Investigations of Grid-Connected Wind Power System – Low Voltage Ride Through and Power Quality Issues

Zhang Shao

School of Electrical & Electronic Engineering

A thesis submitted to the Nanyang Technological University
in partial fulfillment of the requirement for the degree of
Doctor of Philosophy

2011

Acknowledgements

First of all, I would like to express my sincere appreciation to my dedicated supervisor, Dr. K.J. Tseng, for the consistent guidance and encouragement he has provided throughout my research in Nanyang Technological University. His patience and kindness are greatly appreciated. His constructive insights and profound knowledge have helped to shape my research skills. His pleasant personality and understanding have inspired me through difficult times. I have learnt from him a lot not only about the scientific research, but also the professional ethics.

I am also deeply thankful to Prof. Choi San Shing, Dr. Don Mahinda Vilathgamuwa, Dr. Luo Fang Lin, Dr. Loh Poh Chiang, Dr. Ali Iftekhar Maswood, and Dr. HAQUE Mohammed Hamidul for their knowledge, guidance, fruitful discussions throughout my study and research in Nanyang Technological University. I am greatly indebted to their broad interests, high enthusiasms for research and exemplary academic standards.

I would like to thank all the technical staff in the Power Electronics Research Laboratory: Mr. Chua Tiam Lee, Ms. Lee-Loh Chin Khim, Ms. Tan-Goh Jie Jiuan, and Mr. Teo Tiong Seng; in the Laboratory for Clean Energy Research: Mr Thomas Foo, Ms Nge Tak Heng, for their technical support in the equipment usage and the software installation. I would like to extend my appreciation to Ms. Koh Lee Min and Ms. Chew Sim Annie for their continuous consideration.

I also wish to express my thanks to my laboratory fellows and friends, especially to Dr. Wang Xiaoyu, Dr. Zhang Chi, Mr. Nguyen Trong Duy, Mr. Wang Mingqiang, Ms. Yao Dailin for their friendly assistance in my research and everyday life. The financial assistance offered by Nanyang Technological University is gratefully acknowledged.

Special thanks are dedicated to my wife Huang Lei for her consistent encouragement. I offer my deepest gratitude to my family and particularly to my parents in law and parents for their love, understanding and support.

Summary

This thesis presents an investigation on system architecture, control and analysis of wind turbine generators to improve grid integration performance. First of all, the main grid connection requirements have been reviewed in terms of safety operation of transmission systems as well as the wind turbine configurations. Due to these requirements, there have been conscious efforts made by wind turbine manufacturers to design grid compatible wind turbines, which are able to improve turbine operating performance and eliminate negative impacts on the utility, with features such as strong fault ride-through capability, flexible voltage regulation and good power quality performance. All these expectations provided the motivation to carry out the research described in this thesis.

Doubly-fed induction generator (DFIG) wind turbine technology has been extensively applied by many turbine manufacturers due to the low cost of its partial-scale power electronics converter. However, enhancing ride-through capability under grid fault events has been worldwide recognized as a challenging problem of the DFIG-based wind generation systems. The operating principle and numerical simulation of DFIG-based wind turbine are thus reviewed, which give the fundamentals to analyze the essential behaviors during grid faults. Consequently, a ride-through enhancing solution is proposed based on series compensation principle. The compensator is in series with the stator windings of the DFIG in order to eliminate the impacts caused by grid voltage faults. Furthermore, an advanced ride-through control scheme based on ramp-function injection voltage is developed to significantly reduce the energy capacity requirement of the series compensator, which in turn reduces the capital cost. The performance of the developed architecture has been verified in simulation.

Compared to DFIG, full scale power electronics converter based wind generators such as those using permanent magnet synchronous generators (PMSG), exhibit superior ride-through and grid support performances. The PMSG will likely be the mainstream turbine generator in most new installations in the next decade. In the PMSG configuration, the power electronics play the crucial function of power interface and buffer to bridge the PMSG and the utility. This project proposes an integration of a three-switch buck-type rectifier and a grid-side Z-source inverter for the application of PMSG wind turbine,

which aims to produce a robust design of wind power generation system. The modulation technique, analysis and demonstration of this topology have been studied in details in this project. Subsequently, the design methodology, the simulation studies, and the experimental verification of a PMSG wind turbine based on this new power converter are presented. The proposed generator-side control strategy is optimized from the fundamentals of the $I_d=0$ control and the unity power factor control. In addition, voltage-oriented control is used for the grid-side inverter to decouple active and reactive power control while extracting the maximum wind power by adjusting the shoot-through duration of the Z-source network. The numerical simulation and experimental results have verified the proposed control schemes.

Regardless of DFIG or PMSG, wind power capacity will have a significant percentage of the worldwide electricity demand in the next decade, especially in western European countries. Consequently, grid connected wind power will be significant enough to affect the operation of utility in terms of voltage regulation and frequency control. Thus there is a need to devise reliable methods to accurately quantify the impacts so as to obtain the most appropriate and economical solution to mitigate the negative impacts. Hence, another original contribution of this thesis is a statistics-based analysis method for the purpose of assessing the impact on voltage quality caused by large wind power generation. Herein, voltage deviation has been calculated using the probabilistic models of wind power production and grid Thevenin impedance. An index called the significance level of the voltage deviation α has been developed to provide a probabilistic measure of the voltage quality performance. By considering the contributing factor from each of the grid states that constitute α, possible solution methods to improve voltage quality can be obtained. A case study has been included to illustrate the effectiveness of the proposed method.

Table of Contents

Acknowledgements ..... **i**

Summary ..... **ii**

Table of Contents ..... **iv**

List of Figures ..... **viii**

List of Tables ..... **xii**

List of Abbreviations ..... **xiii**

List of Principal Symbols ..... **xv**

CHAPTER 1 INTRODUCTION **1**

1.1 Motivation 1

1.2 Objectives 4

1.3 Major contributions of the thesis 5

1.4 Organization of the thesis 7

CHAPTER 2 LITERATURE REVIEW **9**

2.1 Introduction 9

2.2 Wind market development 9

2.3 The advances in wind turbine technology 12

2.3.1 Fixed rotor speed wind turbine 13

2.3.2 Partial variable speed wind turbine 15

2.3.3 Variable speed wind turbine 16

2.4 Review on types of generator machines 16

2.4.1 Doubly fed induction generator type 16

2.4.2 Permanent magnet synchronous generator type 18

2.4.3 Synchronous generator type 19

2.4.4 Squirrel cage induction generator type 20

2.4.5 Switched reluctance generator type 22

2.4.6 Summary of the wind power configurations 22

2.5 Grid regulation for wind turbines/plants 24

2.5.1 Ride-through ability of wind turbine 25

2.5.2 Control of voltage and reactive power 27

2.5.3 Active power and frequency regulation 30

2.5.4 Power quality issues 31
2.6 The potential challenges for grid-connected wind turbines 33
2.6.1 Fault ride-through enhancement for DFIG wind turbine 33
2.6.2 Power architecture improvement for PMSG wind turbine 36
2.6.3 Potential methods to quantify wind power impacts 38
2.7 Conclusion 40

CHAPTER 3 RIDE-THROUGH ENHANCEMENT OF DFIG WIND TURBINES BASED ON SERIES VOLTAGE COMPENSATION 42

3.1 Introduction 42
3.2 Fundamentals of DFIG wind turbine 43
3.2.1 Mathematical model of DFIG 43
3.2.2 Field oriented control of DFIG 45
3.3 A series compensator based ride-through enhancement for DFIG 53
3.4 Essential behavior of DFIG during grid fault 55
3.4.1 Phasor diagram during normal operation 55
3.4.2 Phasor diagram during grid fault condition 57
3.4.3 Key factors on the DFIG fault operation 60
3.4.4 Advantages and disadvantages of DFIG 61
3.5 General control principle of the series compensator 62
3.5.1 Voltage sag detection 62
3.5.2 Reference voltage generation for series compensator 67
3.5.3 Advantages and Disadvantages of DFIG-Series compensator 68
3.6 Improved ride-through control of DFIG-Series compensator 69
3.7 Simulation results for DFIG 72
3.7.1 Simulation results for DFIG during normal operation 73
3.7.2 Simulation results for DFIG during faults 76
3.7.3 Performance of DFIG 78
3.8 Simulation results for series compensated DFIG 79
3.8.1 Simulation results for series compensated DFIG during normal operation 79
3.8.2 Simulation results for series compensated DFIG during faults 79
3.8.3 Performance of series compensated DFIG 83
3.9 Conclusion 84

CHAPTER 4 MODULATION AND ANALYSIS OF THREE-SWITCH BUCK-TYPE RECTIFIER BASED Z-SOURCE INVERTER 85

4.1 Introduction 85
4.2 Derivation of the proposed topology for PMSG turbine 85
4.2.1 Principle of Z-Source inverter 85
4.2.2 Principle of indirect matrix converter 86
4.2.3 Derivation of the three-switch buck-type rectifier based Z-Source inverter 87
4.3 Operation and Modulation of three-switch rectifier based Z-Source inverter 90
4.3.1 Space vector modulation 90
4.3.2 Control of indirect matrix converter 92
4.3.3 Modulation of the developed converter 93
4.4 Circuit analysis of the developed Z-Source inverter 94
4.4.1 Equivalent circuit analysis 95
4.4.2 Obtainable voltage transfer ratio 98
4.5 Simulation and experimental verification 99
4.5.1 Simulation results 99
4.5.2 Experimental results 102
4.6 Comparison of simulation and experimental results 105
4.7 Conclusions 106

CHAPTER 5 DESIGN OF A ROBUST PMSG TURBINE SYSTEM BASED ON THE DEVELOPED TOPOLOGY 107

5.1 Introduction 107
5.2 Generator-side (PMSG) control principle 108
5.2.1 Unity power factor control of PMSG 109
5.2.2 Id=0 control of PMSG 109
5.2.3 Optimized control strategy of PMSG 110
5.3 System control scheme considering turbine characteristics 112
5.3.1 Maximum power point tracking 112
5.3.2 Control of power delivered into grid 114
5.4 Design consideration of the passive components 115
5.4.1 Parameters design of the Z-Source network 115
5.4.2 Parameters design of the generator-side filter 116
5.5 Simulation and experimental verification 117
5.5.1 Simulation results 117
5.5.2 Experimental results 124
5.5.3 Comparison of simulation and experimental results 128

5.5.4 Comparison with other topology 129
5.6 Conclusion 130

CHAPTER 6 STATISTICAL VOLTAGE QUALITY ASSESSMENT METHOD FOR GRIDS WITH WIND POWER GENERATION 131
6.1 Introduction 131
6.2 Preliminary considerations 131
6.2.1 Network description 131
6.2.2 Impact on the PCC voltage 133
6.3 Probabilistic analysis of PCC voltage deviation 134
6.3.1 Probabilistic model of wind power generation 135
6.3.2 Grid Thevenin equivalent impedance probabilistic model 138
6.3.3 Probabilistic voltage deviation 139
6.4 Significant level of voltage deviation 140
6.5 Case study 142
6.5.1 Wind power distribution 143
6.5.2 Grid Thevenin impedance 144
6.5.3 Voltage deviations probability 145
6.5.4 Screening network states 149
6.5.5 Additional comparison with other Methods 150
6.6 Conclusion 152

CHAPTER 7 CONCLUSIONS AND RECOMMENDATIONS 153
7.1 Conclusions 153
7.2 Recommendations 155

AUTHOR'S PUBLICATIONS 157

BIBLIOGRAPHY 159

APPENDICES 169
Appendix A: Laplace transform 169
Appendix B: Wind power probability calculation 171

List of Figures

Fig.2.1 World total installed wind power capacity 10
Fig.2.2 Country share of total capacity in 2009 10
Fig.2.3 Projected total installed wind capacity 1997-2020 11
Fig.2.4 A fundamental wind turbine configuration 12
Fig.2.5 Fixed speed wind turbine with squirrel cage induction generator 13
Fig.2.6 Fixed speed turbine configuration with permanent magnet synchronous generator 14
Fig.2.7 Wind turbine configuration with variable rotor resistances 15
Fig.2.8 Wind turbine configuration based on DFIG 16
Fig.2.9 PMSG wind turbine with DC chopper 18
Fig.2.10 PMSG wind turbine with back-to-back converter 19
Fig.2.11 Wind turbine configuration with synchronous generator 19
Fig.2.12 Variable speed turbine with squirrel cage induction generator 21
Fig.2.13 Squirrel cage induction generator based turbine with simple power converter 21
Fig.2.14 Wind turbine configuration with switched reluctance generator 22
Fig.2.15 Typical fault ride-through requirement of wind farm 26
Fig.2.16 More stringent fault ride-through requirements of wind farm 26
Fig.2.17 Single line diagram of a grid connected wind generation system 27
Fig.2.18 Power factor requirement for wind farm integrated to grid 29
Fig.2.19 DFIG ride-through enhancement with crowbar circuit 34
Fig.3.1 A wind generation system based on doubly fed induction generator 42
Fig.3.2 Vector diagram of the DFIG 43
Fig.3.3 Equivalent circuit of a DFIG in the reference frame rotating at ω 44
Fig.3.4 Vector control scheme for the rotor-side converter 48
Fig.3.5 Grid voltage vector orientation for the grid-side inverter 49
Fig.3.6 Grid-side converter arrangement 49
Fig.3.7 Vector control scheme for the grid-side converter 51
Fig.3.8 Power transfer coefficient C_p versus Tip-speed ratio λ 52
Fig.3.9 System control diagram of the DFIG based wind turbine 53
Fig.3.10 Single-line diagram of the DFIG based wind turbine connected to grid. 53
Fig.3.11 Γ-form equivalent circuit of the DFIG in the static frame 55
Fig.3.12 Phase diagram of DFIG during normal operation 57

Fig.3.13 Phase diagram of DFIG during grid fault 58

Figure 3.14 Simplified phase diagram of DFIG during a full voltage dip and a partial voltage dip with the phase shift φ 59

Fig.3.15 The magnitude and angle-jump of stator voltage impact on the rotor current ... 60

Fig.3.16 Determination of the maximum allowed voltage drop on the PCC under the maximum rotor current $I_{r,max}$ 65

Fig.3.17 The maximum allowed PCC voltage drop boundaries along with different pre-fault rotor current angle θ_0 66

Fig.3.18 Phase diagram of series voltage compensation under grid faults 67

Fig.3.19 The series voltage V_{sc} related to fault PCC voltages V_{pcc} under different rotor current limitation 67

Fig.3.20 Wind turbine power characteristics used in the simulation 73

Fig.3.21 DFIG operating performance under different wind speeds 74

Fig.3.22 The steady-state stator and rotor voltage/current waveforms 75

Fig.3.23 Stator/rotor voltages and currents in the conventional DFIG system 76

Fig.3.24 Feasible ride-through region of the conventional DFIG system under three-phase balanced fault 77

Fig.3.25 Fault voltage phase shift impacts on the ride-through performance in the original DFIG system 78

Fig.3.26 Ride-through performance of the DFIG system with the series compensation method 82

Fig.3.27 Zoom-in of the voltage compensation during transient fault 82

Fig.3.28 The relationship of the rotor peak current/ DC link capacitance of the series compensator versus the compensation time ΔT 83

Fig.3.29 The control of the reactive current of the grid-side converter during the fault period 83

Fig.4.1 DC Z-Source network diagram 86

Fig.4.2 Topology of a three-phase indirect matrix converter 86

Fig.4.3 Integration of IMC and Z-Source network 87

Fig.4.4 Simplification of one-leg in the front-end converter 88

Fig.4.5 Two derivatives of the proposed IMC based Z-Source inverter 89

Fig.4.6 Input current space vector modulation of the front-end rectifier 90

Fig.4.7 Space vector representation of the back-end inverter 91

Fig.4.8 Switching modes synthesis of the IMC 92

Fig.4.9 Switching sequence for the developed Z-Source topology 94

Fig.4.10 Reduced circuit of the developed Z-Source inverter 94

Fig.4.11 Equivalent circuit modes of the developed Z-Source inverter 95

Fig.4.12 Operating waveforms of the Z-Source inverters 98

Fig.4.13 Simulation results of output voltage and current with shoot-through 100

Fig.4.14 Simulation results of DC-link voltage and current waveforms with shoot-through 101

Fig.4.15 Simulation results of input voltage and current waveforms with shoot-through 101

Fig.4.16 Photograph of the prototype of three-switch buck-type Z-Source inverter 102

Fig.4.17 Experimental results of DC-link voltage and current waveforms without shoot-through 103

Fig.4.18 Experimental results of output voltage and current waveforms without shoot-through 103

Fig.4.19 Experimental results of DC-link voltage and current waveforms with shoot-through 104

Fig.4.20 Experimental results of output voltage and current waveforms with shoot-through 104

Fig.4.21 Experimental results of input voltage and current waveforms with shoot-through 105

Fig.5.1 Proposed PMSG based wind generation system 107

Fig.5.2 Three-switch buck-type rectifier based Z-Source inverter for PMSG 108

Fig.5.3 Equivalent circuit and phasor diagram of the PMSG 108

Fig.5.4 The turbine power output versus the generator speed under different wind speeds 112

Fig.5.5 System control diagram of the developed PMSG wind generation system 113

Fig.5.6 Simulation results of the PMSG-side operating profiles 118

Fig.5.7 Simulation results of the grid-side operating profiles 120

Fig.5.8 Comparison of efficiency of PMSG under different control principles 121

Fig.5.9 Comparison of the converter power ratings under different control principles . 121

Fig.5.10 Simulation results of PMSG voltage and current waveforms in the proposed system 123

Fig.5.11 Simulation results of PMSG voltage and current waveforms in the conventional diode-fronted system 123

Fig.5.12 Simulation results of PMSG voltage and current waveforms in the back-to-back converter system 124

Fig.5.13 Experimental setup of the proposed system 124

Fig.5.14 Experimental results of generator reference and actual speeds, the shoot-through duty-cycle D and active power output 125

Fig.5.15 Steady-state experimental waveforms of voltage and current of PMSG with unity power factor method 126

Fig.5.16 Steady-state experimental waveforms of voltage and current of PMSG with the Id=0 control 127

Fig.5.17 Experimental waveforms of voltage and current in the conventional diode front-end system. 127

Fig.5.18 Experimental results of reliable operation of the proposed system. 128

Fig.6.1 Diagram of wind generation system 132

Fig.6.2 A typical discrete probability distribution of wind speed 136

Fig.6.3 Probabilistic derivation 137

Fig.6.4 Network elements in grid 138

Fig.6.5 The base-case network model used in the study 142

Fig.6.6 Wind speed probability distribution 143

Fig.6.7 Discrete probability distribution of wind power: rated power 300MW 144

Fig.6.8 Probabilistic distribution of ΔV 146

Fig.6.9 Significant level α vs P: with and without accelerated G3 repair 149

Fig.6.10 Comparison between the probability density distribution of wind speed obtained from MCS and proposed method 151

Fig.6.11 Comparison between the probability density distribution of wind power obtained from MCS and proposed method 151

List of Tables

Table 2.1 Characteristics summary of wind turbine configurations 23

Table 3.1 DFIG parameters 72

Table 4.1 Parameters of the three-switch buck-type rectifier based Z-Source inverter ... 99

Table 5.1 System Parameters of the Proposed Systems 117

Table 5.2 Comparison between the back-to-back converter and the developed converter 130

Table 6.1 Component Reliability Data 144

Table 6.2 Thevenin Impedance of Grid at Various States and the Associated Probability (Base MVA = 1000) 145

Table 6.3 Grid States and Probability when $|\Delta V| > 0.1$ 147

Table 6.4 Comparison of voltage deviation ΔV obtained from the conventional load flow study and from the proposed probabilistic method 148

Table 6.5 Computational Time Comparison 150

List of Abbreviations

AC	Alternative current
AVR	Automatic voltage regulator
D	Duty-cycle
DC	Direct current
DFIG	Doubly-fed induction generator
EMF	Electromotive force
ESS	Energy storage system
FACT	Flexible AC transmission systems
FFT	Fast Fourier transform
GSC	Grid side converter
GSI	Grid side inverter
HVDC	High voltage direct current
IEC	International electrotechnical committee
IMC	Indirect matrix converter
KCL	Kirchhoff's current law
m	Modulation index
MCS	Monte Carlo simulation
MPPT	Maximum power point tracking
PCC	Point of common coupling
pdf	Probability density function
PF	Power factor
PLF	Probabilistic load flow
PLL	Phase-locked loop

PMSG	Permanent magnet synchronous generators
PWM	Pulse width modulation
rms	Root mean square
RSC	Rotor side converter
SCIG	Squirrel cage induction generator
SCR	Silicon controlled rectifier
SDP	Switching device power
SPWM	Sinusoidal pulse width modulation
SRG	Switched reluctance generator
SVM	Space vector modulation
THD	Total harmonic distortion
TSO	Transmission system operators
TSR	Tip-speed ratio
VSI	Voltage source inverter
WECC	Western Electricity Coordinating Council
WRIG	Wound rotor induction generator
WTG	Wind turbine generator
WWEA	World Wind Energy Association

List of Principal Symbols

C_{in}	Capacitance of the input LC filter
C_p	Power coefficient of wind turbine
E	The equivalent Thevenin voltage
$f(v)$	The Probability density function of wind speed
Fv	The probability distribution of wind speed
I_r	Rotor current
i_{rd}	Rotor current component in d_s-axis
i_{rq}	Rotor current component in q_s-axis
I_S	Stator current
i_{sd}	Stator current component in d_s-axis
i_{sq}	Stator current component in q_s-axis
L_{in}	Inductance of the input LC filter
L_m	Mutual inductance
L_r	Rotor total magnetic inductance
L_{rl}	Leakage inductance of the rotor windings
L_S	Stator total magnetic inductance
L_{sl}	Leakage inductance of the stator windings
p	Machine pole pairs
P	Active power
Q	Reactive power
R	Resistance
v	Wind speed
v_{in}	Cut-in wind speed

v_{out}	The cut-out wind speed
v_r	The rated wind speed
V_{pn}	The voltage on the fictitious DC-link
V_r	Rotor voltage
V_{rd}	Rotor voltage component on d_s-axis
V_{rq}	Rotor voltage component on q_s-axis
V_S	Stator voltage
V_{sd}	Stator voltage component on d_s-axis
V_{sq}	Stator voltage component on q_s-axis
$V_{Threshold}$	The maximum voltage error allowed on the PCC
ΔV	Voltage deviation
X	Impendence
Z	The equivalent Thevenin impedance
α	Significance level of voltage deviation
γ	R/X ratio
δ	The torque angle
λ	Tip-speed-ratio
λ_{pm}	The permanent magnetic flux
ρ	Air density (kg/m3)
Ψ	Magnetic flux
ω_e	Synchronous angular speed
ω_r	Rotor speed of wind turbine

CHAPTER 1

INTRODUCTION

1.1 Motivation

The twin problems of global warming and exhaustion of fossil fuels have seen an increase in the usage of renewable energy, such as wind energy, solar energy and biofuel in recent years. Especially, wind power generation has experienced a very fast development in the last decade [1]. By the end of 2009, the worldwide capacity of wind power generators has been as large as 159.2 gigawatts [2]. Obviously, the installing capacity of wind power generators will continue to increase in the countries with abundant wind potential. Consequently, it can be expected that capacity of wind power production will be a significant amount of energy produced by large conventional power plants. Actually, several countries and regions have presented this situation. For instance, in Western Denmark, Schlesswig-Holstein in Germany, and Navarra in Spain, the wind power capacity has reached the limit which can have a significant impact on the operation of the connected transmission system [3]. Hence, the influence of wind turbines on the power quality of grid network is becoming an important issue due to the rapid increase of wind power penetration.

Among all the influences caused by grid-connected wind turbine, the main impacts are focused on voltage profiles, energy loss, frequency control, power quality improvement and system restoration practices in case of faults [4]. For instance, the increased use of wind turbines for generating electricity makes frequency control more challenging, due to the intermittent nature of wind conditions. In addition, the problem of harmonized integration becomes even challenging as the level of wind power penetration increases. Not only are the voltages at various locations affected, but also the power flow, power system dynamics, transient stability, and reliability [5]. Denmark has been a pioneer in the large-scale connection of wind farms to the grid. Due to these impacts, they have to temporarily shut down some wind turbines especially under conditions of strong wind and low load demand. The purpose is to reduce the negative impacts caused by high wind

power penetration. However, this is not an optimal solution to deal with the increasing wind power production from all over the world.

In addition, more and more stringent rules for grid connected wind turbines have been released by transmission system operators (TSO) in order to ensure the grid remains stable and reliable. According to the codes released by Energinet, E.ON, and WECC [6], the technical requirements have been defined with respect to frequency control, voltage regulation, fault ride-through ability and power quality improvements. For instance, in the past, wind turbines are allowed to disconnect from the connected grid system under conditions of system faults. However, the situation has to be changed in view of large wind power penetration into the transmission systems. Hence under new grid codes, wind turbines are required to maintain connection during grid faults in terms of system stability operation [7]. Moreover, wind turbines are now required to provide reactive power to restore grid voltage during fault conditions according to the latest grid codes in western European countries. Therefore, wind turbines are now generally demanded to serve as generation plants with high reliability and strong grid support, not unlike the conventional coal, oil and gas fired power plants.

Wind generation system is basically equivalent to variable speed pump/fan drive system operation in regenerative mode. Hence, there would be a large amount of wind generation systems, which can be transferred from various drive systems. But different types of wind turbines would have different grid integration performances. Better integration performance is expected from modern turbines since power electronics are widely used [8]. The power electronics are able to produce better dynamic response, faster fault monitoring, and quicker reaction operation. Power electronics were minimally used in the Danish concept of wind turbine two decades ago [9]. It does not actively regulate the terminal voltage because of the absence of reactive power production. Thus it inherently exhibits poor grid support characteristics. So it is required to install additional reactive power equipment to meet the power grid specifications. However, there are always costs associated with the installation and operation of supplementary devices, which makes this option less attractive [10].

Consequently, partial-scale power electronics converter was utilized in the doubly-fed induction generator (DFIG) based wind turbine. More than 50% of the installed turbines

in the last decade are of this configuration. By appropriately controlling the converters in this concept, it becomes possible to locally maintain the power factor or the voltage on the point of common coupling (PCC). However, the DFIG is very sensitive to network disturbances and is inadequate to satisfy with the latest ride-through requirements imposed by grid operators, especially during severe grid fault events [11] occurring near the turbines. In order to meet fault ride-through requirements, it is needed to explore feasible and efficient solutions to enhance the ride-through ability of this kind of turbine, and to keep these turbines connected to the grid utilities.

Compared to DFIG, full scale power electronics converter based wind generators such as those using permanent magnet synchronous generators (PMSG), exhibit superior ride-through and grid support performances. According to predictions by the Danish wind consultation company MAKE, the PMSG will be the mainstream turbine generator in most new installations in the next decade (barring any unexpected upsurge in the price of permanent magnetic materials). In the PMSG configuration, the power electronics play the crucial function of power interface and buffer to bridge the PMSG and the utility. Hence, to seek more efficient and robust power electronics converters would be one of the potential research topics for the development of the modern grid compatible wind turbines.

Regardless of DFIG or PMSG, wind power capacity will have a significant percentage of the worldwide electricity demand in the next decade, especially in western European countries [12]. Consequently, wind power will affect on the operation of utility in terms of voltage regulation, frequency control and so on. Hence, there is a need to devise reliable method(s) to accurately quantify the impacts so that the most appropriate and economical solution to mitigate the impacts can be obtained.

Bearing all these in mind, wind turbine will be required to have capabilities of maintaining good voltage control, frequency regulation, reactive power support, and fault ride-through ability. So it would be timely to develop a reliable wind generation system with improved grid connection characteristics and integration performances. It should also efficiently reduce ancillary impacts of large wind power penetration in order to enhance operation reliability of wind energy connected grid utilities. This research is motivated by the quest for enhancing grid integration of the existed turbine configurations

especially in their ride-through capability, investigating efficient and reliable modern wind turbine architecture, modeling challenges of grid impacts caused by increasing wind power penetration, and thereby analyzing feasible operation and improvement for wind turbines to confront the aforementioned negative impacts.

1.2 Objectives

The objectives of this research project are listed below:

Objective 1: Fault ride-through enhancement of the DFIG based wind turbine

It is well-known that the DFIG is sensitive to network disturbances, especially severe grid faults. The crowbar technology is usually utilized to help ride through grid faults in the conventional DFIG turbine. The new more stringent grid codes not only require the generators to ride through faults, but also demand the generators to provide reactive current during faults. However, if the crowbar is activated, the generator is out of control, which in turn, is impossible to control the reactive current. Hence, the conventional crowbar solution will not be able to satisfy the latest grid requirements. To develop advanced ride-through technology is one of the potential research topics to improve grid integration performance of DFIG.

The main objective of this research is to enhance the ride-through ability of DFIG based wind turbines since a large number of this kind of turbine has been installed in the past.

Objective 2: Design of a robust power architecture for PMSG based wind turbine

Compared to DFIG, the PMSG based wind turbine has better grid integration performance since full-scale power electronics converter is utilized. An AC-DC-AC converter, named as back-to-back converter is usually used to bridge the AC generator and the AC network. However, the disadvantage of this converter is the high risk of bridge shoot-through besides a high number of switching devices. Moreover, the risk of shoot-through phenomenon may be increasing rapidly along with the increase of power ratings. Hence, it is necessary to develop a power electronics architecture which can serve as a reliable power interface between PMSG and grid utility. The control scheme for the

developed topology will also need to be developed with the concern of wind power characteristic to obtain maximum power point tracking (MPPT). The dynamic control behavior should be studied in order to verify the feasibility of this architecture for PMSG.

The main objective of this research is to develop a reliable power architecture and thereby develop the generator control and grid integration scheme for the PMSG turbine.

Objective 3: Development of voltage quality assessment method for grids with wind power penetration

Regardless of DFIG or PMSG, wind power generation will meet a significant percentage of the worldwide electricity demand in the next decade. Large wind power injection is able to affect the connected power transmission system. The main impacts are voltage profile, frequency regulation and system stability. It is necessary to analyze the essential causes of these issues. Modeling and analysis of these impacts can help to propose potential methods for alleviating/mitigating the corresponding impacts.

Hence, the main objective of this research is to devise reliable methods, which can quantify accurately the impacts of the characteristics of wind farm, transmission network and grid topology. From the analysis of the derived methods, they can be helpful to guide design and planning of modern wind farms and thereby make wind turbines satisfy with stringent grid regulations.

1.3 Major contributions of the thesis

The major contributions documented in this thesis are given below.

1. A feasible ride-through enhancement of DFIG based wind turbine

The proposed ride-through solution is inspired by power quality improvement devices, i.e., series compensator. The compensator is in series with the stator windings of DFIG in order to reinforce the fault ride-through capability. Firstly the control fundamentals of the conventional DFIG have been reviewed and thereby the essential behavior of DFIG under grid faults has been analyzed in detail via system phasor diagram. Then the general control scheme for the series compensator is provided. Furthermore, an improved control

scheme based on ramp-function injection voltage has been developed to significantly reduce the energy capacity of series compensator, which in turn reduce the capital cost. The performance of the designed architecture has been verified in simulation.

2. Modulation, analysis and verification of three-switch rectifier based Z-Source inverter for full power converter in WTG applications

The operating principle of an integration of a three-switch buck-type rectifier and a Z-Source inverter has been investigated and the related modulation strategy has been given. The equivalent circuit analysis of the proposed converter is given for an in-depth understanding of its essential behavior. The simulation studies and experimental results have verified the buck-boost characteristic of the developed converter. All these studies are desired to integrate the developed converter for full power converter based wind turbine application, such as those based on PMSG.

3. Design of a robust PMSG wind turbine based on three-switch rectifier based Z-Source inverter topology

The design methodology, the simulation studies, and the experimental verification of the integrated generator-side buck-type rectifier and grid-side Z-Source inverter based PMSG wind generation system have been presented. Based on the developed modulation scheme of the integrated topology, the generator-side control strategy has been proposed, which is optimized from the fundamentals of the $I_d=0$ control and unity power factor method. The voltage-oriented control has been adapted for the Z-Source inverter to decouple active and reactive power control while extracting the maximum wind power by adjusting the shoot-through duration of the Z-Source network.

4. A voltage quality assessment method for grids with wind power penetration has been proposed in this thesis

A statistics-based analysis method has been proposed for the purpose of assessing the impact on voltage quality caused by wind power generation. Voltage deviation has been computed using the probabilistic models of wind power production and grid Thevenin impedance. An index called significance level of the voltage deviation α has been developed to provide a probabilistic measure of the voltage quality performance. By considering the contributing factor from each of the grid states that constitute α, possible

solution methods to improve voltage quality can be obtained. A case study example has been included to illustrate the effectiveness of the proposed method.

1.4 Organization of the thesis

Given below is a brief introduction of what is covered in each chapter:

Chapter 1 presents the objectives and contributions of this research after describing the motivation of our work. The organization of this thesis then follows.

Chapter 2 gives the literature review of worldwide wind power market, wind turbine configurations, corresponding grid connection requirements and potential challenges of wind power technology. The turbine configurations are described in terms of different generators and the main grid connection demands are then considered in terms of safety operation of transmission systems. The challenges of wind power technology provided a guide to define the research objectives.

Chapter 3 proposes a potential ride-through solution for the DFIG to deal with grid faults. A compensation device is in series with the stator windings of DFIG in order to reinforce the fault ride-through capability. The improved ride-through control scheme for the DFIG and series compensation is developed to reduce the energy capacity of the series compensator. The performance of the designed architecture is verified in simulation.

Chapter 4 describes complete modulation principle of an integration of a three-switch buck-type rectifier and a Z-Source inverter. The equivalent circuit analysis is given as well. The simulation studies and experimental results have verified the modulation of the developed topology. The developed topology is suitable to apply in the full power converter based wind turbines, such as those based on PMSG.

Chapter 5 introduces a robust PMSG wind turbine based on the aforementioned converter topology described in Chapter 4. The proposed generator-side control strategy of the generator-side converter is optimized from the fundamentals of the $I_d=0$ control and unity power factor method. The voltage-oriented control of the grid-side converter is adapted to

decouple active and reactive power control. The simulation and experimental results have verified the proposed wind generation system.

Chapter 6 presents the modeling approach for the voltage impact caused by high wind power penetration. A probabilistic method is used to analyze the voltage issue with the consideration of wind uncertainty and reliability of elements in the transmission system. It provides a way to quantify the severity of voltage impacts caused by wind power injection. A case study has been carried out and described in this chapter.

Chapter 7 provides the concluding remarks of this thesis together with the recommendations for future research.

CHAPTER 2

LITERATURE REVIEW

2.1 Introduction

Nowadays, wind energy is a major renewable energy source to integrate into the grid. The worldwide total installed wind turbine capacity is up to 160 gigawatt at the end of 2009 when the global financial and economical crisis started. However, the crisis seemed to have no negative impact on the general development of the wind sector worldwide. Many governments sent clear signals that they wanted to accelerate wind deployment in their countries and indicated that investment in wind and other renewable technologies is an answer to the financial crisis as well as to the still ongoing energy crisis.

Along with the increasing wind power penetration into grid, the interconnection requirements for grid connected wind farms are generally formulated in order to maintain the operation performance of the connected power utilities. In the past, there is little need to consider impacts caused by wind power penetration due its low percentage of the total network capacity. However, the related impacts will be becoming very serious due to rapid increasing wind power penetration into grid without auxiliary solutions.

In this chapter, wind energy technology will be reviewed in terms of various types of generators and the related power electronics. Then grid regulations for grid-connected turbines are reviewed with the aim to address the potential challenges for exciting wind turbines. Consequently, the potential research directions and contents of the following chapters can be clarified based on the detailed review of the current solutions for these challenges.

2.2 Wind market development

In spite of the global economic crisis, the wind capacity worldwide at the end of 2009 reached 159.2 GW after attaining 120.9 GW in 2008. Figure 2.1 illustrates the worldwide

wind power capacity during the last decade from the World Wind Energy Association (WWEA) [13]. The projected wind capacity at the end of 2010 will be up to 203.5 GW. The strong increase of wind capacity means wind based renewable energy has been paid much attention all over the world. In fact, they have recognized that wind energy is an important alternative to address the environment and climate change issues, which seem to be more and more serious in the recent years.

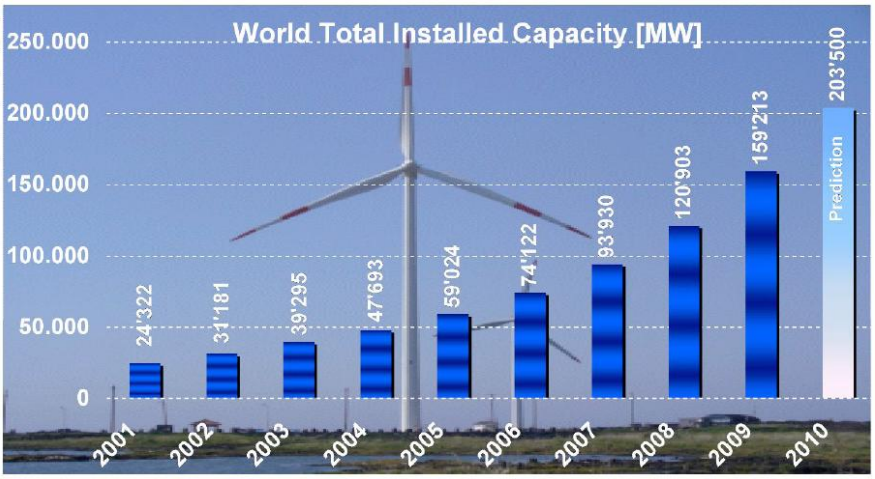

Fig.2.1 World total installed wind power capacity

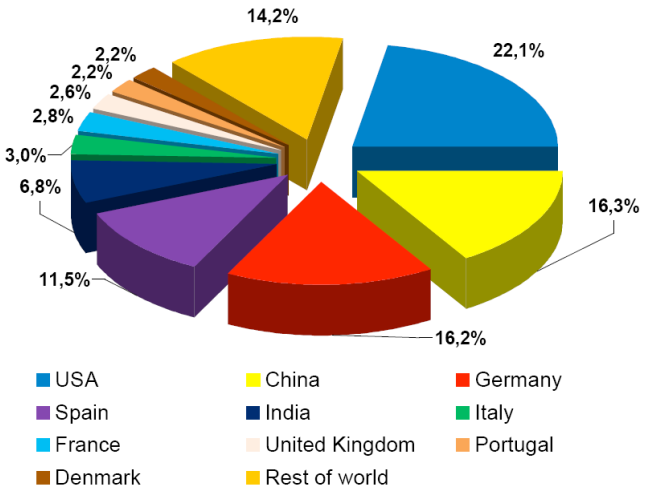

Fig.2.2 Country share of total capacity in 2009

From the WWEA, Figure 2.2 shows the country share of the wind capacity in 2009 [13]. Many western countries, such as United States, Germany and Spain, have major percentage of the worldwide wind capacity. However, in the recent years, especially in 2009, the wind industry has achieved significant development in the Asian countries, such

as China and India. At the end of 2009, China became the second largest country behind the United States to utilize wind energy. The total wind capacity of China and India have attained more than one fourth of the world total capacity. Hence, it can be expected that the wind industry in Asia will continue to grow rapidly in the next decade along with the strong economy of those countries.

Figure 2.3 shows the total installed wind capacity in 1997-2020. As predicted by the WWEA, the total installed wind capacity at the end of the next decade will reach 1,900 GW, which has a significant increase compared to the current capacity. Although wind capacity is only 2% of the worldwide electricity demand in 2010, the percentage will be increased rapidly in the next several years. In some European countries, the wind capacity has already reached more than 10% of the domestic electricity demand at the end of 2010. For instance, the wind capacity in Denmark has reached the point where it can have a significant impact on the operation characteristics of the transmission system. The situation would be much more serious when high wind conditions where 100% of the wind power may be generated under relative low load condition. In addition, similar situation would be met in India because of its relatively weak power grids. The wind power penetration attains levels high enough to affect the power quality and stability of the grids.

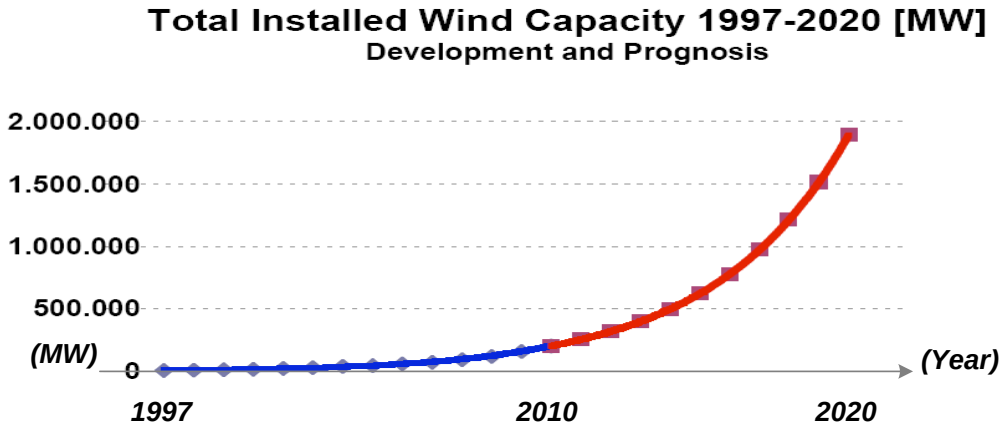

Fig.2.3 Projected total installed wind capacity 1997-2020

Consequently, the countries with the high wind capacity percentage have been much earlier to consider the grid connection issues than other countries. For instance, Denmark, Germany and Spain are three countries that have established their respective grid codes to

regulate the wind power penetration into the transmission network. Hence, the various codes for grid connection of wind turbines should be investigated in order to advance the development of wind conversion system. It is worthy to point out that the operation performances of different configurations of wind turbines directly affect the operation of the connected power transmission system. Hence, it is necessary to review the advances in wind turbine technology, which will be presented in the next section.

2.3 The advances in wind turbine technology

In recent 2 decades, generation capacity of wind turbines has increased from tens' kilowatts to more than 3 MW, while even larger wind turbines are being designed [14]. Furthermore, a number of different generator concepts have been developed and tested. For the electrical system of wind turbines, some manufacturers have started to use asynchronous generator with wound rotor in their wind turbine design, while others have replaced the conventional induction generator by a synchronous generator. This development has introduced the use of power electronics as an interface in their design and led to the variable speed wind turbine. This is designed to pursue maximum aerodynamic efficiency over a wide range of wind speed, to reduce the mechanical stress in the gearbox and to improve the controllability of the active and reactive power which is growing in importance for integrating wind power into grid utility.

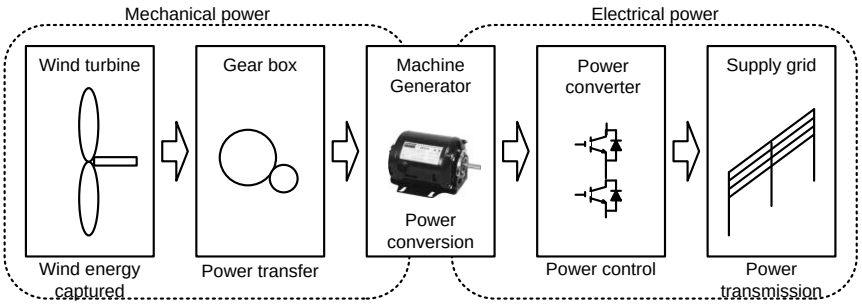

Fig.2.4 A fundamental wind turbine configuration

A fundamental configuration of wind energy conversion system is shown in Fig.2.4. The whole wind system can be divided into mechanical and electrical parts. The mechanical part is used to transform wind energy into the rotating mechanical energy. The mechanical power is converted to electrical energy by generators in the electrical part.

There are many kinds of generators which can be applied in the wind system, such as DC generator, permanent magnet synchronous generator, multi-pole synchronous machine, and induction machine. Reasonably, the variable speed wind turbine has a lot of advantages over the fixed ones in terms of wind power capture efficiency, reducing mechanical stress of gearbox, and so on. So wind turbine can be designed to generate electricity as much as possible based on variable speed conversion concept.

The characteristic of wind turbine can be adapted to estimate power transferred efficiency from wind power into the rotating mechanical power. The most commonly used wind turbine configurations can be categorized into the following concepts: fixed speed wind turbine, partial-variable speed wind turbine, and variable speed wind turbine. The main differences between these designs concern the generating system and wind energy captured efficiency in relation to generator rotor speed. The detail will be discussed in the next sections.

2.3.1 Fixed rotor speed wind turbine

The fixed speed wind turbine has the advantage of being simple, robust and reliable, and easy to maintain. Traditionally, the constant speed wind turbines were coupled to squirrel cage induction generator (SCIG) or wound-field synchronous generator. This configuration also known as the Danish concept that was very popular in 1980's [15]. In the fixed speed wind turbines, the generator is directly connected to the grid. The frequency of the grid determines the rotational speed of the generator rotor. Generally, the generator speed depends on the number of pole pairs and the frequency of the grid. Consequently, the wind turbine is the fixed speed controlled machine with asynchronous cage induction generator directly connected to the grid via a transformer as shown in Fig.2.5.

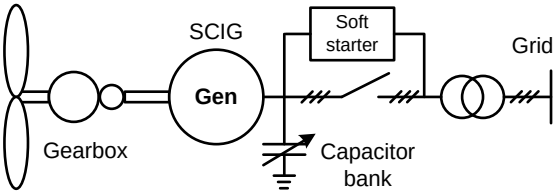

Fig.2.5 Fixed speed wind turbine with squirrel cage induction generator

In this configuration, a reactive power compensator is required to reduce (or even eliminate) the reactive power demand from generator to the grid. Normally it is realized by continuously switching capacitor banks following the production levels (5-25 steps). Additional, a soft starter is incorporated in order to smooth grid connection and reduce inrush current (as high as 5-7 times of rating current). The asynchronous generator 'naturally' limits power production in strong wind or gusts. It restricts the speed of the system to the frequency of the power grid, so that the rotor cannot turn faster when the wind blows stronger.

Recently, another fixed speed concept based on permanent magnet synchronous generator (PMSG) was proposed in [16] as shown in Fig.2.6. This configuration comprises a grid connected permanent magnet synchronous generator and a 20% rated series converter located in its star point. The main function of the series converter is the active damping of the generator. The low cost characteristic is still achieved since the partial rated converter is utilized. However, this configuration is still fixed speed operating turbine, which is impossible to track maximum point of wind power.

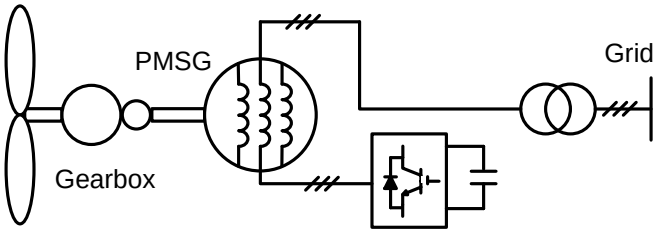

Fig.2.6 Fixed speed turbine configuration with permanent magnet synchronous generator

The available power control for this kind of turbine can be achieved by stall control, active stall control or pitch control. For stall control, the rotor blades are designed to create turbulence when above a certain wind velocity, preventing the lift from accelerating rotation any further even though the blades are themselves not pitched. In the active stall control, the pitch angle of the rotor blades can also be changed to create turbulence. In the concept of the pitch control, electronics and hydraulics are used to continuously adjust the pitch of each blade. This reduces the lift, so that the rotor continues to generate power at nominal capacity even at high wind speeds.

There are some challenges for this kind of wind turbine. First of all, as the wind power fluctuations happen, it is inevitable to affect turbine mechanical torque fluctuations and further into electrical power fluctuations. These can cause voltage fluctuations with the connection of a weak grid. The unbalance between reactive power demand of generator and the reactive power of capacitance banks would result in the corresponding voltage fluctuations. On the other hand, the mechanical torque fluctuations would increase the mechanical stress of mechanical devices. It may require a stronger mechanical construction to absorb high mechanical stress. A mechanical stress calculation method for the fixed speed wind turbine was reported in [17].

2.3.2 Partial variable speed wind turbine

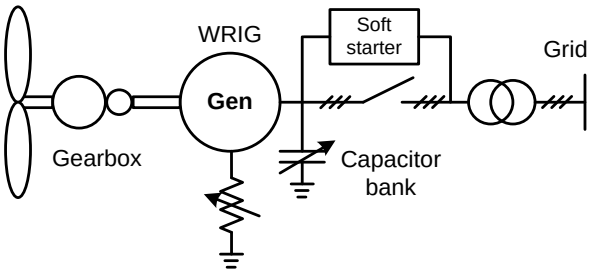

Fig.2.7 Wind turbine configuration with variable rotor resistances

The system diagram of the partial variable speed wind turbine is shown in Fig.2.7. In fact, this configuration is developed based on the fixed speed wind turbine with the purpose of expanding the operation performance. In the partial variable speed wind turbines, the effective rotor resistance of wound rotor induction generator can be varied instantly using fast power electronics. So far, the company Vestas alone has succeeded in commercializing this wind turbine system under the trade mark of Optislip. A number of turbines, ranging from 600 kW to 3 MW, have been developed under this configuration, which allows transient rotor speed increases of up to 10% of the nominal value. In this design, the variable speed technology is realized by dissipating the energy with external rotor side resistors as shown in Fig.2.7. Since the efficiency of the system decreases as the slip increases, the speed control is limited to a relatively narrow margin. The aforementioned stall control, active stall control or pitch control can be adapted in the power control of this kind of wind turbine.

2.3.3 Variable speed wind turbine

In order to overcome the drawbacks of fixed speed wind turbine, variable speed wind turbine based on power electronics can be made to run at desired speed, so that wind turbine can be operated efficiently at a wide range of wind speeds. In variable speed wind turbines, there are several possible combinations of power electronics topologies and machine types for application, such as doubly fed induction machine including wound rotor induction machine with partial-scale power converter, permanent magnet generator with full-scale power converter, synchronous generator with full-scale power converter, cage rotor induction generator with full-scale power converter. In addition, some special machines can be applied in wind generation systems as well [18, 19]. A review of these combinations is given here.

2.4 Review on types of generator machines

2.4.1 Doubly fed induction generator type

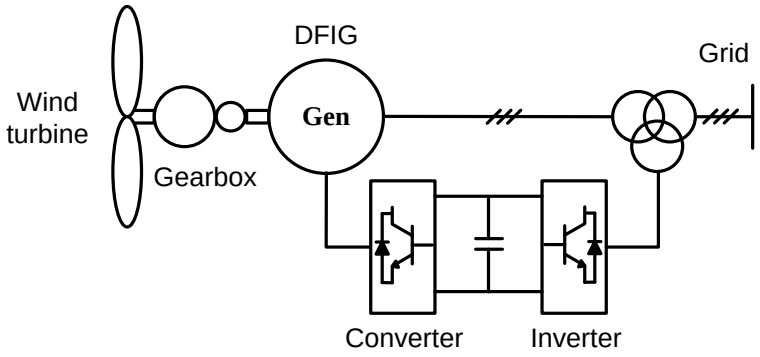

Fig.2.8 Wind turbine configuration based on DFIG

The DFIG based variable speed wind turbine has been investigated by R. Pena [20] in terms of generator-side stator flux orientation, grid-side voltage orientation and maximum power point tracking. Figure 2.8 shows the system diagram of DFIG based variable speed wind turbine. The generator stator is connected directly to the utility grid via an isolated transformer. The generator rotor is connected to a back-to-back converter, where the

rotor-side converter is used to control the rotor current of the generator and the grid-side converter is utilized to control the DC-link voltage and its grid-side power factor. Only slip power is processed by the power electronics converter since the control of the DFIG is tied to the rotor windings, where the purpose of the converter is to synchronize the rotor current with respect to the stator reference of the DFIG. Hence, the smaller the slip speed range the smaller is the power electronics converter, which in turn, to reduce the capital cost of wind turbines. This is one of the significant advantages of the DFIG based wind turbine.

Another advantage using DFIG is the ability to output more than its rated power without becoming overheated. It is able to transfer maximum power over a wind speed range in both sub- and super-synchronous speed. Hence, the DFIG as wind turbine generator is suitable for high power application in the MW level.

Field orientation control can be utilized to control the DFIG. Reference [21] applied a control method using a rotating reference frame fixed on the gap flux of the DFIG and thereby independently control the active and reactive power of DFIG. The estimation method of the gap flux included built-in machine flux sensor and mathematic calculation along with rotor and stator parameters. Consequently, the control performance of this method is very sensitive to the real-time estimation of the gap flux.

To address this problem, a stator-flux vector orientation of the DFIG was introduced in [20]. All the calculation equations would be transferred to the stator side flux. The torque equation would be simple with least coupling variables. The flux expressions would be decided by only one variable in order to simplify the calculation of the corresponding flux. A decoupled control between the electrical torque and the rotor excitation current would be easy to obtain. Furthermore, an indirect stator-flux orientation strategy had been reported in [22]. It was demonstrated that conditions of stator flux field orientation and line voltage orientation are equivalent if the stator side power factor is controlled at unity level. Under such a condition, the stator flux modulus is not a free output variable, but rather it was a function of the produced electromagnetic torque. The torque tracking was then extended to the speed tracking problem in the presence of an unknown constant load torque, using a passivity-based approach.

The operation speed range of the DFIG based turbine is much wider than that of the aforementioned Optislip concept. Most importantly, the efficiency of the DFIG concept is much higher than that of Optislip since the Optislip design needs to burn off some energy in the rotor-side resistors. However, its main disadvantages are the application of slip rings and the protection issues under grid faults, which will be addressed later.

2.4.2 Permanent magnet synchronous generator type

The permanent magnet synchronous generators (PMSG) based variable speed wind turbines were first designed for smaller scale application due to the limited permanent magnet excitation and the cost of power electronics converter [23-25]. The fundamental configuration of variable speed wind turbine with PMSG is shown in Fig. 2.9. This concept has a high power density characteristic. Herein a boost chopper is used to control the PMSG and the grid-side inverter is utilized to service as the grid interface [23-25]. In [23], the duty ratio of chopper converter would affect the modulation ratio of the inverter. The optimal duty ratio was characterized by deriving the equivalent circuit of the whole system.

This system possesses several merits such as simple construction and low cost. However, it lacks control capability over the generator power factor, which reduces generator efficiency. Additionally, high harmonic current distortions in the generator windings further degrade efficiency and produce torque oscillations, which can increase the cost of mechanical components, i.e., gearbox.

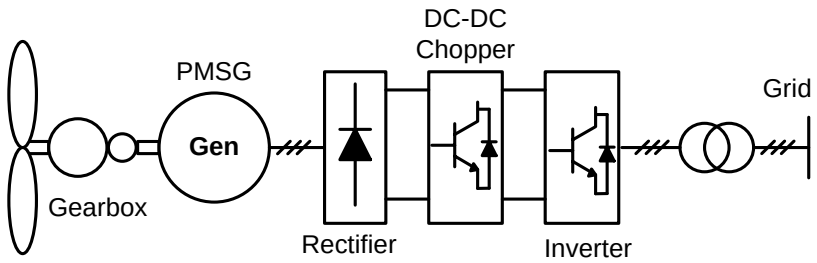

Fig.2.9 PMSG wind turbine with DC chopper

Along with the advance of power electronics, MW-level converter is acceptable for the wind turbine manufacturers. The PMSG was controlled by a fully controllable back-to-

back frequency converter as a configuration of wind generation system [26]. Figure 2.10 shows the system diagram of this PMSG concept. The full scale power converter included a pulse width modulation (PWM) rectifier, an intermediate DC circuit, and a PWM inverter. The generator is controlled to obtain maximum power from the intermittent wind with maximum efficiency via field oriented control of PMSG. At the same time, the voltage oriented control of the grid-side inverter allows power factor regulation of the wind turbine. So far, many wind turbine manufacturers, such as GE Wind and Vestas have announced their commercial PMSG based turbines are available at a power rating up to 3 MW. The significant advantage of the PMSG based turbine is its good performance to deal with grid disturbances compared with the aforementioned DFIG wind turbines.

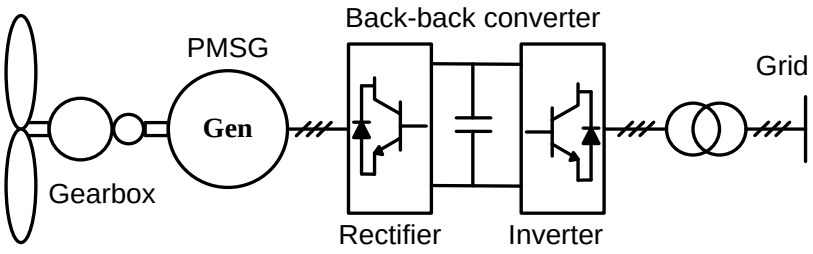

Fig.2.10 PMSG wind turbine with back-to-back converter

2.4.3 Synchronous generator type

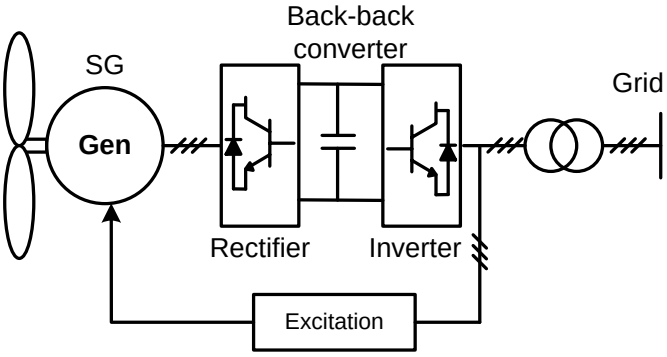

Fig.2.11 Wind turbine configuration with synchronous generator

The commercial wind turbines based on synchronous generator are the products from the Germany wind turbine manufacturer ENERCON. The main configuration with the synchronous generator is illustrated in Fig.2.11. The difference between synchronous

generator and PMSG is the type of excitation. Since there is an independent excited circuit in synchronous generator, the terminal voltage of the generator can be regulated as desired. This generator is suitable to apply in large scale wind turbine.

The control principle of the synchronous generator would be similar to that of the permanent magnet generator except for an extra excitation circuit. The grid-side inverter allowed the control of active power and reactive power respectively. The generator-side rectifier is used for electromagnetic torque regulation [27]. In addition, the full-scale power converter to the grid enables the system to control active power and reactive power very fast, which in turn, to have a good grid connection characteristic. However, it is inevitable to increase the whole cost of wind turbine system according to the full scale power electronics converter, compared to the DFIG wind turbine.

In this concept, the turbine main rotor is coupled to the generator input shaft, eliminating the need for a gearbox, and the reliability can be improved compared with the geared turbines since the mechanical gearbox is the main component reducing the system reliability. In fact, the faults of the mechanical gearbox in the turbines are the most critical from the fault survey in Sweden during 1997~2005 [28], because the downtime per failure of the gearbox is high compared to the other components. Hence, the gearless operation is the significant advantage of this turbine. In addition, the direct-drive generator has reduced the overall size, has lower maintenance cost, has a flexible control method and quick response to wind fluctuations, and load variation [9] as compared to a conventional gearbox-coupled wind turbine generator.

However, the generator has to have many pole pairs in order to generate power at such a low rotation speed, which in turn, increase the size and expense of the generator. So far, this turbine configuration would be most expensive among all the available wind turbine configurations. However, synchronous generator including PMSG is the only type to implement gearless operation among the excited wind turbine generators since it is easy to realize multiple poles design.

2.4.4 Squirrel cage induction generator type

In conventional method, the squirrel cage induction generator has been used in the fixed speed wind turbine which was investigated in Section 2.3.1. Along with the development of power semiconductor and electronics, variable speed wind turbine based on squirrel cage induction generator (SCIG) has been proposed as shown in Fig.2.12. In [29], a complete simulation study of a variable speed wind turbine system based on the SCIG and a double side PWM converter was described. The double side pulse width modulation (PWM) converter directly advance the realization of SCIG based wind turbine in spite of additional cost of power electronic and control.

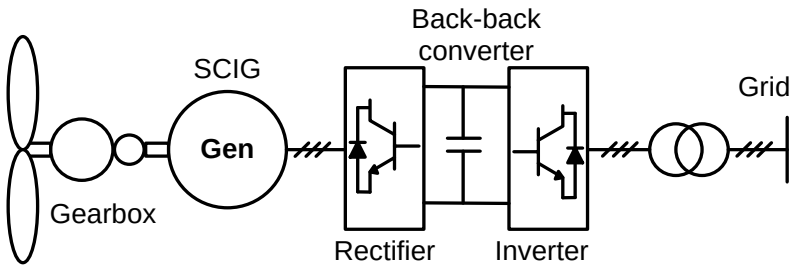

Fig.2.12 Variable speed turbine with squirrel cage induction generator

The full scale converter has to be dimensioned for the maximum power of the turbine. However it is very expensive compared to the aforementioned configuration in Section 2.3.1. Additional, the converter efficiency would affect the entire system performance and has to be very high over the full power range to guarantee a certain performance. This would be another challenge.

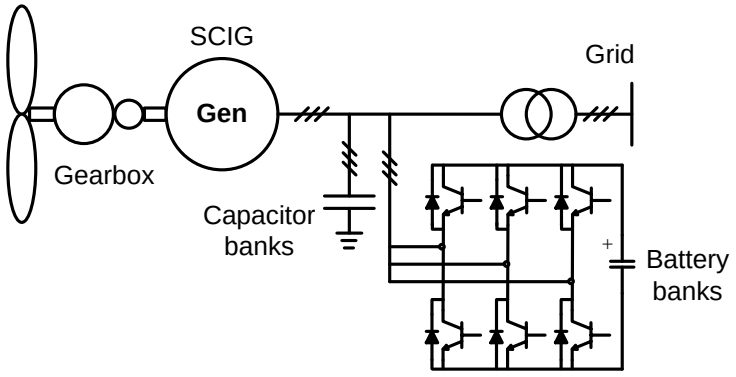

Fig.2.13 Squirrel cage induction generator based turbine with simple power converter

In [30-32], the full scale back-to-back converter was replaced by a number of capacitance banks and relative low rating reactive power compensator. The corresponding scheme of this configuration is depicted in Fig.2.13. An algorithm was used to optimize the demand of capacitance capacity in order to provide enough reactive power for excitation. The interaction control between capacitance banks and reactive power compensator was developed to satisfy variable speed operation characteristics of wind turbine.

2.4.5 Switched reluctance generator type

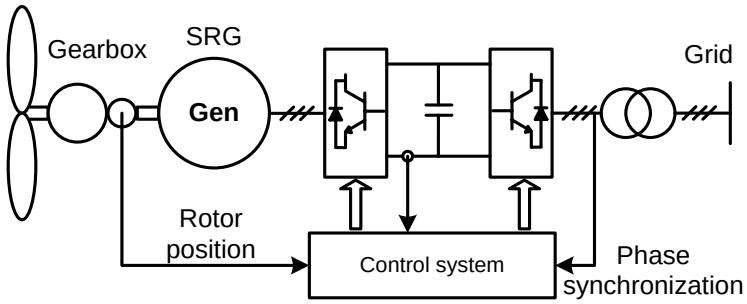

Fig.2.14 Wind turbine configuration with switched reluctance generator

Switched reluctance generator (SRG) has several attributes which make it ideally suited for wind energy schemes [33]. The system diagram is shown in Fig. 2.14. It includes extreme robustness, high efficiency of energy conversion, ability to work over very large speed ranges and control simplicity.

The detailed control strategies of the switched reluctance generator were presented to control the wind power production in [34]. Two converters would be assigned to control generator- and grid-side power factor, respectively. The function of grid-side converter in this scheme would be similar to other types of generators, such as, induction generators, synchronous generator [35]. The maximum power point tracking method was present in [36] by introducing the magnetization curve of the switched reluctance machine.

2.4.6 Summary of the wind power configurations

In the past decades, the wind turbine technology has experienced advancement from the Danish concept, the DFIG design, to the latest synchronous generator turbine especially the PMSG concept. The Danish wind consultation company MAKE predicts the PMSG wind turbine will be the next dominant product in the world wind market barring any unexpected upsurge in the price of permanent magnet materials. In order to clarify the respective characteristics, this section presents the comparison of the aforementioned turbine architectures on the basis of major hardware components required, operation region, and energy output.

Table 2.1 Characteristics summary of wind turbine configurations

Turbine type	**Fixed speed**	**Partial variable speed**	**Variable speed**				
Generator	**SCIG**	**WRIG**	**PMSG**	**SG**	**SCIG**	**DFIG**	**SRG**
Active power control	*Limited*	*Limited*	*Yes*	*Yes*	*Yes*	*Yes*	*Yes*
Reactive power control	*No*	*No*	*Yes*	*Yes*	*Yes*	*Yes*	*Yes*
Blade control	*Stall/Pitch*	*Pitch*	*Pitch*	*Pitch*	*Pitch*	*Pitch*	*Pitch*
Converter rating	*No*	*Small*	*Full scale*	*Full scale*	*Full scale*	*Partial scale*	*Full scale*
Drive type	*Gear box*	*Gear box*	*Gear/ Gearless*	*Gearless*	*Gear box*	*Gear box*	*Gear box*
Speed range	*Fixed*	*Limited*	*Wide*	*Wide*	*Wide*	*Wide*	*Wide*
Transmission type	*HVAC*	*HVAC*	*HVAC/HVDC*	*HVAC/ HVDC*	*HVAC/ HVDC*	*HVAC*	*HVAC/ HVDC*
Grid fault robustness	*Weak*	*Weak*	*Strong*	*Strong*	*Strong*	*Weak*	*Strong*
Power transfer efficiency	*Lower*	*Low*	*High*	*High*	*High*	*High*	*High*
Control complexity	*Simple*	*Simple*	*Mid*	*Complex*	*Complex*	*Complex*	*Mid*
Generator cost	*Cheap*	*Cheap*	*Expensive*	*Expensive*	*Cheap*	*Cheap*	*Cheap*
Converter cost	*No*	*Cheaper*	*Expensive*	*Expensive*	*Expensive*	*Cheap*	*Expensive*
Weight	*Light*	*Light*	*Light*	*Heavy*	*Light*	*Light*	*Light*
Maintenance	*Easier*	*Easier*	*Easy*	*Easy*	*Easy*	*Difficult*	*Easy*

In [37], several different generator systems for wind turbines, namely the DFIG with three stage gearbox, the direct drive synchronous generator, the direct drive PMSG, and the DFIG with single stage gearbox, are presented to compare, based on cost and annual energy yield for a given wind climate. The DFIG with three stage gearbox is the cheapest solution because of standard components. Paper [38] compared the three main wind turbine types: fixed speed induction turbine, DFIG turbine and PMSG with full scale power converter in terms of the corresponding requirements for conventional power plant, such as power factor control, reactive power regulation, stability improvement and so on.

As consideration of these characteristics, a summary of wind turbines configurations is shown in Table 2.1. Each operation performance is presented in order to clarify the corresponding characteristics.

2.5 Grid regulation for wind turbines/plants

In the early years of commercial wind power, wind energy was only a small percent of total grid capacity. Also, wind turbines were normally connected at the medium-voltage level collections. Thus there was no need for special sets of rules to regulate operation. Like other distributed power generators, wind turbines were merely expected to be neutral players. In other words, it is not required to consume or produce much reactive power and allow switching off wind turbines as quickly as possible if there are any problems in networks, such as, short circuit, voltage swells or sags, or deviation in frequency.

However, the share of wind power in individual grids grew rapidly in the recent years, and thereby wind power currently made up a large amount of electricity demand in some regions during strong wind seasons. As the size of wind farms increased, their connections to high-voltage and extra high-voltage grids will became more common. For instance, some offshore wind farms will be planned to connect at these levels. In addition, sparsely populated areas generally do not have strong grid utilities, although a lot of wind power may be available in such areas.

Hence, manufacturers of wind turbines and grid operators face technical challenges of grid compatible turbines. For the past few years, they have been working with research institutes to develop new control systems for wind turbines in order to come up with more

and more stringent rules for grid connected wind turbines. According to the codes released by Energinet, E.On Netz (E.ON), Western Electricity Coordinating Council (WECC) [6], the technical requirements have been defined for the grid connected wind turbines. The common requirements in most of grid codes can be classified into the following issues: ride-through ability of wind turbine, control of voltage and reactive power, active power and frequency regulation, and power quality issues. The aforementioned four issues will be investigated in the following sections.

2.5.1 Ride-through ability of wind turbine

There is ambition to integrate a large amount of wind power into grid and to increase the share of energy consumption that is produced by wind turbines. The disconnection of wind turbines after a fault in the network may provoke the loss of the load. Especially, this could be extremely dangerous where there is a large concentration of wind power system close to the fault point. Hence, the interaction between the grid and the turbine becomes increasingly important in the power system safety operation [4]. This can be understood as follows. When all wind turbines would be disconnected in case of a grid failure, these wind turbine generators will, unlike conventional power plants, not be able to support the voltage and the frequency of the grid during and immediately following the grid failure. This would cause major problems for the systems stability. Hence, it is worldwide recognized that the turbines should remain connected to the grid in case of a failure in order to enable large-scale application of wind energy without compromising system stability. They should supply active and reactive power for frequency and voltage support immediately after the fault has been cleared, which is normally within a fraction of a second.

Due to this requirement, system operators in many countries have recently established transmission and distribution system grid codes that specify the range of voltage conditions for which wind turbines must remain connected to the power system. These are commonly referred to as the fault ride-through specifications.

In July 2004, the wind-farm transmission grid code was released in the Republic of Ireland. The fault ride-through requirements for wind turbines connected to the Irish

transmission system are specified in [39]. A wind farm shall remain connected to the transmission system for transmission system during voltage dips on any or all phases, where the transmission system voltage measured at the high voltage terminals of the grid connected transformer should be within the voltage requirements. Additionally, in Northern Germany, where the concentration of wind turbines is high, the grid operator (E.On, Netz) has already set requirements for the behavior of wind turbines. Instead of disconnecting them from the grid, the turbines should be able to follow the characteristic shown in Fig.2.15. Only when the grid voltage goes below the curve (in duration or voltage level), the turbine is allowed to disconnect. Otherwise, when the voltage is above the curve, the turbine should supply reactive power.

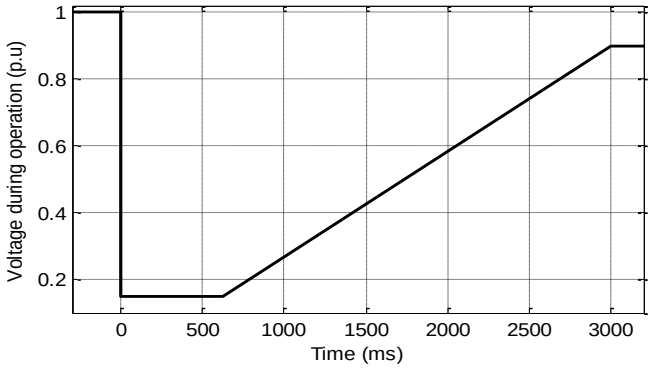

Fig.2.15 Typical fault ride-through requirement of wind farm

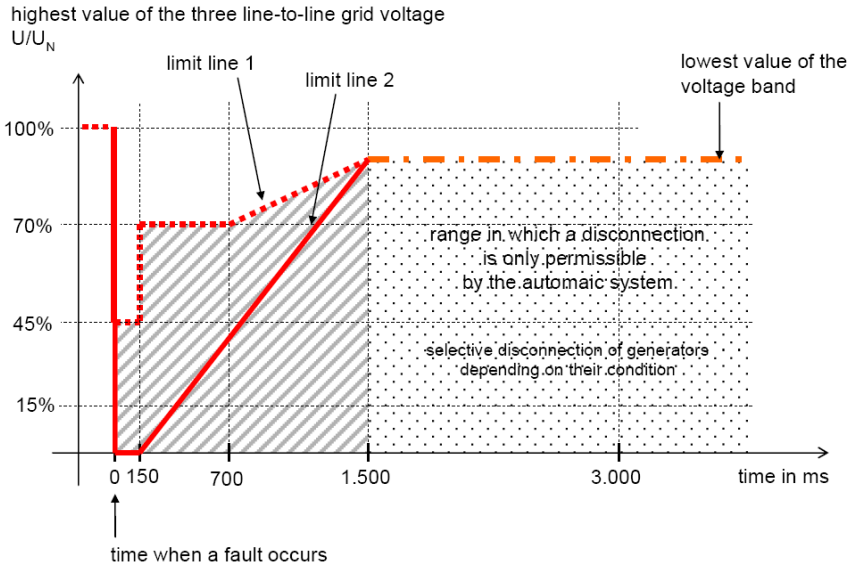

Fig.2.16 More stringent fault ride-through requirements of wind farm

Most recently, the E.ON has updated its grid code for wind farm ride through requirement as illustrated in Fig.2.16 since the rapid increase of wind power penetration. Three-phase balanced faults should not lead to the disconnection of the wind turbines from the grid above the red solid line (limit line 2) shown in Fig.2.16. Below the limit line 2, the turbine is allowed to disconnect from the grid. From Fig.2.16, the grid operators have demanded wind turbine capable to ride through zero voltage within several hundred milliseconds. Active power output must resume immediately following fault clearing and be increased with a gradient of at least 20% of the rated power per second. The active power increase can take place at 5% of the rated power per second within the area between the red dot (limit line 1) and solid lines (limit line 2). Moreover, the additional reactive current has to be supplied by the generating plant during a voltage dip to support the grid voltage. The reactive current is proportional to the severity of voltage sags. The purpose of injecting reactive current is to assist the grid on recovering its rated voltage.

2.5.2 Control of voltage and reactive power

Wind farms are often installed in remote areas and therefore reactive power has to be transported over long distances resulting in power losses. Recent grid codes demand from wind farms to provide reactive output regulation in response to power system voltage variations, as for the conventional power plants. Hence, reactive power control is important for wind farms and network. Since the reactive power injection to the network is dependent on the network short-circuit capacity and impedance, the requirements of reactive power control are related to the network characteristics.

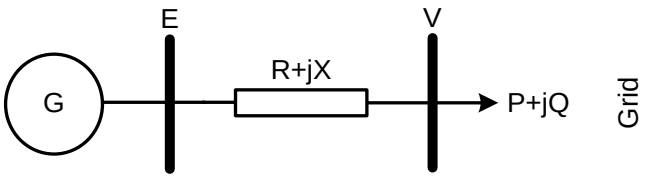

Fig.2.17 Single line diagram of a grid connected wind generation system

To explain the importance of the reactive power control, a simplified power system model with a generator at the sending end, a power transmission line and a grid-side bus named

point of common coupling (PCC) at the receiving end are shown in Fig. 2.17. Let E and V be the voltage at the sending and receiving end, respectively. The power line has a resistance R and a reactance X. P and Q are the transmitted active and reactive power at the receiving end. The voltage deviation between the sending end and the receiving end is

$$\Delta V = E - V = (R + jX)(\frac{P - jQ}{E}) \approx \frac{RP + XQ}{E} \tag{2.1}$$

In most network, $X \geq R$ and hence,

$$Q \propto \Delta V \tag{2.2}$$

From (2.2), the magnitude of the voltage deviation is controlled by the reactive power exchange. The reactive power flow between the generation and the load in the power system must be balanced in order to avoid large voltage excursion.

When a fault happens, there is a voltage drop along the network circuit proportional to fault current and to distance from the substation. Wind farms are usually located in remote locations, the distance to the substation may be very long and the connection may be radial. In this case the impedance is often quite large and thereby the voltage drop is significant. However, the regulator in the substation may not be able to recover the voltage at the connection of the wind farm without exceeding its voltage limits. Therefore, voltage control capability of the wind farm is very useful to keep the voltage profile along the system.

Voltage regulation and reactive power control are fundamentals in the distribution of electric energy. As depicted in (2.2), the voltage deviation across a transmission line determines the reactive power flow in the line or vice versa. Thus, for a given active power output, the conventional generator's Automatic Voltage Regulator (AVR) is used to determine its terminal voltage magnitude in order to supply or absorb to the transmission system the desired amount of reactive power. A mismatch between the supply and demand of reactive power results in a change in the system voltage. For instance, if the supply of lagging reactive power is less than the demand, a decrease in the system voltage results. Otherwise, if the supply of lagging reactive power is more than the demand, there is an increase in system voltage. There are stringent requirements on the

extent to which the system voltage can be allowed to deviate from its nominal values [40] ($\pm 10\,\%$ for low voltage networks and $\pm 5\,\%$ for medium or high voltage networks).

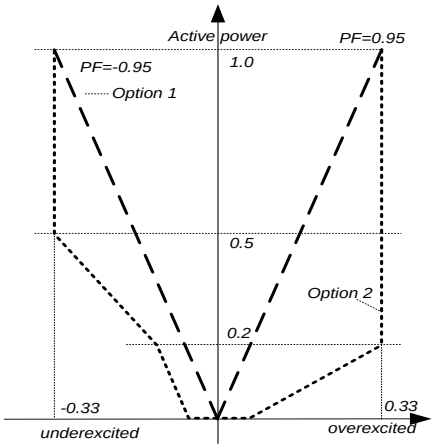

Fig.2.18 Power factor requirement for wind farm integrated to grid

Some codes prescribe that the transmission system operator may define a set-point value for voltage or power factor or reactive power at the wind farm's connection point. Since there are strict requirements on the extent to which the system voltage can be allowed to deviate from its nominal values, several countries have already clarified these issues in their grid codes [41]. For instance, E.ON interconnection agreements require wind farm operator to maintain power factor (PF) between 0.95 leading and 0.95 lagging [40] which is presented in Fig.2.18. When the generating unit is providing low active power, the power factor may deviate from unity because it can support additional leading or lagging currents due to the reactive power demanded by the utility. When the generating unit is working under the nominal condition, the power factor must be kept close to unity otherwise there will be excessive currents. On the other hand, as the reactive power is locally generated and consumed locally, the current through all upstream devices and the power losses in the network can be reduced. Hence, the wind farm should have the capability to control the voltage and the reactive power at the connection point. This is essential to ensure secure operation of the system.

For instance, some grid codes prescribe that wind farms should support the grid by generating reactive power during a network fault, to support and faster restore the grid voltage. The E.ON requires wind farms to support grid voltage with additional reactive

current during a voltage dip, or increased reactive power consumption in the event of a voltage swell. The voltage control must take place within 20 ms after fault recognition by providing additional reactive current on the low voltage side of the wind turbine transformer amounting to at least 2% of the rated current for each percent of the voltage dip. A reactive power output of at least 100 % of the rated current must be possible if necessary. The above applies outside a ± 10% dead band around nominal voltage. According to the Spanish grid code, wind power plants are required to stop drawing reactive power within 100 ms of a voltage drop and to be able to inject reactive power within 150 ms of grid recovery. Finally, Great Britain and Ireland specify in their grid codes that wind farms must produce their maximum reactive current during a voltage dip caused by a network fault.

2.5.3 Active power and frequency regulation

In the conventional grid codes, active power control requirement is defined as an ability to adjust the active power output with respect to the frequency deviations and the orders coming from the transmission system operators (TSO). It is well-known that a mismatch between the generation and load for active power is a change in the rotational energy stored in the rotating mass of the generators: a drift in the system frequency. A surplus in generation creates a frequency increase, and a shortage in generation leads to a decrease of the frequency. Hence, all the generating equipments in an electric system are designed to operate within a stringent frequency margin. Grid codes specify all generating plants should be also able to operate within a frequency range around the nominal frequency [42-44]. The strictest continuous operation limit for frequency appears in the British code (47.5-52 Hz). It is obvious that the most extreme frequency limits 46.5 Hz and 53.5 Hz are for E.ON offshore.

The goal of these new rules is to move beyond treating wind turbines as passive generators that are ideally ‘neutral’ and merely latch on to the ‘actual’ grid structure. However, nowadays, they are to be used as active elements in transmission and distribution grids. Their technical properties should allow them, for instance, to react appropriately to changes in active power and frequency or to overloads in certain lines in order to increase the quality of power supply instead of being a burden.

On the other hand, considerably larger variations of power production may occur at and after extreme wind conditions. The power output of a wind farm can vary rapidly and lead to additional imbalances between production and consumption in the system. It would deteriorate the frequency control in the wind power connected transmission systems.

In Germany, E.ON and Vattenfall have come up with grid connection guidelines for their zones, and the VDN has also created a set of rules as an independent association. In addition, a number of other countries in Europe and elsewhere are currently developing similar rules for their own situations. According to the German code, when frequency exceeds the value 50.2 Hz, wind farms must reduce their active power with a 0.4 pu/Hz gradient (40% of the available power of wind plant). The British code requires that wind farms larger than 50 MW to have a frequency control device capable of supplying primary and secondary frequency control, as well as over-frequency control. It is remarkable that it also prescribes tests, which validate that wind farms indeed have the capability of the demanded frequency response. In Spanish grid code, wind farm must be able to give active power increase or decrease active power output proportional to the frequency deviation at the connection point. The frequency control must work as a droop controller of which values vary between 0.02 and 0.06 pu based on wind power plant ratings. Speed of the response will be adjustable 10% of the rated capacity in 250 ms.

These rules for grid connections mainly concern power limitations for individual wind turbines or entire wind farms, such as increasing or reducing output at preset increments in certain situations, or specifications of the output factors that wind farms must provide. In this way, standby power can be provided over periods of minutes or seconds.

2.5.4 Power quality issues

Power quality issues are addressed especially for wind turbines connected to the medium voltage grid utility. Some grid codes, such as Denmark and Ireland have established the corresponding requirements at the transmission level. Two main standards named by EN 50160 and International Electrotechnical Commission (IEC) 61000-X-X are used to define the power quality parameters. The fast variations in voltage, short term flicker

severity, long term flicker severity and the total harmonic distortion (THD) would be specified in these standards.

The IEC initiated the standardization on the power quality for wind turbine since 1995 as part of the wind-turbine standardization, and ultimately in 1998 IEC issued a draft IEC-61400-21 standard for "power-quality requirements for Grid Connected Wind Turbines". The methodology of that IEC standard consists of the following three considerations.

The first one is the flicker analysis. The IEC-61400-21 specifies a method that uses current and voltage time series measured at the wind-turbine terminals to simulate the voltage fluctuations on a fictitious grid with no source of voltage fluctuations other than the wind turbine switching operation. The second one regards switching operations. Voltage and current transients are measured during the switching operations of the wind turbine (startup at cut-in wind speed and startup at rated wind speed). The last one is the harmonic analysis, which is carried out by the fast Fourier transform (FFT) algorithm. Rectangular windows of eight cycles of fundamental frequency width, with no gap and no overlapping between successive windows, are applied. Furthermore, the current THD is calculated up to 50th harmonic order.

Recently, high-frequency harmonics and inter-harmonics are treated in the IEC 61000-4-7 and IEC 61000-3-6. The methods for summing harmonics and inter-harmonics in the IEC 61000-3-6 are applicable to wind turbines. In order to obtain a correct magnitude of the frequency components, the use of a well-defined window width, according to the IEC 61000-4-7, Amendment 1, is of a great importance. Modern forced-commutated inverters used in variable-speed wind turbines produce not only harmonics but also inter-harmonics, i.e., harmonics that are not a multiple of 50 Hz. Since the switching frequency of the inverter is not constant but varies, the harmonics will also vary. Consequently, since the switching frequency is arbitrary, the harmonics are also arbitrary. Sometimes they are a multiple of 50 Hz, and sometimes they are not.

Such sets of rules, guidelines can be used to predict the response of entire wind farms before they have even been installed. This information then serves as the basis for negotiations of grid connection agreements between operators of wind farms and grid operators.

2.6 The potential challenges for grid-connected wind turbines

According to the grid requirements presented in Section 2.5, the ideal wind turbine should have a good ride-through characteristic to deal with any grid disturbances and faults; be able to provide good grid support, such as reactive current for voltage regulation; have flexible active power regulation, harmonics-free characteristic and high reliability, especially for offshore wind turbines.

2.6.1 Fault ride-through enhancement for DFIG wind turbine

The latest grid codes have clarified the low voltage ride through ability of the grid connected wind turbine in Section 2.5.1. When the network suffers a fault, the turbine is required to keep connection, and most importantly, the reactive current is demanded to inject into the network according to the latest grid codes. The aim is to help the network voltage recovery.

The power electronics converter used in DFIG is only 20%~30% of the generator rating, which is determined by the speed operating range of DFIG. This is the significant advantage of DFIG turbines. Hence, more than 50% of the installed turbines in the last decade are using the DFIG configuration. However, since the stator windings of DFIG are directly connected to the grid utility via a three-phase transformer, the performance of DFIG is very sensitive to any grid disturbances, such as voltage sags, swells. Thus severe voltage sags and the resulting stator flux place a significant electrical stress on the rotor-side converter and thereby increase mechanical stress on the gearbox as well [37, 45]. Consequently, the DFIG fails to satisfy with the aforementioned ride-through requirements if no additional protection is adapted. To cater the latest grid requirement, it is necessary to develop ride-through strategies for DFIG.

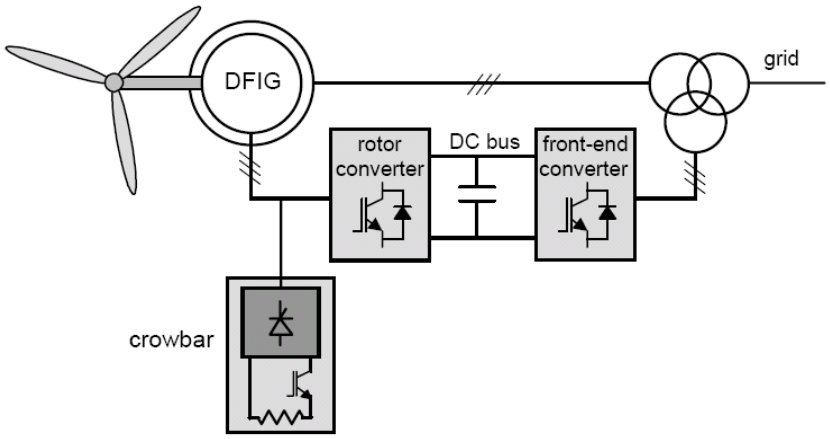

Fig.2.19 DFIG ride-through enhancement with crowbar circuit

Wind generation system is basically equivalent to variable speed pump/fan drive system operation in regenerative mode. Fault studies on induction motor drives [46] are potential to transfer to solve the problem faced in DFIG system. In the literature, several solutions have been proposed to improve ride-through capability of DFIG. Using serial dynamic braking resistors applied to the stator windings during a voltage sag [47] has been shown to be able to reduce torque and current spikes in the DFIG, and thereby prevent rotor-side converter damage during voltage sag conditions. Two improvements of the rotor circuit by introducing either a silicon controlled rectifier (SCR) rotor crowbar circuit [48-50] or a three-phase rectifier and adjustable resistive load [51] have demonstrated enhancement in the DFIG ride-through capability. Figure 2.19 shows the crowbar circuit for DFIG ride-through enhancement. The selection of the crowbar resistance is the key factor to reinforce the ride-through capability of DFIG. Too small a resistance will fail to limit the rotor-side spike current during fault transients, but too large resistance can also cause the overvoltage phenomenon on the rotor-side converter. Both of these two cases will degrade the ride-through performance of crowbar method for DFIG. Recently a combination of crowbar circuit and series dynamic resistor has been installed in the rotor circuit of DFIG, which exhibits good protection during grid faults, especially unsymmetrical disturbances compared to the conventional crowbar [52]. In addition, an improved rotor side control principle has been shown to protect the rotor-side converter while DFIG terminal voltage is stepped down to nearly 30% of nominal [53, 54]. This solution, however, requires large capacity of current in the rotor converter and cannot deal with the severe voltage sags, such as zero-voltage ride-through. The integration of a short-term energy storage device in a DFIG design has also shown the improvement of ride-

through ability compared to the conventional topology [55]. In addition, voltage or current source inverter based flexible AC transmission devices [56, 57] have been used for flexible power flow control, secure loading, and damping of power system oscillation, which is potential for wind turbine ride-through enhancement.

Most importantly, much more stringent grid codes are being established nowadays as mentioned in Section 2.5.1 since wind power penetration into electric grid gets larger. According to the latest regulations as illustrated in Fig.2.16, wind turbines are not only required to remain connected to ride through the grid faults, but they are also demanded to inject reactive current in order to assist the grid in recovering its rated voltage. However, the braking resistor or the crowbar technology does not fulfill the latest codes, as the turbine cannot supply reactive current / power during the activation of the braking resistor or the crowbar circuit. In other words, it is impossible to control the reactive power flowing into grid during fault periods using the aforementioned ride-through enhancements although they are effective to protect the turbine itself.

In order to satisfy with the latest codes, the rotor-side and grid-side converter reconstruction has been presented together with an optimized time setting of crowbar cutting-in and removal, with aims to protect DFIG and provide reactive current during faults [58]. A novel control strategy that notably reduces the crowbar activation time is presented in [59]. As a result, the control of the turbine may shortly be resumed and the turbine can furthermore supply a reactive power fulfilling the newest grid regulations.

On the other hand, researchers are addressing the issue from the angle of FACT devices. Voltage or current source inverter based FACTs devices, such as static var compensator (SVC), static synchronous compensator (STATCOM), dynamic voltage restorer (DVR) have been used for flexible power flow control, secure loading, and damping of power system oscillation [60, 61]. Some of those are even applicable to wind farm stabilization [62-64]. The STATCOM composed of power electronics devices has already been proposed to enhance the ride-through capability of wind farms. However, it is still challenging to deal with severe voltage fault since its shunt compensation essential. Moreover, compared with a parallel reactive power compensator, a series compensator is much more effective to restore voltage in strong grid utility in terms of minimizing the power capacity of devices [65].

Bearing all these in mind, a series compensator based ride-through architecture for DFIG and its advanced control will be investigated in Chapter 3 to cater the latest grid regulations.

2.6.2 Power architecture improvement for PMSG wind turbine

As predicted by the Danish wind consultation company MAKE in 2010, the PMSG will be the next mainstream generator technology barring any unexpected upsurge in price of permanent magnet materials. The worldwide wind turbine manufacturers, such as Vestas, GE Wind, and Siemens have been interested in the design and application of PMSG based wind turbines.

PMSG is much more popular because of its higher efficiency, high-power density, and robust rotor structure. The simple and robust low speed rotor design with no separate excitation or cooling system results in minimum wear, reduced maintenance requirements, lower life cycle costs, and a long lifetime. Most importantly, PMSG exhibits good ride-through and grid support performance because of applying the full scale converter compared with DFIG. The full converter wind turbine is the most flexible wind turbine technology from an LVRT point of view, as the active and reactive power output can be controlled using the converters [66]. So far, Vestas announces its PMSG ride-through technology named as 'GridStreamer', which is able to meet the ride-through requirements.

Another significant advantage of PMSG turbine is the possibility of gearless operation. In [67], the problem to adapt a standard permanent-magnet synchronous machine to a direct-drive application is presented. A complete design of a low-speed direct drive permanent-magnet generator for wind application is depicted in [68].

It is well-known that PMSG is fed by a full scale power electronics converter whether the gear or gearless structure is adopted. Therefore, the power electronics converter plays a significant role in the PMSG turbines. A current-source converter is employed as the bridge between the generator and the grid for high-power wind energy conversion systems [69]. In [70], two current-source inverters are in series to bridge the axial flux generator and grid, which aims for MW level wind turbine application. However, the current-source converter normally introduces a lot of harmonics without advanced

filtering technologies, and thereby deteriorates power quality of the connected utilities. Hence, considering the power quality requirements, voltage-source converter with pulse width modulation (PWM) technology is more and more popular for PMSG applications, thanks to the advance of power electronics in recent years. Figure 2.9 and 2.10 presented two typical power architectures for PMSG application.

As illustrated in Fig.2.9, the PMSG is fed by a diode rectifier cascaded with a DC chopper. This system possesses merits such as simple construction and low cost. However, it lacks control capability over the generator power factor, which reduces generator efficiency. Additionally, high harmonic current distortions in the generator windings further degrade efficiency and produce torque oscillations. To address this problem, the PMSG is connected to the grid by means of a fully controlled frequency converter, which consists of a PWM rectifier, an intermediate DC stage and a PWM inverter, as shown in Fig.2.10. With this configuration the generator-side converter can completely regulate the generator in terms of speed, power factor and electromagnetic torque. However, the configuration reliability is relatively low due to the potential existence of shoot-through states arising from gate-drive failures. Thus there is motivation to overcome the aforementioned limitations.

Recently, research on the three-switch buck-type rectifier has focused on grid-side current quality improvement [71, 72], design and implementation [73], and parallel operation [74]. On the other hand, current research on Z-Source inverters has focused on modeling and control [75, 76], PWM strategy [77], Multi-level implementation [78], application and performance improvement [79, 80], and other variants of the Z-Source network [81-83]. However, detailed design of a PMSG grid interface system based on the integration of the three-switch rectifier and the Z-Source inverter has not been reported.

The motivation to use Z-Source inverter for feeding good-quality power into grid comes from the highly reliable operation of the topology. The Z-Source inverter does not have the short-circuit risk associated with conventional inverter topologies. Moreover, fewer harmonics are presented in the Z-Source inverter compared with the conventional inverter due to the elimination of the commutation dead-time. In addition, the three-switch rectifier also has high reliability characteristics compared to the conventional bridge rectifier. There is no shoot-through phenomenon in the rectifier. This is a very important

issue in PMSG application since short-circuit of PMSG would rapidly result in over-current in the stator windings. Therefore, if any of three switches is shorted or malfunctioning, the PWM rectifier can still be operated as a normal diode rectifier after detecting the fault-event. Hence, the integration configuration can overcome the aforementioned drawbacks of existing configurations, and provides high reliability, low capital cost, and harmonic-free characteristics in both generator and grid sides.

The proposed architecture for PMSG and its control in this thesis has been developed with the above issues in mind. First of all, it is necessary to explore the integration topology named as the three-switch buck-type rectifier with Z-Source inverter in terms of modulation, circuit analysis and validation before doing the system-level integration for PMSG based wind turbine. A unified modulation for both the machine-side and grid-side converters will be given in order to prevent the negative interaction between the two converters. To achieve variable speed operation of PMSG, the buck-boost capability is required for the developed topology. Hence, equivalent circuit analysis of the aforementioned topology will be provided to study the voltage transfer ratio, which gives fundamentals for variable speed PMSG turbine.

In this thesis, the modulation, analysis and demonstration of the three-switch buck-type rectifier with Z-Source inverter will be introduced in Chapter 4 with aims to clarify the proposed topology and essential behavior. Then the design methodology, the simulation studies and experimental validation of the proposed architecture for PMSG wind application will be presented in Chapter 5.

2.6.3 Potential methods to quantify wind power impacts

As mentioned in Section 2.2, wind power capacity will have a significant percentage of the worldwide electricity demand in the next decade, such as in western European countries. It can be predicted that the output power of wind farm will be large enough to affect the voltage regulation of the connected utility as mentioned in Section 2.5.2.

These developments clearly indicate the need to search for effective solutions to alleviate any of the negative impacts the wind generators may have on the grid so that the benefit of the renewable energy source can be maximized. For example, a possible solution is to

incorporate energy storage devices into the network [84]. However, this or any other solution will incur additional cost to the system. Thus, there is a need to devise reliable method(s) to accurately quantify the impacts so that the most appropriate and economical solution to mitigate the impacts can be obtained. It is noted that voltage quality is essentially dependent on the amount of wind power injection and the effective impedance characteristics of the external network connected to the wind generators. Hence, it will be necessary to consider together both the injected power and network impedance characteristics when assessing the impacts of wind generation on network voltage.

Toward this end, deterministic analysis approaches have been proposed in [85, 86]. As the methods involve relatively simple calculations, they require low computation time. The deterministic approaches assume known loads, generation and network conditions. Often only maximum/minimum wind generation conditions at extreme network conditions are considered, without taking into consideration the likelihood of their occurrence. The solution methods obtained to control network voltage may therefore be unnecessarily expensive or complex, as they would only be used for events or instances which may have very low probability of occurrence. It is perhaps in recognition of this observation that for general application study on power quality, new standards such as that discussed in [87, 88] prescribes voltage quality performance measured in statistical terms. The industry trend is indicating that statistical and probabilistic approaches are gaining in importance in voltage quality assessment study.

Recognizing the shortcoming of deterministic methods, the authors of [89] suggested the use of discrete Markov modeling technique to describe wind speed. Voltage profile at selected buses can be obtained through conventional load flow study by applying the derived wind power to a given distribution network. The voltage profile can also be described in probabilistic manner. However, the authors still considered the wind farm connected network to be essentially a deterministic system. In practice, this assumption is unlikely to be valid because network status changes as loads and generation levels vary. The authors of [90] have also derived an alternative probabilistic model to study the impact on external system, due to an aggregate of wind-powered induction generators with fluctuating input mechanical power. Reference [91] proposed a simpler computational method in which the mean values of the wind farm output power and external load level are used to evaluate the voltage profile at the point of common

coupling. Again the authors in [90] and [91] have used a deterministic Thevenin equivalent model to represent the external network. Finally reference [92] proposed to treat the injected wind power in a statistical manner, where network voltage is evaluated using probabilistic load flow (PLF) solution technique. Similarly, reference [93] considered operational uncertainties (including e.g. daily time varying load, stochastic wind power generation, varying network reconfiguration) to assess voltage quality using PLF study. Thus both methods in [92, 93] will require extensive input data which may not be readily available. The computational burden of the technique can be expected to be high.

The method proposed in this thesis has been developed with the above issues in mind. The proposed method calculates the impact of wind power penetration on network voltage in a statistical manner: the wind power injection and the state of the connected grid are described in terms of probabilistic distributions. The detailed analysis will be explained in Chapter 6.

2.7 Conclusion

This chapter has reviewed the existing wind turbine configurations and current grid codes for wind power penetration. Among the aforementioned turbine configurations, the DFIG has a poor ride-through performance, which is inadequate to satisfy the ride-through requirements if no protection is provided. However, more than 50% of the installed turbines in the last decade are based on the DFIG configuration. To make these turbines to still comply with the new grid codes, it is very important to reinforce its ride-through characteristic. Hence, this will be one of the research directions in this thesis.

Compared with DFIG, PMSG exhibits good ride-through and grid support performance because of application of the full scale power converter. As predicted by the Danish wind consultation company MAKE, the PMSG will likely be the dominant technology in the next decade. It is well-known that power electronics converter plays a significant role in the PMSG turbine in terms of system integration, reliability and power quality. Therefore, investigating advanced power architecture is one of the key tasks for PMSG based turbines.

Regardless of DFIG or PMSG, wind power capacity will have a significant percentage of the worldwide electricity demand in the next decade. Consequently, wind power will significantly affect the operation of utility in terms of voltage regulation, frequency control and so on. Thus, there is a need to devise reliable methods to accurately quantify the impacts so that the most appropriate and economical solution to mitigate the impacts can be obtained. Hence, one of the potential researches is to develop a feasible voltage quality analysis for large wind power penetrated networks, which aims to eliminate the related negative impacts.

All these three directions have been investigated and analyzed in this project and will be described in details in the subsequent chapters respectively.

CHAPTER 3

RIDE-THROUGH ENHANCEMENT OF DFIG WIND TURBINES BASED ON SERIES VOLTAGE COMPENSATION

3.1 Introduction

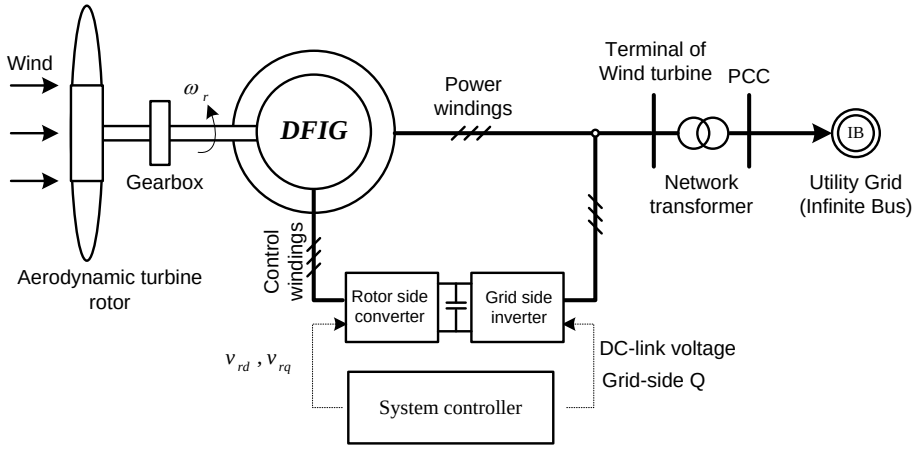

Fig.3.1 A wind generation system based on doubly fed induction generator

The DFIG is a common sub-system for large variable speed wind turbines that are connected to a grid. A diagram of wind energy system based on DFIG is shown in Fig. 3.1. The DFIG is driven by a horizontal-axis wind turbine. The power windings of the generator stator are connected directly to the utility grid. The control windings of the generator rotor are connected to a back-to-back converter, where the rotor-side converter is used to control the rotor current of the generator and the grid-side converter is utilized to control the DC-link voltage. With stator–flux orientation, a vector-control for DFIG is adapted to generate the reference of V_{rd} and V_{rq} for the rotor-side converter, decoupling generator torque and excitation control. Meanwhile, a vector-control approach is also used for the grid-side inverter with a reference frame oriented along with grid voltage vector position, enabling independent control of active (DC-link voltage) and reactive power (Q) flowing between grid utility and grid-side inverter.

Since the control of the DFIG is tied to the rotor windings, only slip power is processed by the power electronics converter, where the purpose of the converter is to synchronize the rotor current with respect to the stator reference of the DFIG. However, since the stator windings of DFIG are directly connected to the utility grid via a three-phase transformer, the performance of DFIG is very sensitive to any grid disturbances, such as voltage sags and swells. It is therefore necessary to explore ride-through enhancements for DFIG based turbines.

Several ride-through enhancement solutions have been reviewed in Chapter 2. To address the potential challenges of existing ride-through methods as mentioned in Section 2.6.1, an integration of a series voltage compensator in the stator of the DFIG to reinforce its fault ride-through capability is introduced in this chapter. Prior to introducing the control of series compensator, the control of DFIG system is firstly presented to give the fundamentals for its ride-through analysis. Then the essential behavior of the DFIG during the fault condition is analyzed using system phasor diagram. Subsequently, the general control scheme for the series compensation system in case of grid faults is presented. However, the conventional control scheme would result in the high cost of the ride-through method. Hence, to reduce the cost of series voltage compensator, this chapter also proposes a customized control solution to regulate the series voltage compensator. This is the significant contribution of this series compensator based ride-through method.

3.2 Fundamentals of DFIG wind turbine

3.2.1 Mathematical model of DFIG

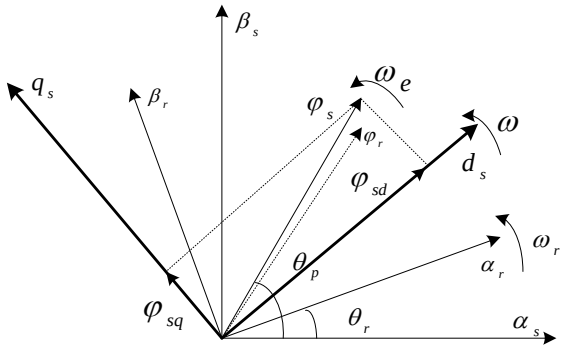

Fig.3.2 Vector diagram of the DFIG

This section investigates the control of DFIG, which gives fundamentals for the ride-through analysis. Vector diagram of the DFIG is shown in Fig.3.2. The $\alpha_s - \beta_s$ and $\alpha_r - \beta_r$ frames are the stationary two-phase frames referenced to the stator and rotor windings, respectively. As referred to the stator windings, the $\alpha_r - \beta_r$ frame is a rotating frame with the angular speed ω_r. Compared to the $\alpha_s - \beta_s$ frame, the $d_s - q_s$ frame is referred to a rotating frame when it is rotating at the angular speed ω. If the ω is chosen as the synchronous speed ω_e, the synchronous $d_s - q_s$ frame is obtained. Therefore, the equivalent circuit of a DFIG expressed in the reference frame ($d_s - q_s$ frame) rotating at a speed of ω is shown in Fig.3.3 [94]. As it is shown in the stator reference frame, the stator and rotor flux linkage vectors can be expressed as,

$$\begin{cases} \vec{\varphi}_s = L_s \vec{I}_s + L_m \vec{I}_r \\ \vec{\varphi}_r = L_r \vec{I}_r + L_m \vec{I}_s \end{cases} \tag{3.1}$$

Where, $L_s = L_m + L_{sl}$ and $L_r = L_m + L_{rl}$ are the stator and rotor total magnetic inductances. L_{sl} and L_{rl} are the leakage inductances of the stator windings and rotor windings respectively, and L_m is the mutual inductance. The stator voltage vector in the rotating reference frame is given as

$$\begin{aligned} \vec{V}_s &= R_s \vec{I}_s + \frac{d\vec{\varphi}_s}{dt} + j\omega\vec{\varphi}_s \\ \vec{V}_r &= R_r \vec{I}_r + \frac{d\vec{\varphi}_r}{dt} + j(\omega - \omega_r)\vec{\varphi}_r \end{aligned} \tag{3.2}$$

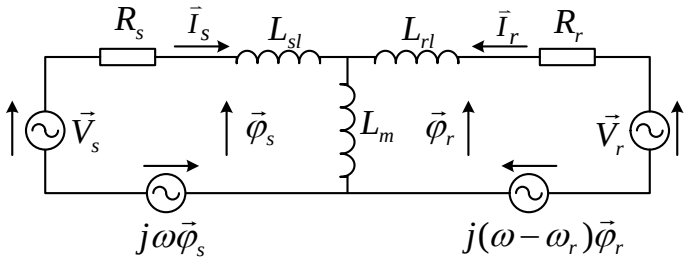

Fig.3.3 Equivalent circuit of a DFIG in the reference frame rotating at ω

Putting the vectors in (3.2) into the $d_s - q_s$ synchronous frame, (3.2) is rewritten as

$$\begin{cases} u_{sd} = R_s i_{sd} + \dfrac{d\varphi_{sd}}{dt} - \omega\varphi_{sq} \\ u_{sq} = R_s i_{sq} + \dfrac{d\varphi_{sq}}{dt} + \omega\varphi_{sd} \end{cases} \tag{3.3}$$

Where, u_{sd} and u_{sq} are the d_s - and q_s -axis components according to the rotated vector $\vec{V}_s$, respectively. i_{sd} and i_{sq} are the stator current components in $d_s - q_s$ frame.

Again, the stator and rotor flux linkage vectors in (3.1) can be also rewritten in the synchronous frame as

$$\begin{cases} \varphi_{sd} = L_s i_{sd} + L_m i_{rd} \\ \varphi_{sq} = L_s i_{sq} + L_m i_{rq} \\ \varphi_{rd} = L_r i_{rd} + L_m i_{sd} \\ \varphi_{rq} = L_r i_{rq} + L_m i_{sq} \end{cases} \tag{3.4}$$

Where, i_{rd} and i_{rq} are the rotor current components on $d_s - q_s$ frame, respectively.

3.2.2 Field oriented control of DFIG

In order to apply the field oriented control for a DFIG, a d-q transformation is required, which has been introduced in Section 3.2.1. The scheme presented in this section uses stator flux oriented control for the rotor-side converter and grid voltage oriented control is used to control the grid-side converter.

A. Control of the rotor-side converter

For high power machine, the stator resistance is usually neglected and the amplitude and rotating speed of the stator flux are constant due to the fixed grid voltage. Therefore, stator flux orientation gives orientation with the stator voltage for the MW level wind turbines.

The realization of the stator flux orientation will be carried out as follow. The d-axis is assumed to be aligned to stator flux, and the stator current coming out of the stator windings is considered positive. In the synchronous d-q reference frame ($d_s - q_s$) as illustrated in Fig. 3.3, the speed of the reference frame ω is chosen equal to the stator flux rotated speed ω_e (consistent with the grid frequency). Thus,

$$\begin{cases} \varphi_{sd} = const \\ \varphi_{sq} = 0 \end{cases} \tag{3.5}$$

On the other hand, the stator active and reactive power outputs of the DFIG can be expressed under the synchronous reference frame as,

$$\begin{cases} P_s = \dfrac{3}{2}(u_{sd} i_{sd} + u_{sq} i_{sq}) \\ Q_s = \dfrac{3}{2}(u_{sq} i_{sd} - u_{sd} i_{sq}) \end{cases} \tag{3.6}$$

Substituting (3.3), (3.4) and (3.5) into (3.6), (3.6) can be rewritten as

$$\begin{cases} P_s = \dfrac{3}{2}\dfrac{L_m}{L_s}\omega_e \varphi_{sd} i_{rq} \\ Q_s = -\dfrac{3}{2}\cdot\dfrac{L_m}{L_s}\omega_e \varphi_{sd}(\dfrac{\varphi_{sd}}{L_m} - i_{rd}) \end{cases} \tag{3.7}$$

From (3.7), it is easy to identify the active power and reactive power via the rotor side current in the given rotated reference frame. The stator flux oriented vector control strategy is used to achieve the decoupled control of the real and reactive power.

In order to control the rotor-side current, the rotor voltage vector in the rotating reference frame from Fig.3.3 is given by,

$$\vec{V}_r = R_r \vec{I}_r + \frac{d\vec{\varphi}_r}{dt} + j(\omega - \omega_r)\vec{\varphi}_r \tag{3.8}$$

According to the axis transformation in Fig.3.2, the corresponding $d_s - q_s$ axis expression can be derived as

$$\begin{cases} u_{rd} = R_r i_{rd} + \dfrac{d\varphi_{rd}}{dt} - (\omega_e - \omega_r)\varphi_{rq} \\ u_{rq} = R_r i_{rq} + \dfrac{d\varphi_{rq}}{dt} + (\omega_e - \omega_r)\varphi_{rd} \end{cases} \tag{3.9}$$

Where, u_{rd} and u_{rq} are the d_s and q_s axis values according to the rotating vector $\vec{V}_r$, respectively. i_{rd} and i_{rq} are the rotor currents on the d_s and q_s axis.

From (3.4) and (3.5), the stator current d_s- and q_s-axis components can be derived as

$$\begin{cases} i_{sd} = \dfrac{\varphi_{sd} - L_m i_{rd}}{L_s} \\ i_{sq} = -\dfrac{L_m}{L_s} i_{rq} \end{cases} \tag{3.10}$$

Substituting (3.10) into (3.4), the rotor flux d_s- and q_s-axis components can be rewritten as

$$\begin{cases} \varphi_{rd} = \sigma L_r i_{rd} + \dfrac{L_m}{L_s}\varphi_{sd} \\ \varphi_{rq} = \sigma L_r i_{rq} \end{cases} \tag{3.11}$$

Where, $\sigma = 1 - L_m^2 / (L_s L_r)$.

Again, substituting φ_{rd} and φ_{rq} in (3.11) into (3.9), the rotor voltage in (3.9) can be expressed in terms of the rotor currents

$$\begin{cases} u_{rd} = R_r i_{rd} + \sigma L_r \dfrac{di_{rd}}{dt} - (\omega_e - \omega_r)\sigma L_r i_{rq} \\ u_{rq} = R_r i_{rq} + \sigma L_r \dfrac{di_{rq}}{dt} + (\omega_e - \omega_r)\sigma L_r i_{rd} + (\omega_e - \omega_r)\dfrac{L_m}{L_s}\varphi_{sd} \end{cases} \tag{3.12}$$

From (3.12), it is found that there is cross coupling between the d_s- and q_s-axis due to the presence of the rotational EMF terms. The current loop dynamics along the d_s- and q_s-axis can be made independent by compensating for these terms in the control loops. **Figure** 3.4 shows the block diagram for the rotor-side converter to realize the field oriented control of DFIG. The stator flux estimation block is used to extract the stator flux, angle

and the synchronous speed. The stator flux is equal to the integral of the stator terminal voltage minus the voltage drop on the stator resistance. The angle and the synchronous speed can be calculated by the PLL principle [95]. The error between the reference current and the feedback current is used to generate the reference voltage of the rotor-side converter together with the compensation terms as mentioned before. Due to the reference voltage, the modulation of the converter can be carried out by sinusoidal pulse width modulation (SPWM) or SVM.

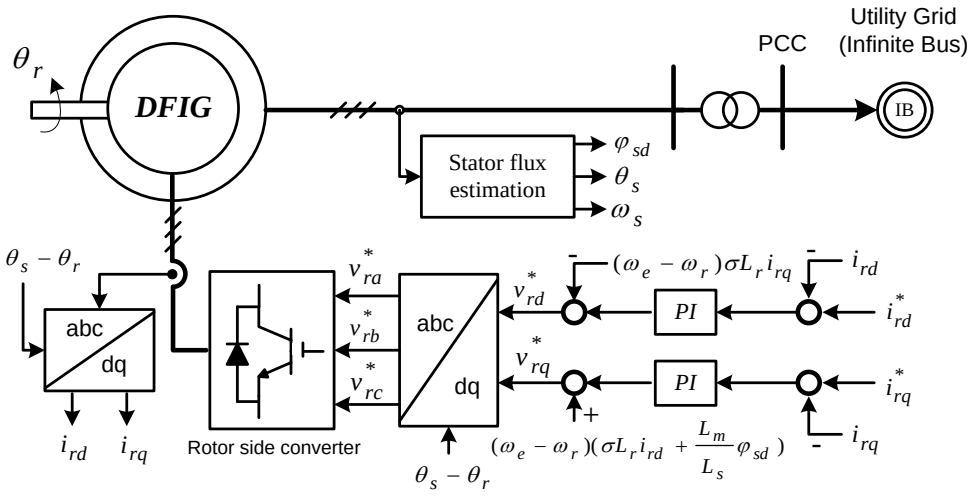

Fig.3.4 Vector control scheme for the rotor-side converter

B. Control of the grid-side inverter

When the generator is operating at the sub-synchronous speed, a grid-side converter is required to deliver power into the rotor-side converter in order to keep the DC-link voltage constant. On the other hand, when the generator is operating at the super-synchronous speed, the grid-side converter will provide the rotor power into the utility grid so as to control the DC-link voltage. Hence, the important function of the grid-side converter is to keep the DC-link capacitor voltage constant regardless of direction and magnitude of power flow. In addition, the grid-side reactive power can be regulated by the converter. A leading power factor is helpful to support grid voltage in case of any grid disturbances.

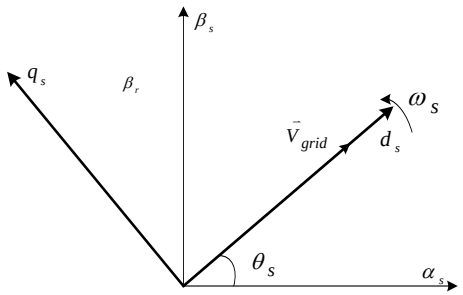

Fig.3.5 Grid voltage vector orientation for the grid-side inverter

A grid voltage vector oriented control strategy is utilized in the control of the grid-side converter, which allows decoupled control of the DC-link voltage and grid-side reactive power regulation. The voltage vector is oriented along the d-axis as shown in Fig.3.5. Herein, the grid voltage is aligned with the d-axis synchronous speed. Hence, the active and reactive power dealt with the grid-side converter can be calculated by

$$\begin{aligned} P_g &= \frac{3}{2} v_d i_d \\ Q_g &= \frac{3}{2} v_d i_q \end{aligned} \tag{3.13}$$

The energy stored in the DC link capacitor is the integral of power difference between the power delivered by the rotor-side converter and the power flowing into grid by the grid-side converter. Hence, from (3.13), the d-axis current controls the DC link voltage and reactive power is controlled using the q-axis current.

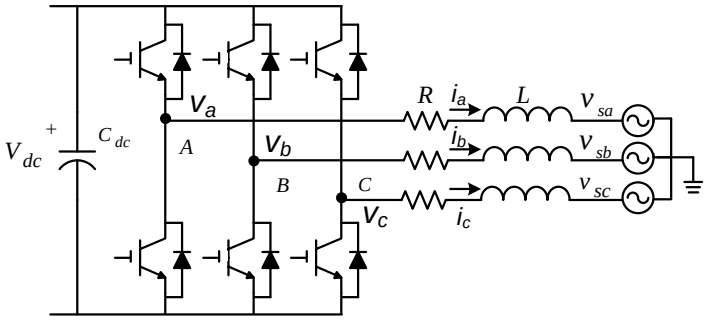

Fig.3.6 Grid-side converter arrangement

Figure 3.6 shows the arrangement of the grid-side converter. *L* and *R* are the grid-side inductance and resistance respectively. The converter is connected to the grid through the

transformer as the DC-link is operated at a relative lower voltage level. The voltage equations across the inductances and resistances are expressed as follow,

$$\begin{bmatrix} v_{sa} \\ v_{sb} \\ v_{sc} \end{bmatrix} = R\begin{bmatrix} i_a \\ i_b \\ i_c \end{bmatrix} + L\frac{d}{dt}\begin{bmatrix} i_a \\ i_b \\ i_c \end{bmatrix} + \begin{bmatrix} v_a \\ v_b \\ v_c \end{bmatrix} \tag{3.14}$$

With the transformation into a d-q synchronous frame as shown in Fig.3.5, the d- and q-axis voltage components can be written from (3.14) as

$$\begin{aligned} v_{sd} &= Ri_d + L\frac{d}{dt}i_d - \omega_s L i_q + v_d \\ v_{sq} &= Ri_q + L\frac{d}{dt}i_q + \omega_s L i_d + v_q \end{aligned} \tag{3.15}$$

Since the d-axis of the reference frame is aligned with the grid voltage vector, the q-axis component of the grid voltage is zero. The grid-side converter is required to supply the voltage as follow, which is rewritten from (3.15),

$$\begin{aligned} v_d &= -(Ri_d + L\frac{d}{dt}i_d) + \omega_s L i_q + v_{sd} \\ v_q &= -(Ri_q + L\frac{d}{dt}i_q) - \omega_s L i_d \end{aligned} \tag{3.16}$$

From (3.16), there is cross coupling between the d- and q-axis due to the presence of the rotational EMF terms. The current loop dynamics along the d- and q-axis can be made independent by compensating for these terms in the control loops. Figure 3.7 shows the block diagram for the grid-side converter. The stator voltage calculation block is used to extract the stator voltage magnitude, angle and the corresponding angular speed. The angle and the synchronous speed can be calculated by the PLL principle as aforementioned. The error between the reference DC-link voltage and the corresponding feedback serves as the reference current of the inner current loop. The d- and q-axis components are utilized to control the DC-link voltage and the grid-side reactive current, respectively. The reference voltage of the grid-side converter is obtained by combining the outputs of the inner current loop and the aforementioned compensation terms.

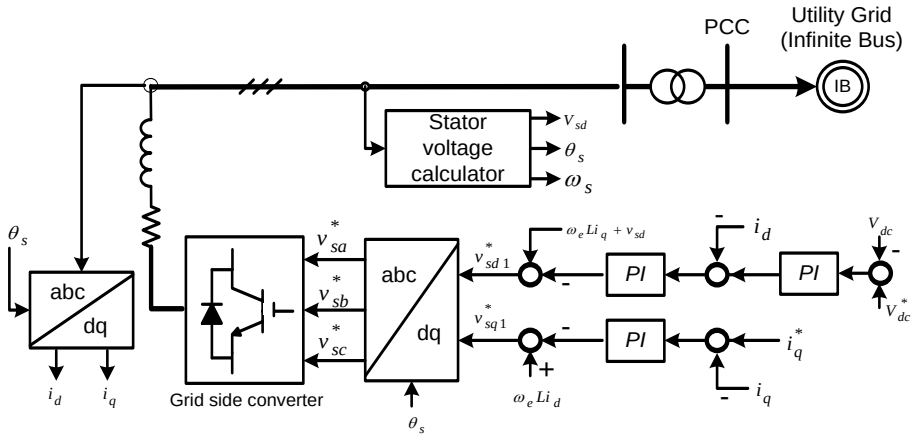

Fig.3.7 Vector control scheme for the grid-side converter

C. System control diagram considering turbine's characteristic

For a horizontal-axis wind turbine, the captured wind power is a function of wind speed and can be expressed as [96]:

$$P_W = \frac{1}{2}\rho A v^3 \times C_p \tag{3.17}$$

Where, P_W is the wind power production of wind turbine. ρ is the air density (kg/m^3)(At $15^0 C$ and 1 atm, $\rho = 1.225 kg/m^3$), A is the cross-sectional area of wind turbine (m^2) ($A = \pi \cdot r^2$ with wind turbine radius of r), and v is wind speed (m/s). C_p is the power coefficient of wind turbine.

For a given wind speed, the power transferred coefficient C_p is a function of the rate at which the wind turbine turns. If the turbine turns too slowly, the coefficient drops off since the blades are letting too much wind pass by unaffected. In contrast, if the turbine turns too fast, the coefficient is reduced as the turbulence caused by one blade increasingly affects the blade that follows. The usual way to illustrate C_p is to present it as a function of turbine's tip-speed ratio (TSR). The tip-speed-ratio λ of wind turbine can be defined as:

$$\lambda = \frac{\omega_r r}{v} \tag{3.18}$$

Where, ω_r is the rotating angular speed of wind turbine which can be expressed by $\omega_r = k \cdot \omega_m$. Here ω_m is the generator angular speed. Normally there is a gear box between wind turbine blades and generator. The gear box ratio is k.

A non-linear relationship between C_p and λ can be obtained experimentally for any given wind turbine as shown in Fig.3.8. The rotor speed of the generator would be proportional to the wind speed in order to achieve maximum wind power.

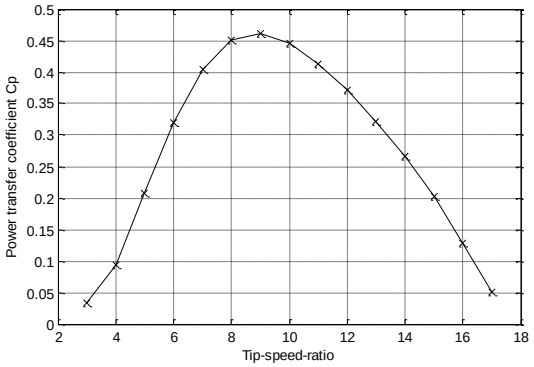

Fig.3.8 Power transfer coefficient C_p versus Tip-speed ratio λ

In order to maximize the wind power extraction, the relation between wind speed and wind power is written in a look-up table, which serves as the reference for the rotor-side converter. Due to the optimized wind power, the torque reference provided by the turbine can be expressed as,

$$T_e^* = P_w^{opt} / \omega_r \tag{3.19}$$

Where, P_w^{opt} is the maximum wind power according to the optimized tip-speed ratio.

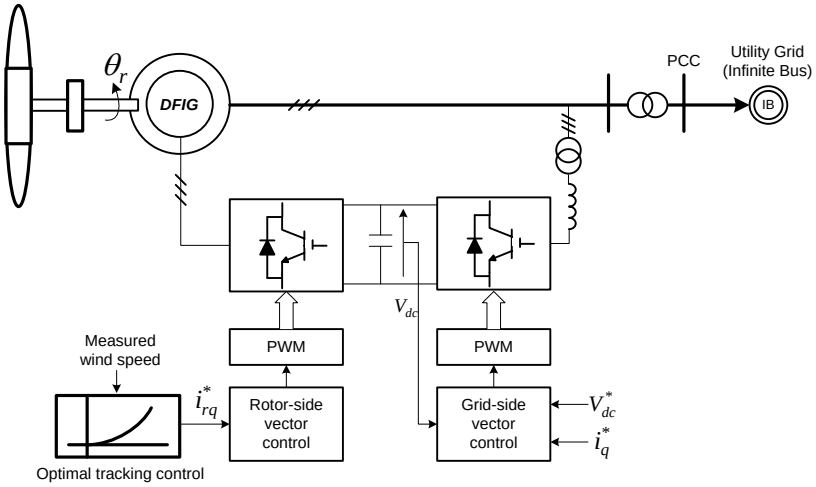

Fig.3.9 System control diagram of the DFIG based wind turbine

Figure 3.9 shows the system control diagram of DFIG to track the maximum power point of wind power. Due to the real-time measured wind speed, the theoretical maximum wind power captured and optimized rotor speed can be calculated by (3.17) and (3.18), respectively. Consequently, the torque reference can be calculated from (3.19) as well. Under the stator-flux oriented control, the rotor-side q-axis current component, i_{rq}, is proportional to the torque, and thereby the i_{rq} reference can be obtained from the torque reference. Hence, the vector control of DFIG can be implemented with the current references in the stator-flux oriented frame, which has been illustrated in Fig.3.4.

3.3 A series compensator based ride-through enhancement for DFIG

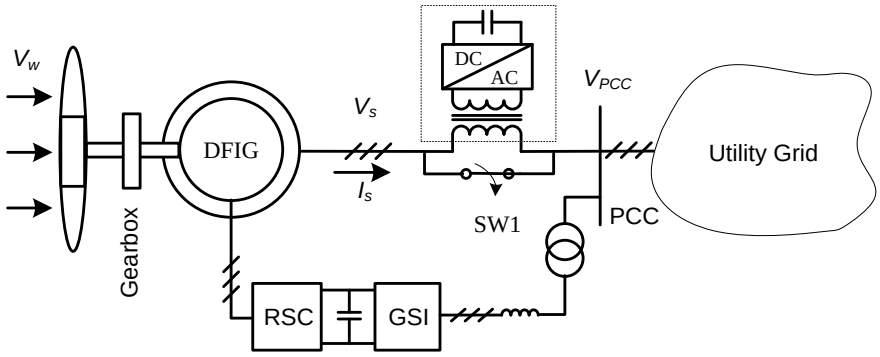

Fig.3.10 Single-line diagram of the DFIG based wind turbine connected to grid.

The general schematic arrangement of the proposed DFIG architecture is shown in Fig.3.10, which aims to enhance ride-through capability. Compared to the conventional DFIG system in Fig.3.1, the difference in the proposed structure is the utilization of a series compensator. From Fig.3.10, the series compensator is made up of a three-phase transformer and a power electronics converter with DC-link energy storage devices. The primary side of the series transformer is installed between the DFIG stator terminal and the PCC. The secondary side of the transformer is connected with the power electronics converter, which is used to generate a certain voltage during grid faults.

The principle of the series compensator is as follow. In the normal condition, the series compensator is bypassed by the power semiconductor switch SW1 (as shown in Fig.3.10) in order to eliminate the stator side impedance, which in turn, reduces system losses. As fast as monitoring the PCC voltage beyond the certain limitation, the series compensator is being in function by turning off the SW1. The function of the series compensator is to keep the stator voltage as constant when the PCC voltage suffers voltage sag during grid fault period. The advantage of the series compensated solution is to make the DFIG turbine insensitive to the grid-side disturbances. Moreover, the rotor-side converter is still in normal operation to regulate the power output of DFIG during fault periods with the help of series compensator. Thus this characteristic is not available in the conventional crowbar solution since the rotor-side converter has to be shut down during the crowbar activation. It is worthy to point out the high cost of the series compensator is the significant limitation of the series compensation solution compared to the crowbar method. In order to address this challenge, an improved control of DFIG-series compensator will be discussed in Section 3.6 with the aim to reduce the cost of the series compensator.

On the other hand, the conventional grid connected DFIG system is sensitive to the grid variants such as voltage sags and swells as aforementioned. There will be overcurrent / overvoltage phenomenon in the rotor-side converter during grid fault periods. Herein the essential behavior of DFIG during grid faults will be investigated in the next section by using phasor diagram analysis.

3.4 Essential behavior of DFIG during grid fault

For the convenience of phasor diagram analysis, the T-form circuit of DFIG shown in Figure 3.3 is desired to transform into the Γ-form equivalent circuit. It is worthy to point out that the $\gamma=L_s/L_m$ is nearly equal to 1 for the power rating of generator larger than 100KW [97]. Consequently, the T-form equivalent circuit of DFIG is transformed to the Γ-form equivalent circuit as illustrated in Fig.3.11. The phase diagram analysis will be carried out in the next section based on the Γ-form equivalent circuit.

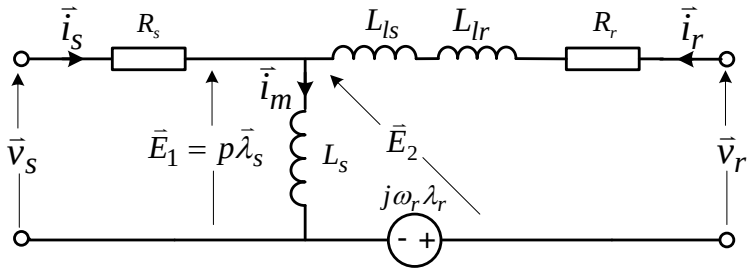

Fig.3.11 Γ-form equivalent circuit of the DFIG in the static frame

3.4.1 Phasor diagram during normal operation

In the DFIG based wind turbine, the stator windings are directly connected to the grid utility via a step-up transformer, and thereby the stator voltage is imposed by the grid. The rotor windings voltage is controlled by a rotor-side converter and is used to perform the machine control. Hence, in the normal operation, the stator voltage phasor $\vec{v}_s$ is a rotating vector of the constant magnitude V_s that rotates at the synchronous speed ω_s

$$\vec{v}_s = V_s e^{j\omega_s t} \tag{3.20}$$

From Fig.3.11, the stator voltage can be expressed as

$$\vec{v}_s = R_s \vec{i}_s + \vec{E}_1 \tag{3.21}$$

Where $\vec{E}_1 = p\vec{\lambda}_s$ and $p=d/dt$. $\vec{i}_s = I_s e^{j(\omega_s t+\varphi_s)}$ is the stator current phasor.

Again, the rotor voltage can be also expressed as

$$\vec{v}_r = \vec{E}_1 + R_r\vec{i}_r + jX_r\vec{i}_r - j\omega_r\vec{\lambda}_r \tag{3.22}$$

Where $X_r=\omega_s(L_{ls}+L_{lr})$. $j\omega_r\vec{\lambda}_r$ is the rotating EMF. Herein we denote $\vec{E}_2 = \vec{E}_1 - j\omega_r\vec{\lambda}_r$ as the rotor-side total EMF, which is shown in Fig.3.11.

For a high power generator, the stator resistance R_s is neglected and thereby the back EMF $\vec{E}_1 = p\vec{\lambda}_s$ is directly equal to the grid voltage. Since the L_m is much larger than L_{ls} and L_{lr}, the $\vec{\lambda}_r$ is nearly equal to $\vec{\lambda}_s$ due to the (3.1). Then the rotating EMF $j\omega_r\vec{\lambda}_r$ in (3.22) can be simplified as

$$j\omega_r\vec{\lambda}_r \approx j\omega_r\vec{\lambda}_s = j\omega_r\int\vec{v}_s dt \tag{3.23}$$

Then substituting $\vec{v}_s$ in (3.20) into (3.23), (3.23) can be rewritten as

$$j\omega_r\vec{\lambda}_r = \frac{\omega_r}{\omega_s}V_s e^{j\omega_s t} = (1-s)\vec{v}_s \tag{3.24}$$

Where $s=(\omega_s-\omega_r)/\omega_s$ is the slip speed.

Due to (3.20)~(3.22), Figure 3.12 presents the phase diagram of the DFIG under normal grid condition. Herein, the stator voltage phasor $\vec{v}_s$ is selected as the reference vector and the wind speed is assumed to be constant at that moment. Consequently, the constant wind power captured by the DFIG is considered. Based on the reference vector, the stator current phasor $\vec{i}_s$ can be determined when the steady-state power factor of DFIG is fixed. The φ_s is the power factor angle, as shown in Fig.3.12. Due to (3.21), the back EMF $\vec{E}_1$ on the stator windings can be figured out. The magnetizing current $\vec{i}_m$ is always lagging 90^0 to the back EMF if the magnetizing resistance is neglected. According to KCL, the rotor current phasor $\vec{i}_r$ can be obtained from the stator current phasor $\vec{i}_s$ and the magnetizing current phasor $\vec{i}_m$. Finally, based on (3.22) and (3.23), the rotor voltage phasor $\vec{v}_r$ can be determined as illustrated in Fig.3.12.

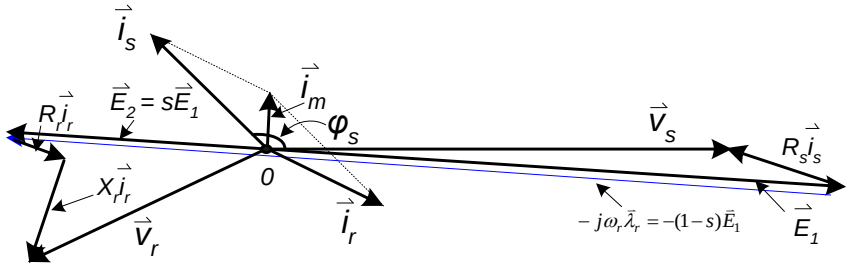

Fig.3.12 Phase diagram of DFIG during normal operation

It can be seen from Fig.3.12 that the magnitude of $\vec{v}_r$ supplied by the rotor-side converter is approximately proportional to the slip speed if the voltage drop on the rotor impedance is neglected. For instance, the amplitude of the rotor voltage is only one fifth the stator voltage if the slip speed is 0.2 pu. For high power generators, the voltage drop on the stator resistor is quite small compared to the voltage on the PCC. Hence, it is acceptable to neglect the resistance in the phasor diagram for simplicity.

3.4.2 Phasor diagram during grid fault condition

This section will analyze the operating behavior of the DFIG during a fault event. Three-phase balance faults are concerned in this section. In practical systems, it is well-known that the voltage drops on the PCC are determined by the grid fault condition and its transmission characteristics. Consequently, when a fault occurred near the PCC, the magnitude of voltage on the PCC is inevitable to drop significantly as well as the change of the phase angle. In order to analyze the operating behavior of DFIG, the PCC voltage during fault period is assumed to be $v_{s,1}$ as illustrated in Fig.3.13. The subscript '1' means the variables during fault periods.

From Fig.3.13, during the fault period, the stator voltage is dropt from the nominal value v_s to $v_{s,1}$ with the phase angle shift φ_1. Herein the stator resistance is neglected for simplicity. Consequently the stator side electromotive force (EMF) E_1 as shown in Fig.3.11 is directly equal to the fault period PCC voltage $v_{s,1}$. At the beginning of the fault, the magnetizing current i_m is impossible to damp so quickly since large mutual inductance itself. So the i_m is considered as the same at that moment. Thereby the rotor flux $\vec{\lambda}_r$ is still

same as the pre-fault value. Hence the rotating EMF $j\omega_r\vec{\lambda}_r$ in the rotor still refers to the pre-fault value as expressed in (3.23). Finally the rotor voltage phasor $\vec{v}_r$ can be figured as shown in Fig.3.13. The rotor back EMF $\vec{E}_2$ during fault periods is much larger than that in the normal operation since the rotating EMF $j\omega_r\vec{\lambda}_r$ is still kept at the pre-fault value.

Normally the rotor voltage is only a small fraction of the stator voltage, such as 0.3 pu. But the $j\omega_r\vec{\lambda}_r$ is much larger than this value. Moreover, the rotor current phasor $\vec{i}_r$ can also be determined by the rotor resistance and inductance as similar as Fig.3.11. Considering the small leakage inductance X_r and rotor resistance R_r, the rotor current will be much larger than the normal value, which is large enough to damage the rotor-side converter. In addition, the stator current phasor $\vec{i}_s$ can be obtained based on the rotor current phasor and the magnetizing current phasor. The aforementioned procedure has been presented in Fig.3.13.

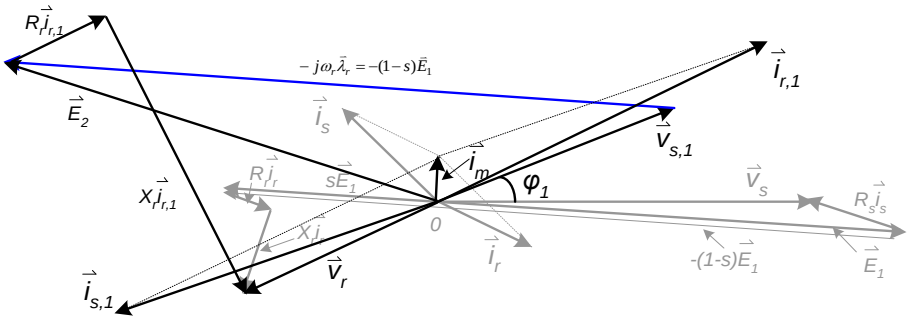

Fig.3.13 Phase diagram of DFIG during grid fault

From Fig.3.13, the rotating EMF $j\omega_r\vec{\lambda}_r$ in the rotor is the main source that makes the DFIG difficult to ride through severe grid faults. As presented in (3.23), the aforementioned rotating EMF is determined by the generator speed and the rotor flux. Thus the rotor flux is decided by the magnetizing current. Due to the large mutual inductance in the large power DFIG, the voltage on the mutual inductor can be immediately changed, however, the current in the inductor does not change instantaneously. This is the essential behavior of the DFIG while the grid fault happens.

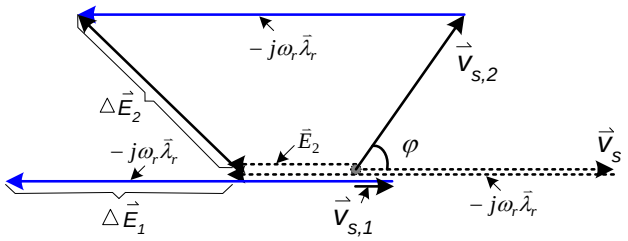

Figure 3.14 Simplified phase diagram of DFIG during a full voltage dip and a partial voltage dip with the phase shift φ

The following part will address which kind of voltage drops that cause the worst operation of the DFIG. Neglecting the resistance of DFIG, the phasor diagram during normal grid condition can be simplified by the dot-lines in Fig.3.14 from Fig.3.13. When the grid suffers a fault, the PCC voltage $\vec{v}_s$ is dropt to $\vec{v}_{s,1}$. The rotor total EMF $\vec{E}_2$ is increased from the normal value $\vec{v}_s - j\omega_r\vec{\lambda}_r$ to $\vec{v}_{s,1} - j\omega_r\vec{\lambda}_r$, which is illustrated in Fig.3.14. If $v_{s,1}$ is equal to zero, the rotor voltage increment ΔE_1 is equal to V_s, the pre-fault rotor voltage. Currently the researchers are considering the $v_{s,1} = 0$, as the worst operation of DFIG.

Both the magnitude and phase angle of the stator voltage can be changed while a fault happens. Normally the phase-angle jump on the PCC is determined by the *X/R* ratios of the source and the fault path [98] while a fault happens near the PCC. As far as is known, the phase-angle jump during fault period has not been paid attention in the investigation of DFIG ride-through. For instance, if the fault stator voltage is illustrated as $v_{s,2}$ in Fig.3.14, where φ is the phase-angle shift. It can be found that the phase-angle jump also contribute to the rotor voltage increment ΔE_2,

$$\left|\Delta E_2\right| = \sqrt{V_s^2 + V_{s2}^2 - 2V_sV_{s2}\cos\varphi} \tag{3.25}$$

From (3.25), when $\varphi \geq \cos^{-1}(V_{s2}/2V_s)$, the ΔE_2 is larger than the ΔE_1, and thereby the phase-angle jump will cause a larger rotor current than that caused by the full voltage dip. Figure 3.15 illustrates the rotor current response considering the magnitude of the stator voltage together with the angle-jump. Although the amplitude of the stator voltage has not been reduced to zero, the phase-angle jump of the stator voltage can also result in the even worse overcurrent in the rotor than that in the condition of the full voltage dip.

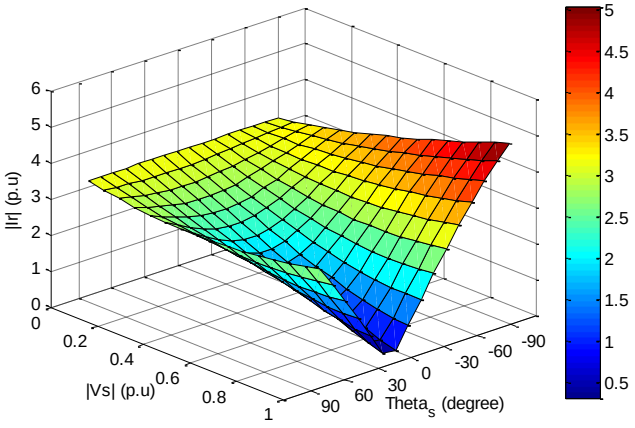

Fig.3.15 The magnitude and angle-jump of stator voltage impact on the rotor current

3.4.3 Key factors on the DFIG fault operation

This section will address the key factors which significantly contribute on the over-current/voltage in the rotor. The factors can be separated in terms of the stator and rotor circuit, respectively.

⑴ The stator resistance/ braking resistance

From Fig.3.11, the E_1 will not be equal to the stator voltage if the voltage drop across the stator resistance is large enough. Therefore, at the fault instant, the E_1 is not reduced so largely to affect the electrical behavior of the rotor circuit. Normally the stator resistance is quite small, especially in high power application. Hence, an additional stator braking resistance can be inserted in the stator circuit during the fault period to enhance the ride-through capability of the generator.

⑵ The rotor resistance / crowbar

From the viewpoint of rotor circuit, the overvoltage is mainly caused by the rotating EMF $j\omega_r\vec{\lambda}_r$. The rotor speed can be considered as a constant at the fault instant. The rotor flux $\vec{\lambda}_r$ is also kept at the same value because of the larger mutual inductance L_m. In order to balance the $j\omega_r\vec{\lambda}_r$, an additional rotor resistance is usually involved. This is the so-call

crowbar method. The additional resistance is used to limit the rotor current in order to avoid the overcurrent in the rotor. However, the additional resistance should not be too large to further increase the terminal voltage of the rotor-side converter.

⑶ Demagnetizing current concept

The rotor flux should be damping immediately in order to avoid the overvoltage in the rotor. Hence, a demagnetizing current can be generated by the rotor-side converter in order to damp the rotor flux as fast as possible, and thereby partly enhance the ride-through capability of the DFIG.

3.4.4 Advantages and disadvantages of DFIG

Section 2.4 has reviewed the characteristics of the main types of wind turbine generators, and the advantages of DFIG based wind turbine can be listed as:

1. Partial power rating electronics converter: The employed power electronics converter is only required to deal with the slip power of DFIG. Hence, the cost of the converter/inverter can be significantly reduced. Typically the converter rating is 20~30% of the total power rating of the system.

2. Variable speed operation: Compared to the fixed speed wind turbines, the variable speed operation makes DFIG wind turbine possible to maximize power point tracking of wind power under different wind profiles, which in turn, improve the utilization of wind turbine.

3. Flexible power factor control: Power factor control can be implemented at lower cost because the DFIG system (four-quadrant converter and induction machine) basically operates similar to a synchronous generator. The rotor converter has to provide only excitation energy/power.

4. Decoupled control of active and reactive power: compared to silicon-controlled rectifier, the DFIG with a four-quadrant converter in the rotor circuit enables decoupled control of active and reactive power of the generator.

Besides the aforesaid advantages of DFIG wind turbine, there are still several limitations of DFIG wind turbine in terms of its poor fault ride-through ability, mechanical commutators and wearable brushes (regular maintenance required), bulky mechanical gearbox for speed coordination, and so on.

To address the poor ride-through ability, a series compensated solution for DFIG ride-through enhancement will be studied in the following sections.

3.5 General control principle of the series compensator

In order to eliminate the transient variants of the stator voltage caused by the step-down PCC voltage during grid faults, the series voltage compensation architecture shown in Fig.3.10 is desired to inject an appropriate $\vec{v}_{sc}$ in the face of an up-stream voltage disturbance. The following section will study how to command the injected voltage $\vec{v}_{sc}$.

During the normal grid voltage, the series compensator is held in an idle state to keep the losses to a minimum. The SW1 (shown in Fig.3.10) is always kept ON to bypass the series compensation system. Once any voltage sag is detected the series compensator switches into active state to operate as fast as possible and inject the required AC voltage to the PCC.

Herein the main considerations for the control of the series compensator are consisted of real-time determination of the start and end of series compensation, voltage reference generation.

3.5.1 Voltage sag detection

The accuracy of the voltage sag detection significantly impact on the operating performance of the series compensator. Due to power quality enhancement for sensitive load application, the voltage sag detection method used is based on the root mean square (rms) value of the error vector, which allows for detection of symmetrical and

asymmetrical sags, as well as the associated phase jump [99]. Hence, the detection formula for starting the series compensation is given by

$$\left|\vec{v}_{error,pcc}\right| > V_{Threshold} \tag{3.26}$$

Here, the rms value of the voltage vector error on the PCC is

$$\left|\vec{v}_{error,pcc}\right| = \left|\vec{v}_{ref,pcc} - \vec{v}_{\sup ply,pcc}\right| \tag{3.27}$$

Where $V_{Threshold}$ is the maximum voltage error allowed on the PCC, where the wind turbine can still ride through by itself. Herein, $\vec{v}_{ref,pcc}$ is the nominal PCC voltage and $\vec{v}_{\sup ply,pcc}$ is the real-time measured PCC voltage. The $\vec{v}_{ref,pcc}$ is equal to the $\vec{v}_{\sup ply,pcc}$ before faults happen.

From (3.26), while the $V_{Threshold}$ is chosen as 0, the series compensator is immediately turned on when any slight sags happen. However, the wind turbine is not exactly like a sensitive power load. It is unnecessary to compensate the stator terminal voltage back to the pre-fault value when PCC voltage suffers slight sag. This is because the rotor-side converter usually has some amount of power margin for overcurrent/overvoltage operation. Hence, we will investigate how to select the appropriate $V_{Threshold}$ in the following paragraphs.

In the conventional DFIG wind turbine, the rotor-side converter usually employs the IGBT as the semiconductor switching device. Its continuous current rating is determined by the steady-state load, while the overload capability could be exploited during transient. In theory, the maximum current switched by the device can be the peak pulse rating, as long as the junction temperature reached in the IGBT is permissible and the V-I switching trajectory is within the safe operating area (SOA). The pulse current rating of an IGBT is typically 100% higher than the continuous current rating. Therefore, the control objective of this study is to constrain the instantaneous rotor current below $I_{r,max}$, which is the maximum allowed rotor current by the device's rating.

Herein, the PCC voltage $v_{pcc,0}$ is changed to $v_{pcc,1}$ after suffering a grid fault and thereby the stator terminal voltage is also changed from $v_{pcc,0}$ to $v_{pcc,1}$. Therefore, the pre-fault

stator and rotor voltage equations of (3.21) and (3.22) are rewritten after ignoring the stator resistance as

$$\vec{v}_{pcc,0} = \vec{E}_{1,0} \tag{3.28}$$

And

$$\vec{v}_{r,0} = \vec{E}_{1,0} + R_r\vec{i}_{r,0} + jX_r\vec{i}_{r,0} - j\omega_r\vec{\lambda}_r \tag{3.29}$$

The stator and rotor voltages during the fault period can be expressed as

$$\vec{v}_{pcc,1} = \vec{E}_{1,1} \tag{3.30}$$

And

$$\vec{v}_{r,1} = \vec{E}_{1,1} + R_r\vec{i}_{r,1} + jX_r\vec{i}_{r,1} - j\omega_r\vec{\lambda}_r \tag{3.31}$$

Where, the subscript 0 and 1 in (3.28) ~ (3.31) depict the pre-fault and fault values, respectively. The rotating EMF $j\omega_r\vec{\lambda}_r$ of rotor circuit can be considered as constant during fault occurrence as shown in (3.23).

Substituting $j\omega_r\vec{\lambda}_r$ from (3.23) into (3.29) and (6.31), then

$$\vec{v}_{r,0} = (R_r + jX_r)\vec{i}_{r,0} + s\cdot\vec{v}_{pcc,0} \tag{3.32}$$

$$\vec{v}_{r,1} = \vec{v}_{pcc,1} + (R_r + jX_r)\vec{i}_{r,1} - (1-s)\vec{v}_{pcc,0} \tag{3.33}$$

Considering the rotor voltage generated by the converter as same during fault period, then the pre-fault and fault rotor currents can be derived as,

$$\vec{v}_{pcc,0} - \vec{v}_{pcc,1} = (R_r + jX_r)(\vec{i}_{r,1} - \vec{i}_{r,0}) \tag{3.34}$$

Compared to the X_r, the R_r can be neglected, and the (3.34) can be simplified as

$$\vec{v}_{pcc,0} - \vec{v}_{pcc,1} = jX_r(\vec{i}_{r,1} - \vec{i}_{r,0}) \tag{3.35}$$

Herein the voltage and current phasors in the pre-fault and fault condition are

$$\begin{aligned} \mathrm{Pr}\,e-\ fault:\ & \vec{v}_{pcc,0} = 1\angle 0^0, \quad \vec{i}_{r,0} = I_{r0}\angle\theta_0 \\ Fault:\ & \vec{v}_{pcc,1} = V_{pcc1}\angle\theta_v, \quad \vec{i}_{r,1} = I_{r,\max}\angle\theta_c \end{aligned} \tag{3.36}$$

Where, $\vec{v}_{pcc,0} = 1\angle 0^0$ is set as the reference phasor, θ_0 can be arbitrary value from 0 to 2π. $\theta_v \in [0, 2\pi]$ is the phase angle of the fault PCC voltage. θ_c is also arbitrary value from 0 to 2π.

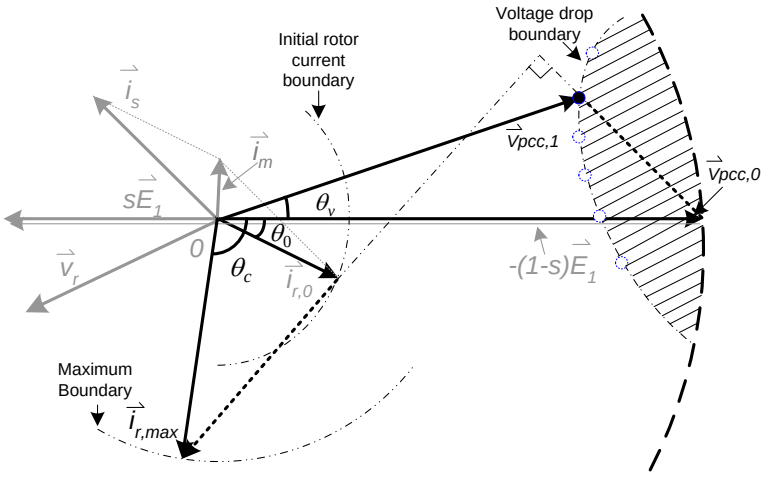

Fig.3.16 Determination of the maximum allowed voltage drop on the PCC under the maximum rotor current $I_{r,max}$

Substituting (3.36) into (3.35), the boundary of the maximum allowed voltage drop on the PCC can be constructed with the maximum rotor current $I_{r,max}$. Figure 3.16 illustrates the phasor diagram of PCC voltage and rotor current under this situation. From Fig.3.16, if the rotor current reached the boundary of the limitation, $I_{r,max}$, the stator voltage is then changed from $v_{pcc,0}$ to $v_{pcc,1}$ due to (3.35). Herein the $v_{pcc,1}$ is the maximum allowed voltage drop on the PCC. With the different θ_c, we can plot the boundary of the maximum allowed voltage drop on the PCC as shown in Fig.3.16. Hence, if the fault PCC voltage is at the right-side of the aforementioned boundary (the shadow area), the rotor current will never exceed the maximum current limitation $I_{r,max}$.

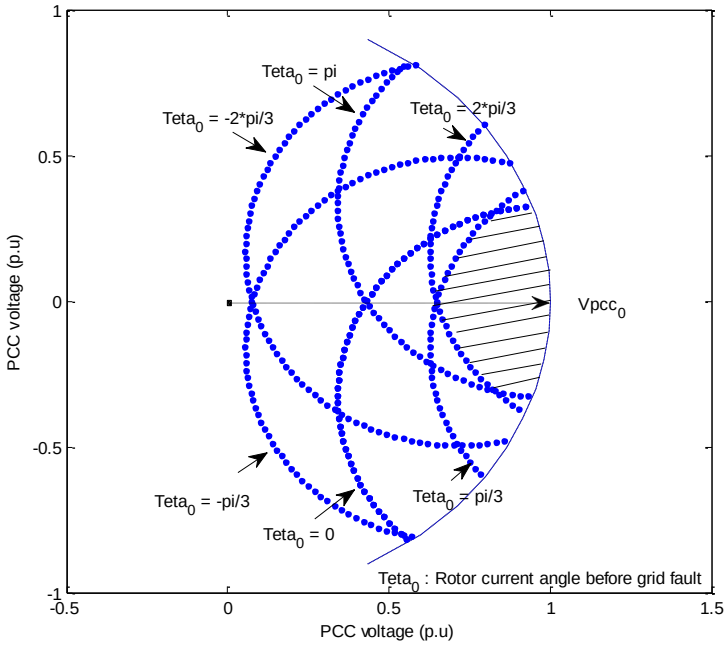

Fig.3.17 The maximum allowed PCC voltage drop boundaries along with different pre-fault rotor current angle θ_0

On the other hand, since the different pre-fault rotor current angle θ_0 also results in the different PCC voltage boundaries, a group of the voltage boundaries can be plotted. Figure 3.17 shows the boundaries of the maximum allowed voltage drop on the PCC under the different θ_0. In practice, it is difficult to predict the θ_0 when the grid fault happen. Hence, in order to make sure the rotor current is within the limitation for all of the θ_0, the common-area of the aforesaid PCC boundaries is determined, as shown in Fig.3.17 by the shadowed area.

Due to the above principle, if the PCC voltage is within the shadowed area, it is unnecessary to trigger the series compensator since the conventional DFIG can withstand this kind of grid faults. Once the PCC voltage exceeded the shadowed area, the series compensator is required to operate immediately; otherwise, the rotor converter will be overloaded. This provides a criterion to determine the aforementioned $V_{Threshold}$.

3.5.2 Reference voltage generation for series compensator

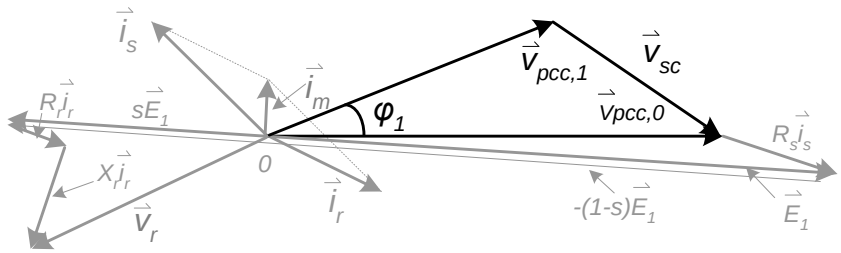

Fig.3.18 Phase diagram of series voltage compensation under grid faults

Once the (3.26) is satisfied, the series compensator is kicked into function. In ideal operation, the series compensator is desired to fully balance the voltage deviation on the PCC in order to maintain the voltage on the stator as the pre-fault value. Figure 3.18 presents the phasor diagram of this operation. The other variables in the phasor diagram can still stay at the same place as the pre-sag occasion. The pre-fault voltage on the PCC is $v_{pcc,0}$, and the fault voltage is $v_{pcc,1}$. The reference of the series compensator is the voltage difference between $v_{pcc,0}$ and $v_{pcc,1}$ if we assume the ideal series transformer with 1:1 ratio.

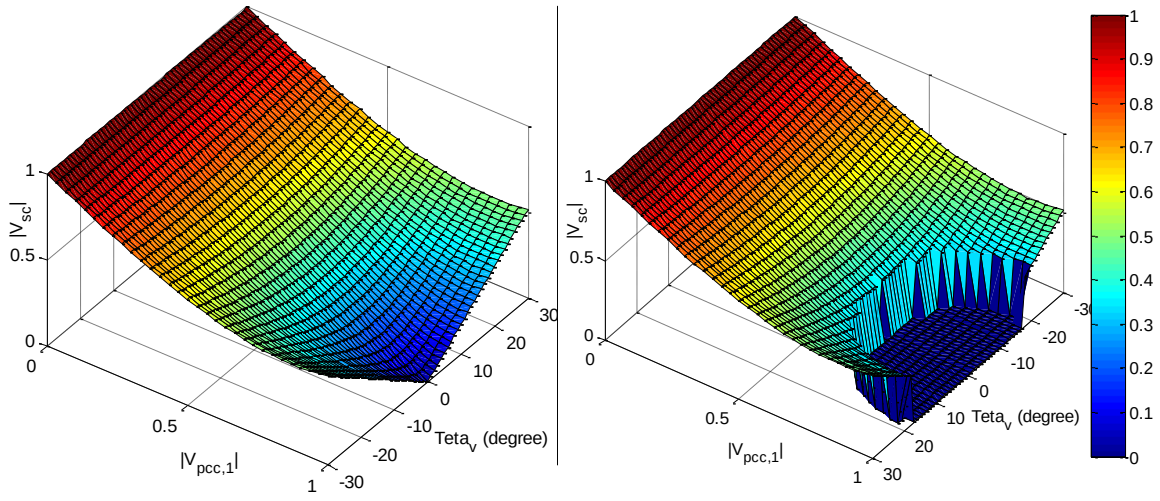

(a) $I_{r,max}$=1 pu (b) $I_{r,max}$=2 pu

Fig.3.19 The series voltage V_{sc} related to fault PCC voltages V_{pcc} under different rotor current limitation

Consequently, the voltage rating of the series compensator under different rotor current limitations $I_{r,max}$ can be plotted, as illustrated in Fig.3.19. It can be seen that the large PCC voltage drop is required to inject a high voltage from the series compensator. However, the series compensator is unnecessary to switch in and out frequently with the larger rotor current limitation as shown in Fig.3.19(b). In practice, the slight sag will have a relatively larger possibility to occur than the more severe sags. The appropriate selection for turning on and off the series compensation is important for the overall system performance.

3.5.3 Advantages and Disadvantages of DFIG-Series compensator

The main purpose of series compensator is to help DFIG ride-through grid faults and thereby enhance the ride-through ability of DFIG based wind turbine. A summary of the characteristics of the series compensated DFIG is listed as below:

1. The series compensator is desired to compensate the voltage sag or swell of grid utility and thereby maintain the DFIG stator terminal voltage as normal under such fault conditions, which in turn, avoid the overcurrent phenomenon in the rotor circuit of DFIG. The significant advantage of the series compensated DFIG is able to protect the rotor-side partial power rating converter, which is easy to be damaged in the conventional DFIG system during severe grid faults.

2. In theory, the series compensated DFIG is potential to deal with any kinds of grid faults, such as symmetrical and unsymmetrical faults. Herein, the symmetrical fault condition will be studied in the thesis.

Besides the aforementioned advantages, the cost of the series compensator is the main challenge of the series compensated DFIG system. Normally, the series compensator is required to deal with active power as well as reactive power delivery, which is determined by the stator current phasor and sag voltage phasor on the PCC. The large active power current requires the series compensator has a large energy storage capacity, which in turn, results in the bulky volume of energy storage devices as well as high cost of the series compensator. To overcome the aforesaid constraint, an improved control scheme for the series compensator will be analyzed in the next section.

3.6 Improved ride-through control of DFIG-Series compensator

Based on the aforementioned analysis in section 3.5, the ideal solution for the DFIG based wind turbine during a voltage dip would be a system that isolates the wind turbine from the voltage dip. The series compensator can provide this kind of function. However, the main drawback of the series compensator application is its high cost, compared to the crowbar protection. Moreover, the longer the voltage dip is, the larger the compensator energy storage capacity is required. Therefore, it will even increase the cost of the whole system. All of these inspire to seek solutions to reduce the capacity of the series compensator. In this section, a potential solution is introduced to reduce the energy capacity of the series compensator.

The previous section contributes to analyze the voltage rating of the series compensator. The energy capacity of the series compensator will be analyzed in this section. The DFIG rotor current response related to the stator voltage is introduced in [100] as,

$$i_{dr} = \frac{1}{L_m} \frac{\omega_s}{s^2 + 2(R_s / L_s)s + \omega_s^2} v_s - \frac{L_s}{L_m} i_{ds} \tag{3.37}$$

$$i_{qr} = \frac{1}{L_m} \frac{s + R_s / L_s}{s^2 + 2(R_s / L_s)s + \omega_s^2} v_s - \frac{L_s}{L_m} i_{qs} \tag{3.38}$$

Where i_{dr} and i_{qr} are the rotor-side d- and q-axis components in the synchronous frame, respectively.

According to (3.37) and (3.38), the transfer function between the rotor current and the stator voltage can be considered as a second-order model. While the generator suffered a grid fault, it seems the system occur a step-function input. Under the step-function of stator voltage, there is a significant oscillation on the rotor current response since the system damping coefficient, $\xi = R_s/(\omega_s L_s)$ is nearly zero. With inverse Laplace transform and $R_s << \omega_s L_s$, the time-domain rotor current response under grid fault can be described as,

$$i_{dr}(t) = \frac{V_s}{\omega_s L_m} - \frac{kV_s}{\omega_s L_m}\left[1-\cos(\omega_s(t-t_0))\right] \tag{3.39}$$

$$i_{qr}(t) = -\frac{kV_s}{\omega_s L_m}\sin[\omega_s(t-t_0)] \tag{3.40}$$

Where, k is the voltage drop severity. The detailed derivation of (3.39) and (3.40) are presented in Appendix A.

The system response caused by linear ramp-function is usually smaller than that caused by step-function. This inspires to change the stator voltage from the step-function to ramp-function by injecting a ramp voltage from the series compensator. Hence, the improved control scheme for the series compensator can be arranged as follow.

It is assumed that the DFIG is operating at the normal grid voltage $\vec{v}_{pre-fault,pcc}$ until a fault happen at time t_0, and the PCC voltage $\vec{v}_{fault,pcc}$ during fault is returned to the normal value $\vec{v}_{post-fault,pcc}$ at time t_1 after fault is removed. The $\vec{v}_{post-fault,pcc}$ may be not same as the $\vec{v}_{pre-fault,pcc}$ since the network topology can be changed after fault clearance.

Consequently, as fast as the detection of the voltage drop on the PCC is beyond the limit in (3.26), we apply a voltage vector of the series compensator as,

$$\vec{v}_{sc} = \begin{cases} 0 & t \notin [t_0, t_0+\Delta T] \\ (\vec{v}_{pre-fault,pcc} - \vec{v}_{fault-pcc})\cdot\left[1-(t-t_0)/\Delta T\right] & t \in [t_0, t_0+\Delta T] \end{cases} \tag{3.41}$$

And

$$\vec{v}_{sc} = \begin{cases} 0 & t \notin [t_1, t_1+\Delta T] \\ (\vec{v}_{fault-pcc} - \vec{v}_{post-fault,pcc})\cdot\left[1-(t-t_1)/\Delta T\right] & t \in [t_1, t_1+\Delta T] \end{cases} \tag{3.42}$$

Where, ΔT is the operating duration of the series compensator after detecting a grid fault. By compensating the voltage as expressed in (3.41) and (3.42), the stator voltage can be smoothed without any step-changes in terms of the amplitude and angle while the PCC voltage suffers a step change by the severe fault. In other words, the ramp-function voltage generated by the series compensator makes the stator voltage of DFIG as a ramp-

function. The following paragraphs will explain how to select the ΔT.

When the voltage in (3.41) and (3.42) is injected, the DFIG stator terminal voltage is a ramp-function during grid fault. Thereby the rotor current response is calculated based on the inverse Laplace transformation,

$$i_{dr}(t) = \frac{V_s}{\omega_s L_m} - \frac{kV_s}{\omega_s L_m}\left[\frac{t-t_0}{\Delta T} - \frac{1}{\omega_s \Delta T}\sin(\omega_s(t-t_0))\right] \tag{3.43}$$

$$i_{qr}(t) = -\frac{kV_s}{\omega_s L_m}\frac{1}{\omega_s \Delta T}\left[1-\cos(\omega_s(t-t_0))\right] \tag{3.44}$$

The detailed derivation of (3.43) and (3.44) has been presented in Appendix A as well. In order to make (3.43) and (3.44) smaller than (3.39) and (3.40) respectively, the constraint are $\Delta T > 1/\omega_s$ and $\Delta T > 2/\omega_s$. Hence, the ΔT is better to choose as

$$\Delta T > \frac{2}{\omega_s} \tag{3.45}$$

From (3.45), the ΔT is chosen as several cycles of the system frequency, which aims to limit the rotor current oscillation during fault periods. The larger ΔT is, the smaller the rotor current oscillation will be. However, the large ΔT will result in large energy capacity of the series compensator, since the DC-link capacity of the series compensator can be calculated by

$$E = \frac{1}{2}C\Delta V^2 = \int_{t_0}^{t_0+\Delta T} \vec{v}_{sc} \cdot \vec{i}_s \, dt \tag{3.46}$$

Where ΔV is the maximum allowable voltage variation of the DC-link capacitor of the series compensator. C is the related capacitance. From (3.46), while the $\vec{v}_{sc} \cdot \vec{i}_s$ is positive, the series compensator will absorb power to charge the DC-link capacitor. Otherwise, the capacitor will be discharged to provide the network real power. On the other hand, the size of the capacitor can be reduced by shorting the ΔT while the $\vec{v}_{sc} \cdot \vec{i}_s$ is fixed. However, the determination of the ΔT has been presented in (3.45).

Due to the series compensation concept, the original controller of the rotor-side converter

can still work without any damage during the fault period. The reactive power generated by the stator windings and the grid-side converter is still under control, which is helpful to recover the PCC voltage. This is unavailable with the crowbar solution. Hence the proposed architecture can provide a better characteristic to satisfy with the latest grid requirements.

3.7 Simulation results for DFIG

A detailed computer simulation of the DFIG based wind generation system is carried out in Matlab/Simulink as well as the ride-through demonstration of the proposed series compensator concept. Table 3.1 presents a list of numerical values of DFIG parameters, which is used in the simulation. The system operating waveforms from the simulations are presented in this section.

Table 3.1 DFIG parameters

Items	**Value**
Rated power	*1.5 MW*
Rated frequency	*50 Hz*
Stator voltage	*575 V*
Stator resistance	*0.007 p.u*
Rotor resistance	*0.005 p.u*
Mutual inductance	*2.9 p.u*
Stator leakage inductance	*0.17 p.u*
Rotor leakage inductance	*0.16 p.u*
Number of pole pairs	*3*

3.7.1 Simulation results for DFIG during normal operation

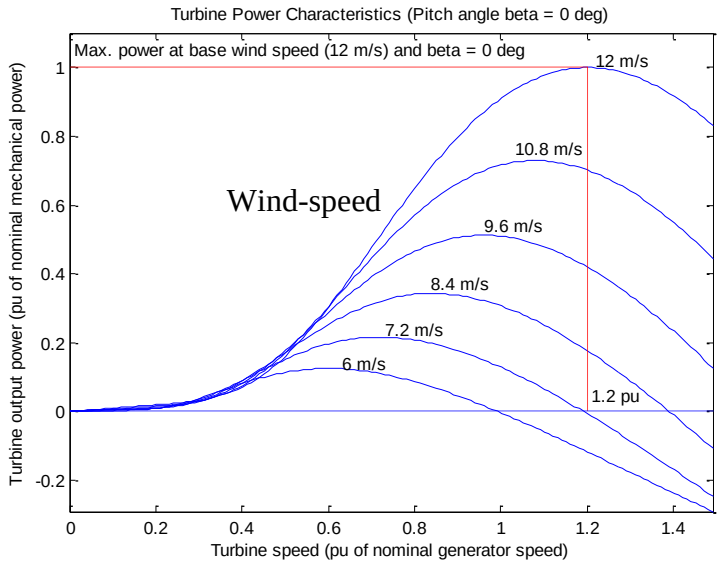

Fig.3.20 Wind turbine power characteristics used in the simulation

Figure 3.20 shows the wind turbine power characteristic along with different turbine rotating speeds. Herein, the rated wind speed for this turbine is 12 m/s. When the wind speed is 12m/s, the desired rotor speed should be 1.2 pu in order to track the maximum power point of wind energy. Along with the decrease of wind speed, the desired rotor speed is generally reduced as shown in Fig.3.20. The pitch angle is set as zero when the wind speed is below the rated speed. However, once the wind speed is larger than 12 m/s, the pitch angle control is turned in function in order to limit the maximum power flowing into the generator. While the wind speed is larger than a cut-out speed, the power delivered by the turbine is regulated as zero. This is the principle of pitch control. Consequently, due to the power characteristics, the DFIG operating performance under different wind speeds is carried out, which will be given in the following paragraphs.

Figure 3.21 shows the operating waveforms of the DFIG based turbine under different wind speeds. The wind speed has a step-up at time 2 s from 8m/s to 12m/s, and then a step-down from 12m/s to 8m/s at time 4 s. Figure 3.21 (a) shows the aforementioned wind speed profile. The generator speed is accordance with the wind speed in order to maximize wind power extraction. Figure 3.21(b) illustrates the generator speeds. Consequently, the corresponding power captured by the DFIG is also given in Fig.3.21 (c). From Fig.3.21 (c), the reactive power output is always zero since the zero reference is

set. During the simulation, the DC-link voltage of the back-to-back converter is controlled as 1200 V, which is presented in Fig.3.21 (d). The rotor side current of the generator is shown in Fig.3.21 (e). The frequency of the rotor current is changed along with the rotor speed from the sub-synchronous speed to super-synchronous speed and finally back to the sub-synchronous speed. The magnitude of the current is generally increased with the rotor speed since the delivered power is increased.

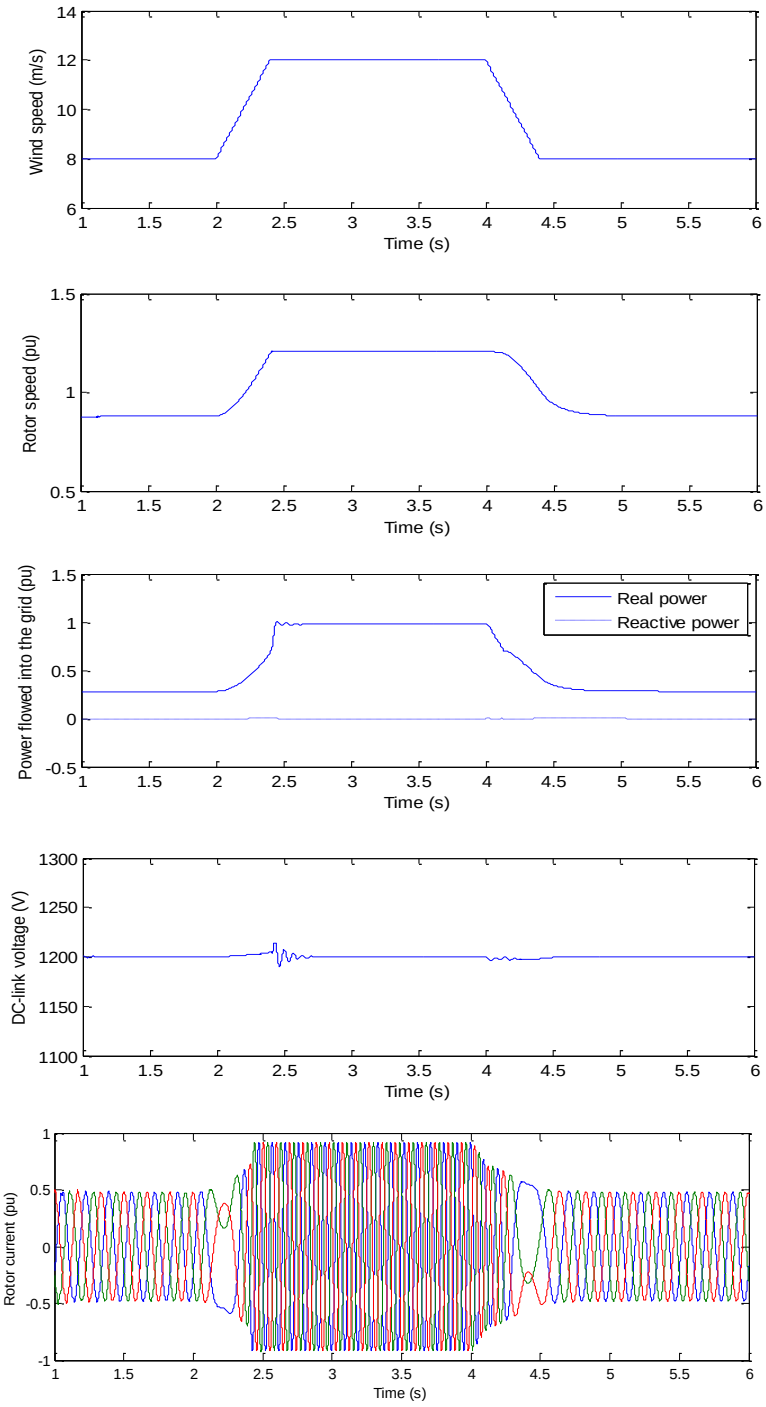

Fig.3.21 DFIG operating performance under different wind speeds

Figure 3.22 shows the steady-state waveforms of the stator/rotor voltage and current at the 12m/s wind speed. Both the stator windings and rotor winding are delivered wind power into the utility grid. The 80% of wind power is delivered by the stator winding. And the slip power 0.2 pu is delivered by the rotor side converter and completely transferred to the grid-side converter if the loss on the DC-link is neglected. Figure 3.22 (a) and (b) present the rotor voltage and current respectively. And the stator three-phase voltage and current are shown in Fig.3.22 (c) and (d), respectively.

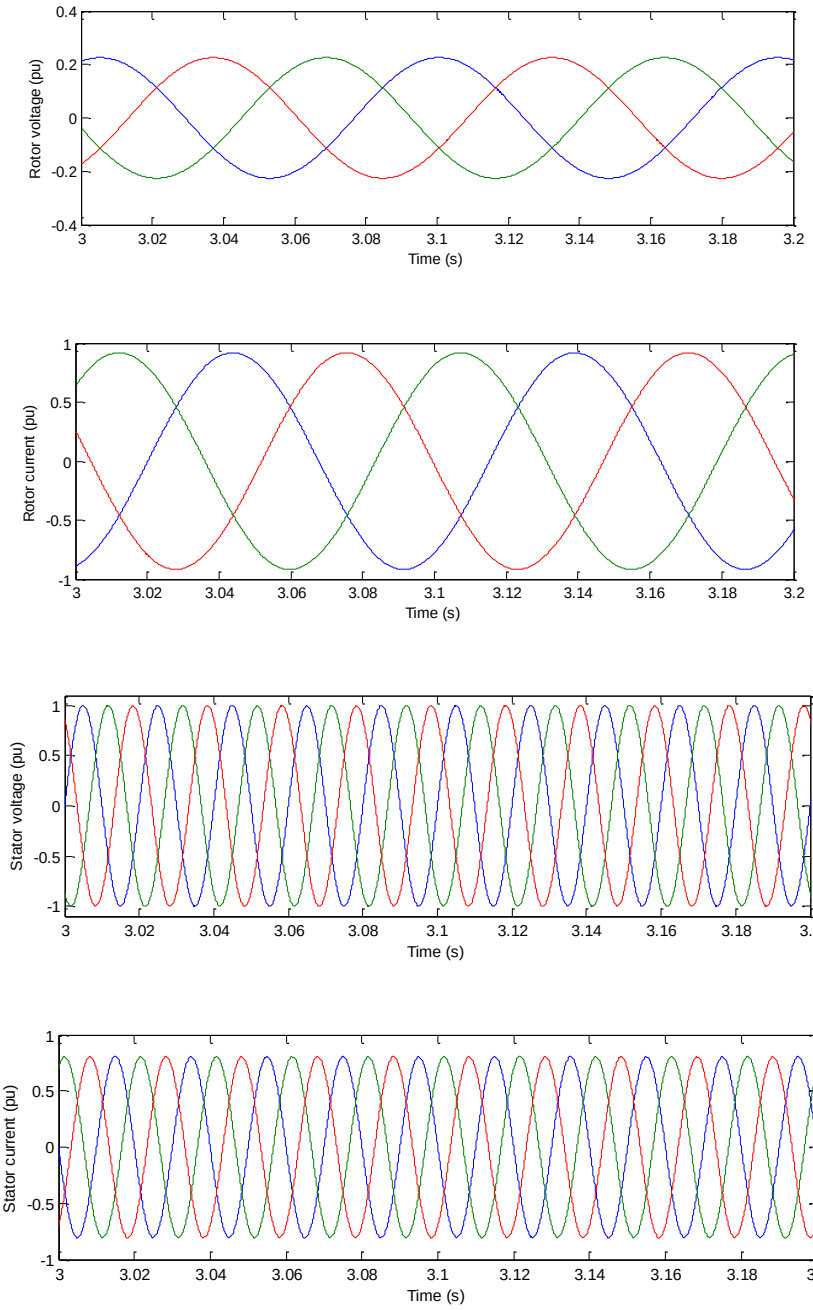

Fig.3.22 The steady-state stator and rotor voltage/current waveforms

3.7.2 Simulation results for DFIG during faults

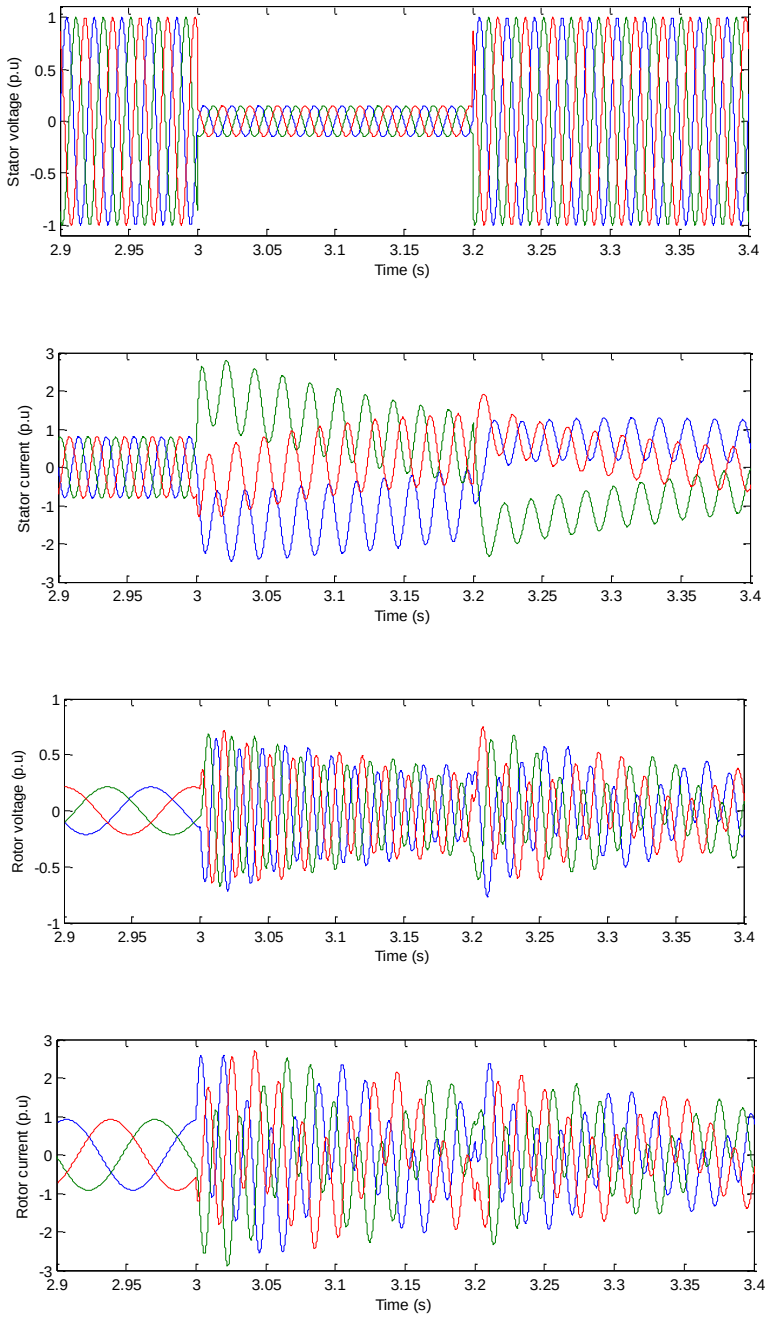

Fig.3.23 Stator/rotor voltages and currents in the conventional DFIG system

Figure 3.23 shows the stator and rotor-side three-phase voltage/ current in the conventional DFIG system when suffering a balanced grid fault. The rotor speed is set at 1.2 pu so as to maximize wind power capture according to the corresponding wind speed.

At time 3 to 3.2 s, the DFIG suffers a grid fault, which results in 85% voltage drop and no phase shift on the stator-side PCC. From Fig.3.23, the transient maximum currents of the stator and rotor windings appeared at the moment of voltage changes. At that time, the rotor current suffers a severe overcurrent, which is up to 3 times larger than the nominal value. It can be seen from Fig.3.23(c) that the rotor voltage is larger than the rated value, which is normally 0.3 pu. Hence, the rotor-side converter will be damaged if the stator voltage suffers this severe fault, however, the operator demands the DFIG should have the ability to ride through this kind of grid faults.

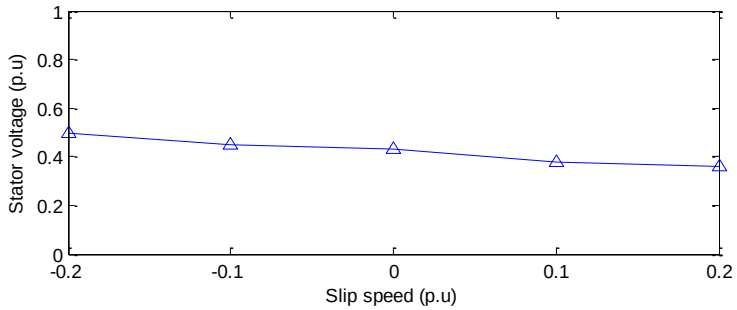

Fig.3.24 Feasible ride-through region of the conventional DFIG system under three-phase balanced fault

As mentioned in Section 3.6, the rotor-side converter is able to afford the transient current up to 2 pu since the semiconductor device characteristics. Herein, we assume the maximum rotor current limit is set as 2 p.u , applied in the following simulation.

Figure 3.24 shows the maximum allowed voltage drop on the PCC under three-phase balanced fault, where the rotor current is not beyond the limitation. The phase shift of the PCC voltage is set as zero. From Fig.3.24, the stator voltage of the original DFIG system is allowed to drop to as low as 0.5 p.u, and the rotor current does not exceed the limitation of 2 p.u. In addition, the larger generator speed is, the lower voltage drop is allowed. For instance, if the slip speed is -0.2, the maximum voltage drop is 0.5 p.u (1-0.5=0.5p.u), in order to make the rotor-side current within the limitation. Once the voltage drop is larger than this value, the rotor current will exceed the 2 p.u limitation immediately.

It can be found from Fig.3.24 that the serious condition of ride-through is occurred at the maximum slip speed. This is accordant to the analysis in Section 3.5. So this condition of the maximum slip speed is chosen to analyze the ride-through performance affected by

the post-fault voltage phase shift. Figure 3.25 shows the fault ride-through impact of the voltage phase shift during three-phase balanced faults. Along with the increase of the phase shift between the pre-fault and post-fault voltages, the maximum allowed voltage drop on the stator windings are reduced rapidly in the conventional DFIG system. From Fig.3.25, not only the amplitude of the voltage dip affects the ride-through performance, but also the phase shift of the stator voltage also results in the ride-through problem of the DFIG. The proposed series compensation solution is desired to balance both of the amplitude and angle of the PCC voltage.

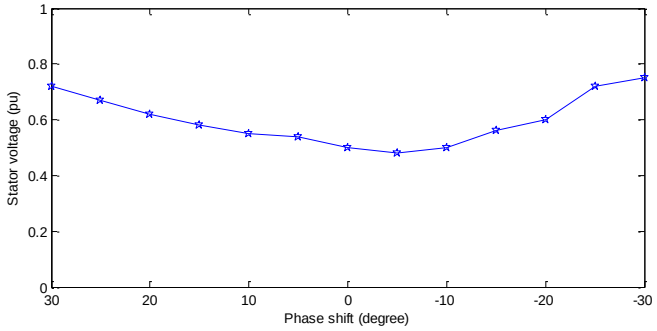

Fig.3.25 Fault voltage phase shift impacts on the ride-through performance in the original DFIG system

3.7.3 Performance of DFIG

The simulation results of DFIG during normal and fault condition have been studied in Section 3.7.1 and 3.7.2 respectively. Based on the aforementioned results, this section will discuss the performances of DFIG, which can be classified into two main types: wind power delivery characteristics (e.g., MPPT) and grid compatibility (e.g., fault ride-through ability).

With the characteristic of mechanical power captured by turbine (as illustrated in Fig. 3. 20), the DFIG is required to deal with the variable wind profile. To maximize the utilization of wind turbine, the MPPT feature of DFIG is one of the important factors to evaluate the performance of the wind generation system. Figure 3.21 is desired to evaluate the MPPT performance of the DFIG based wind turbine. Under the given variable wind speed, the rotor speed of the DFIG can be controlled at the optimized

reference speed, and thereby make DFIG tracking the maximum power point of wind power.

On the other hand, it is better to extinguish the operating performance of DFIG during fault conditions before the enhancement is involved. The essential behaviors of DFIG under grid fault condition have been shown in Fig.3.23. It can be seen that the current in the rotor would be nearly 3 time of that in the normal operation when suffering the assumed fault mentioned in Section 3.7.2. Hence, the rotor-side converter will be damaged under the assumed fault if no any protection is provided. The simulation of the serried compensated DFIG will be carried out in the next section, and the simulation results in Fig.3.23 can be used as the comparison criterion for the developed series compensated DFIG.

3.8 Simulation results for series compensated DFIG

3.8.1 Simulation results for series compensated DFIG during normal operation

During normal grid condition, the series compensator is bypassed by SW1 as illustrated in Fig. 3.10, and thereby the series compensator is at the "standby" status. Hence, the operation of the series compensated DFIG is similar to the original DFIG system as discussed in Section 3.7.1 during normal operation.

3.8.2 Simulation results for series compensated DFIG during faults

To verify the effectiveness of the ride-through enhancement of the series compensator, the proposed control scheme of the series compensator is implemented in the simulation. Figure 3.26 shows the operating performance of the DFIG with the proposed series compensation method. Herein, the compensation duration ΔT are chosen as 20ms according to the (3.45). When the PCC voltage is down to 0.15 p.u and no phase shift is involved. The PCC voltage is dropt at time 3s and recovered at time 3.2s, which is shown in Fig.3.26(a). Figure 3.26(b) shows the compensation voltage generated by the series compensator according to the proposed control scheme. Due to the compensation, the

stator voltage of DFIG is smoothed as Fig.3.26(c). The compensation solution not only smoothes the amplitude, but also smooth the angle shift of the PCC voltage. Figure 3.27 shows the zoom in of the stator voltage with the compensation. There is no step change in terms of the amplitude and angle shift, which are the main causes of the overcurrent in the rotor windings.

From Fig.3.26 (d) and (e), the currents of the stator and rotor windings are always within the limitation. Both the stator and rotor currents are much smaller than that in Fig.3.23. Hence, the proposed method is effective to ride through the severe grid faults without any crowbar circuits.

From the viewpoint of the series compensator, Figure 3.26(f) presents the DC-link voltage of the series compensator. At the start point of the voltage dip, the power is absorbed by the compensator and thereby stored into the DC capacitor, which in turn, boost the DC voltage. Thus at the end point of the voltage dip, the compensator supplies the power and make the DC link voltage drop. However, within the one cycle of the voltage dip, the DC link voltage of the series compensator is back to the pre-fault value. There is no power change between the compensator and the wind turbine. The power captured by the turbine is stored in the mechanical rotating energy of the wind turbine rotor. Therefore, the rotor speed is increased as shown in Fig.3.26 (g).

In Fig.3.26, the compensation duration ΔT is chosen as 20 ms, but the ΔT will impact on the size of the DC-link capacitance of the series compensator and the peak value of the rotor current. Figure 3.28 shows the relationship of the rotor peak current/ DC link capacitance of the series compensator versus the compensation duration ΔT. The voltage on the PCC in Fig.3.26(a) is supplied in this simulation. With the increase of the ΔT, the peak value of the rotor current can be reduced, however, the capacitance of the compensator will be larger. Herein, the maximum allowed voltage variation is chosen as 600V and the pre-fault voltage is 1000V. The capacitance is calculated based on (3.46).

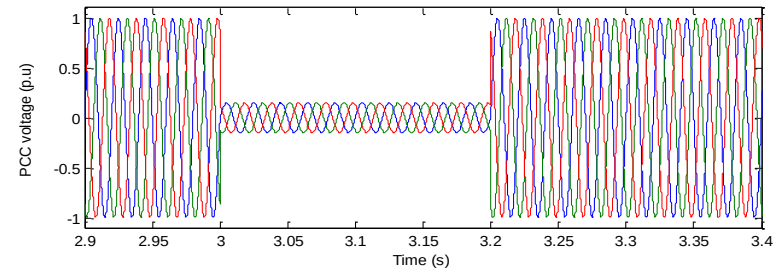
PCC voltage (p.u)
Time (s)

(a)

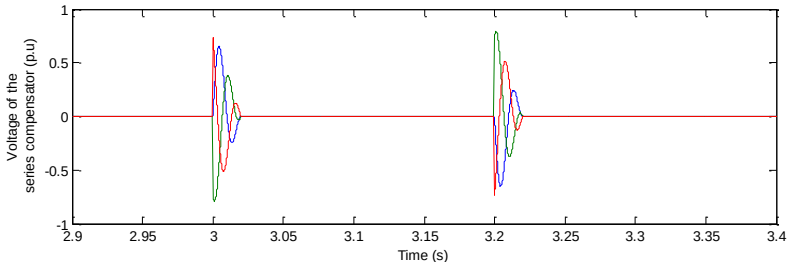
Voltage of the series compensator (p.u)
Time (s)

(b)

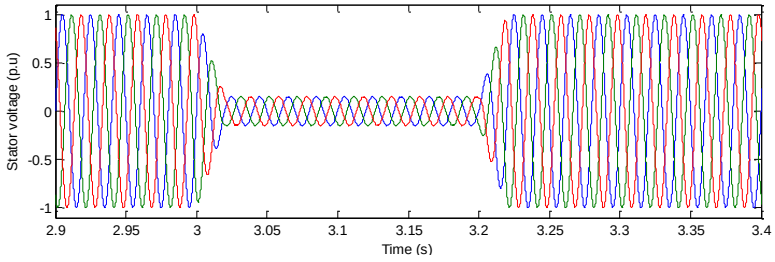
Stator voltage (p.u)
Time (s)

(c)

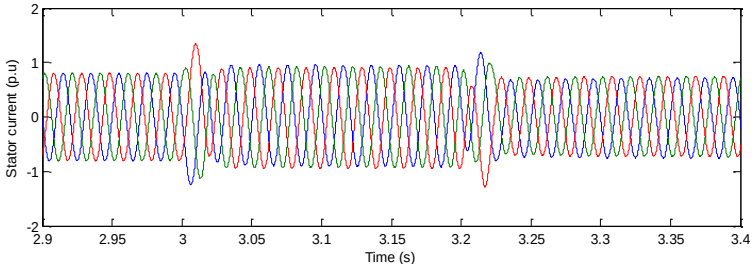
Stator current (p.u)
Time (s)

(d)

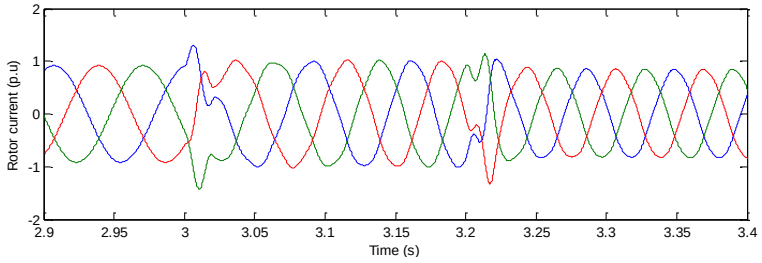
Rotor current (p.u)
Time (s)

(e)

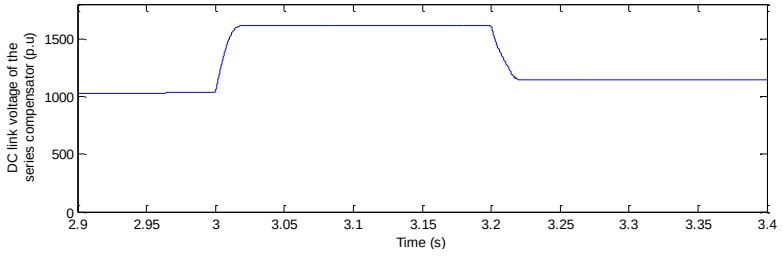
DC link voltage of the series compensator (p.u)
Time (s)

(f)

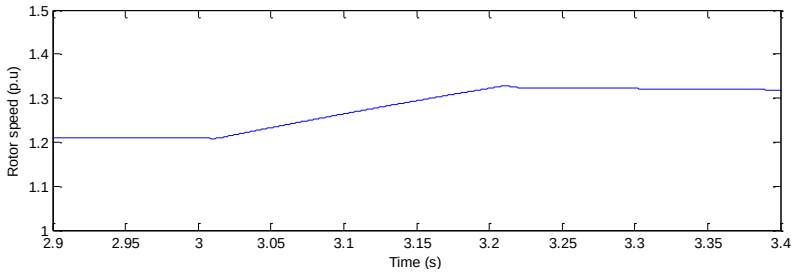

(g)

Fig.3.26 Ride-through performance of the DFIG system with the series compensation method

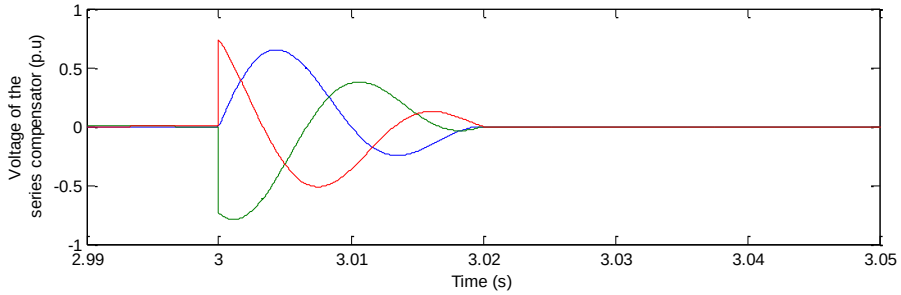

(a)

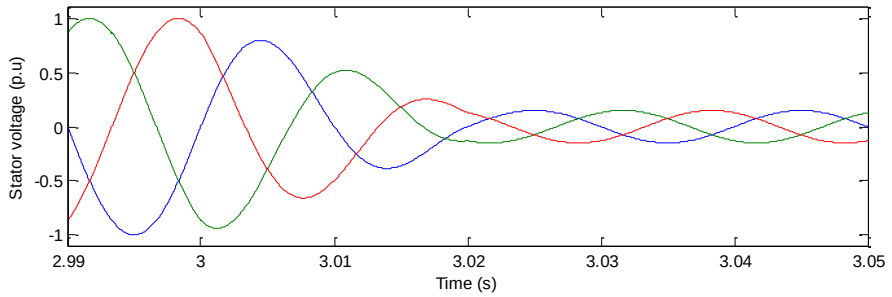

(b)

Fig.3.27 Zoom-in of the voltage compensation during transient fault

Due to the series compensation, the original control of the DFIG controller can be operating as the pre-fault condition during the fault period. The PCC voltage fault can not affect the operating states of the rotor-side and grid-side converter. This makes the grid-side converter generates reactive current independently. Figure 3.29 shows the reactive current of the grid-side converter during the fault period. It is utilized to recover the PCC voltage according to the latest grid code requirement.

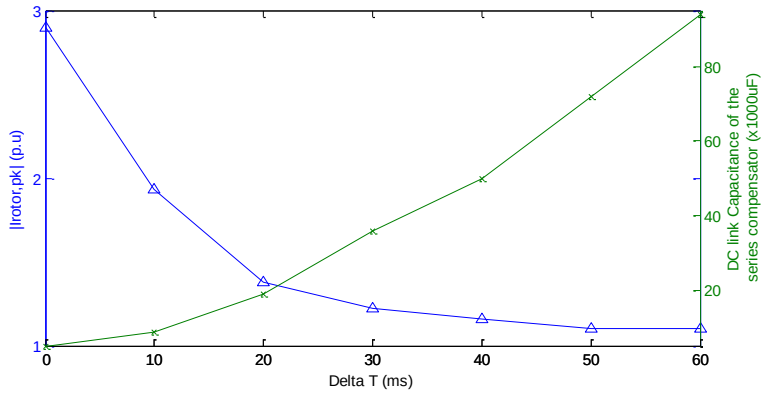

Fig.3.28 The relationship of the rotor peak current/ DC link capacitance of the series compensator versus the compensation time ΔT

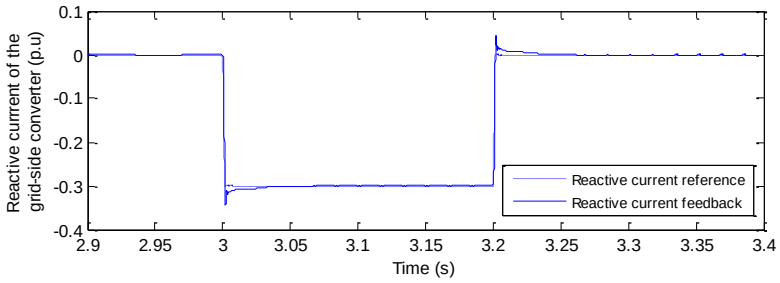

Fig.3.29 The control of the reactive current of the grid-side converter during the fault period

3.8.3 Performance of series compensated DFIG

The rotor-side current is an important indicator to evaluate the effectiveness of the series compensated solution under the given grid fault. From Fig.3.26, the fault currents in the rotor of the series compensated DFIG is controlled around the normal value, which is much smaller than that of the original DFIG in Fig.3.23. In other words, the rotor-side converter can be protected by the series compensator during the grid fault, and the ride-through ability of DFIG wind turbine can be enhanced with the concept of series compensation.

In addition, the energy storage capacity of series compensator would affect the system cost of the series compensated solution. The large energy storage will significantly increase the cost of series compensator, which in turns, increase the whole system

expense. The improved control of series compensator has been proposed in Section 3.6 to reduce the energy storage of series compensator and thereby reduce the system cost. In our proposed method, the series compensator is desired to provide the expected voltage only during the transient periods of grid fault happening and clearing. The effectiveness of the control strategy has been verified in Section 3.8.2 as well.

3.9 Conclusion

Enhancing ride-through capability under grid fault events has been recognized as a challenging problem of DFIG based wind generation systems. This chapter has presented the field oriented control and the grid voltage oriented control of DFIG for an in-depth understanding of the operation of DFIG. Then a ride-through solution, which was inspired by the series compensation device, has been proposed to enhance grid robustness of DFIG. The compensator is in series with the stator windings of DFIG and the general control of the series compensator aims to fully eliminate the impact of grid fault voltages. However, it is inevitable to increase the cost of the ride-through enhancement. Subsequently, an improved ride-through control scheme of the DFIG and series compensation has been developed to significantly reduce the energy capacity of the series compensator, which in turn, reduces the system expense. This is the significant contribution of this ride-through strategy. The developed series compensated DFIG has a stronger grid fault ride-through ability than that of the original DFIG. The performance of the designed architecture has been verified in simulation.

CHAPTER 4

MODULATION AND ANALYSIS OF THREE-SWITCH BUCK-TYPE RECTIFIER BASED Z-SOURCE INVERTER

4.1 Introduction

Compared with DFIG, PMSG exhibits good ride-through and grid support performance because of its full scale converter. Hence the power electronics converter plays a significant role in the PMSG turbine in terms of reliability and power quality.

This chapter presents an integration of a three-switch buck-type rectifier and a Z-Source inverter for PMSG, which can overcome the drawbacks of existing configurations as mentioned in Section 2.6.2. It is prerequisite to explore the integrated topology named as the three-switch buck-type rectifier with Z-Source inverter in terms of modulation, circuit analysis and validation before doing system-level integration for PMSG based wind turbine. Hence, the modulation, analysis and demonstration of the three-switch buck-type rectifier based Z-Source inverter will be introduced in this chapter with aims to clarify the essential behavior of the developed topology. Then the design methodology, the simulation studies and experimental validation of the proposed architecture for PMSG wind application will be presented in the next chapter.

4.2 Derivation of the proposed topology for PMSG turbine

In order to explore the suitable modulation strategy for the integration of Z-Source inverter and three-switch rectifier, this section will introduce the origin of the developed integrated topology, which can be deduced from the Z-Source inverter and indirect matrix converter (IMC).

4.2.1 Principle of Z-Source inverter

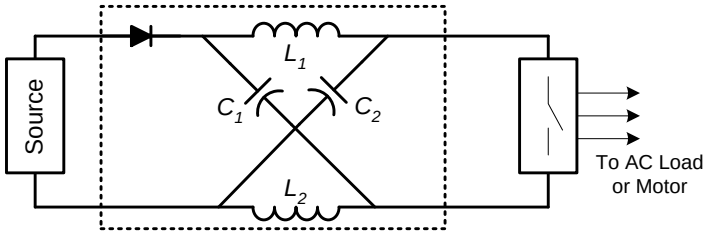

Fig.4.1 DC Z-Source network diagram

The DC Z-source network diagram is illustrated in Fig.4.1 [101]. An impedance network is coupled between a power source and an inverter circuit, with the impedance network being implemented using a split-inductor (L_1 and L_2) and capacitor (C_1 and C_2) connected in an X-shape. This unique impedance network allows the Z-Source inverter to buck and boost its output voltage, and also provides unique features that cannot be achieved in the conventional voltage source inverter (VSI). The inductors L_1, L_2, and capacitors C_1 and C_2 make up a symmetrical Z-Source network. Assuming that the inductors L_1 and L_2 and the capacitors C_1 and C_2 have the same inductance L and C, respectively, the Z-Source network becomes symmetrical. The detailed operation modes of the Z-Source inverter will be discussed in Section 4.4.

4.2.2 Principle of indirect matrix converter

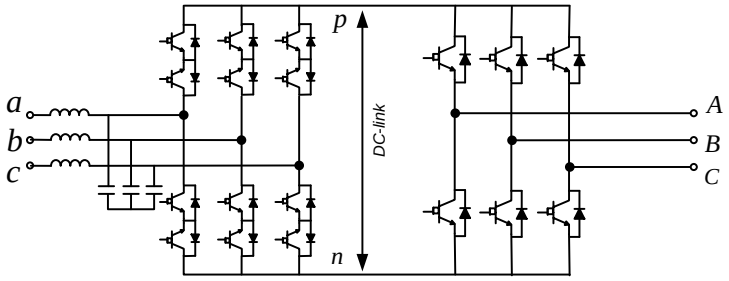

Fig.4.2 Topology of a three-phase indirect matrix converter

The topology of the IMC is shown in Fig.4.2 [102]. It realizes AC to AC direct power conversion without intermediate DC-link capacitor. The bidirectional switches in the front-end rectifier are used to block the input voltage source, and the two-quadrant

switches are applied in the back-end inverter. Space vector modulation (SVM) is simultaneously employed in both the front-end rectifier and the back-end inverter. The detailed modulation will be introduced in Section 4.3.

4.2.3 Derivation of the three-switch buck-type rectifier based Z-Source inverter

The Z-Source network shown in Fig.4.1 can be introduced into the IMC (Fig.4.2) such that the integrated topology can exhibits both the advantages of the aforementioned two topologies. Figure 4.3 shows the integration of Z-Source network and IMC. The proposed topology is able to boost the average DC-link voltage in order to provide higher load voltage when required. In Fig.4.3, the switches in the rectification stage are implemented using four-quadrant switches [103], and the switches in the inversion stage are each implemented with an IGBT and an anti-parallel diode. In this topology, the diode *D* in the DC-link is utilized for safe commutation of four-quadrant switches in the front-end converter.

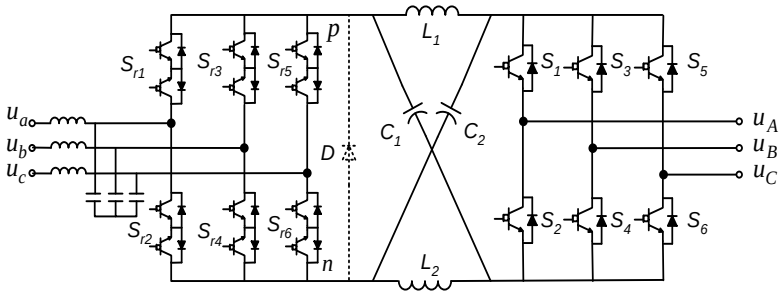

Fig.4.3 Integration of IMC and Z-Source network

Nevertheless, it is noted that the commutation diode *D* in Fig.4.3 can be replaced by the front-end bridge leg. Moreover, the DC-link voltage of the topology in Fig.4.3 must have a fixed polarity, but the front-end four-quadrant switch of the front-end rectifier is able to operate with both positive and negative DC-link voltage polarities. All of these inspire to simplify the integration of the IMC and Z-Source network by reducing the front-end circuit complexity. Consequently, the simplification principle is illustrated in Fig.4.4. One bridge-leg of the front-end circuit is shown in Fig.4.4(a), and if only positive DC-link voltage and current are required, the actual useful semiconductors are presented in

Fig.4.4(b) with solid-line. The other two switches S_{pa1} and S_{na1}, shown with dot-line, are used to flow negative DC-link current. To simplify the topology, the function of S_{pa2} and S_{na2} are replaced by the structure in Fig.4.4(c), where the control signals of switch S_{pa2} and S_{na2} are same. Considering the same function of S_{pa2} and S_{na2}, the final compact bridge leg is shown in Fig.4.4(d), where the switching signal of the merged switch is synthesized by an 'OR' operator of S_{pa2} and S_{na2}.

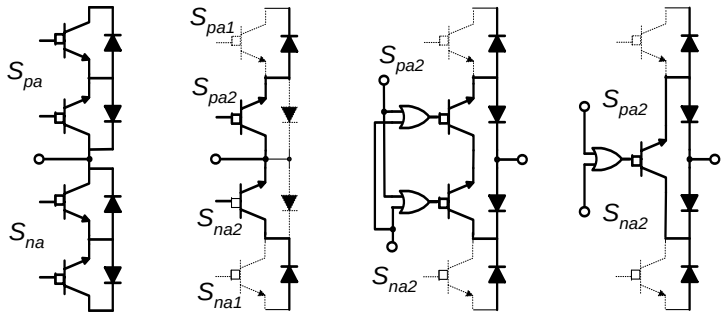

(a) (b) (c) (d)

Fig.4.4 Simplification of one-leg in the front-end converter

(a) front-end bridge leg structure (b) for modulating Positive DC-link voltage (c) simplified circuit of (b) (d) derived compact bridge leg

Consequently, the two simplified AC-AC Z-Source inverter topologies are presented in Fig.4.5. The commutation problem in the two derivatives can be solved easily since the absence of four-quadrant switches. The actual control of S_{ra}, S_{rb} and S_{rc} (Fig.4.5) is synthesized by utilizing the principle depicted in Fig.4.4. Due to the so-call sparse matrix converter [104], the topology shown in Fig.4.5(a) is named as Z-Source sparse converter, which has the same functionality as the topology shown in Fig.4.3. Bidirectional power flow can be implemented in these two topologies.

However for applications where only unidirectional power flow is required, e.g. wind turbine generation, the three-switch buck-type Z-Source inverter presented in Fig.4.5(b), is a good alternative since it has the simplest architecture with buck-boost capability and low current distortion. Moreover, it has the highest reliability since there is no shoot-through risk in both front-end and back-end circuits. The shoot-through The system

integration of this topology for PMSG based wind turbine will be discussed in the next chapter.

The front-end converter is used to control the input power factor and serve as the power source of the back-end Z-Source inverter. As explained in Fig.4.4, the switching signal of the switch S_{ra}, S_{rb} and S_{rc} in Fig.4.5 can be synthesized by an 'OR' operator of S_{r1} and S_{r2}, S_{r3} and S_{r4}, S_{r5} and S_{r6}, respectively. In order to control input power factor flexibly, space vector modulation is adapted to generate the control signals for S_{ri} ($i=1, 2, \ldots, 6$), which will be discussed in detail in the next section. On the other hand, the modulation of back-end Z-Source inverter should be coordinated with the front-end rectifier, especially the control of shoot-through mode. Hence, Section 4.3.3 will explain the synthesized modulation of the front-end converter and back-end inverter.

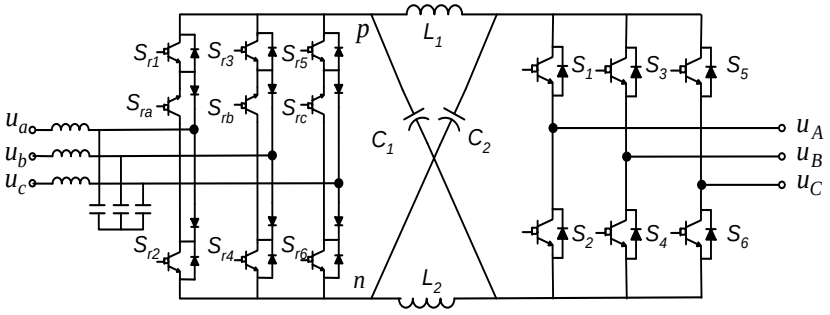

(a) Topology of Z-Source sparse converter

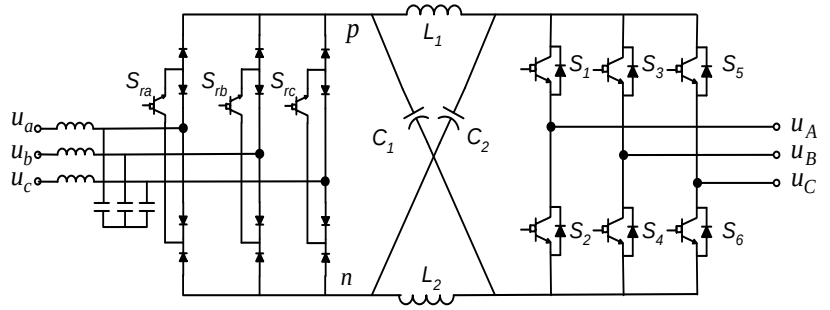

(b) Topology of three-switch buck-type Z-Source inverter

Fig.4.5 Two derivatives of the proposed IMC based Z-Source inverter

4.3 Operation and Modulation of three-switch rectifier based Z-Source inverter

This section will introduce the modulation scheme for the three-switch buck-type rectifier based Z-Source inverter. Since the derivation of this converter is based on the IMC. Hence the SVM modulation for the IMC can be used for the control of the derivative converter. Herein, the modulation of IMC will be presented.

4.3.1 Space vector modulation

Implementation of SVM for the matrix converter has been discussed in [105], where the similar strategy can be used for IMC. The input current of the front-end rectifier is modulated by current-SVM to attain controllable input power factor. Voltage-SVM is applied in the back-end inverter to modulate three-phase output voltage. The synthesis of the simultaneous output-voltage and input-current SVMs for controlling the IMC are performed. The control principle of the IMC is introduced via front-end rectifier and back-end inverter, respectively.

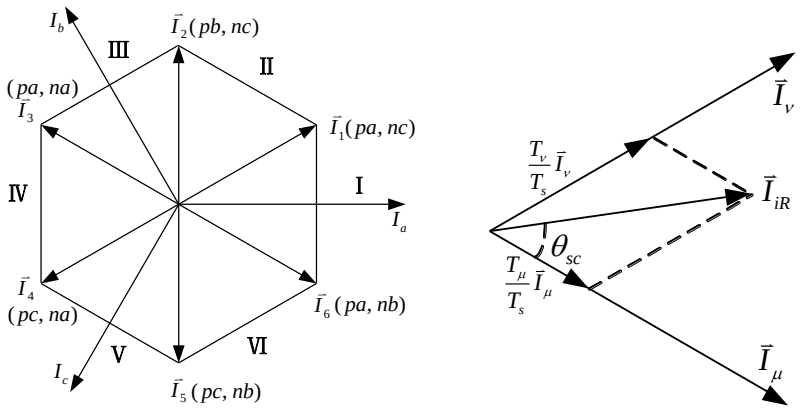

Fig.4.6 Input current space vector modulation of the front-end rectifier

The six switches of the rectifier stage can be divided into nine switch modes as shown in Fig.4.6. These nine modes are relevant to nine static space current vectors which include six non-zero-vectors and three zero-vectors. The three-phase instantaneous input current can be transformed into rotating current space vectors by Park transformation. The rotating vector can be modulated by the six non-zero-vectors and three zero-vectors. For

example, when the vector is in a particular segment, it can be synthesized by two static vectors of this interval. So the input current vector can be expressed as:

$$\vec{I}_{iR} = d_{\mu} \cdot \vec{I}_{\mu} + d_{\nu} \cdot \vec{I}_{\nu} + d_{0i} \cdot \vec{I}_{0} \tag{4.1}$$

Where, $d_{\mu} = T_{\mu}/T_s = m_i \cdot \sin(60 - \theta_{sc})$, $d_{\nu} = T_{\nu}/T_s = m_i \cdot \sin\theta_{sc}$, $d_{0i} = T_{0i}/T_s = 1 - d_{\mu} - d_{\nu}$, θ_{sc} is the input current vector angle, m_i is the modulation index of the front-end rectifier, T_s is the switching period, T_{μ}、T_{ν}、T_{0i} are the turn-on time of different current vectors in one switching period, d_{μ}、d_{ν}、d_{0i} are the corresponding duty-cycles, respectively.

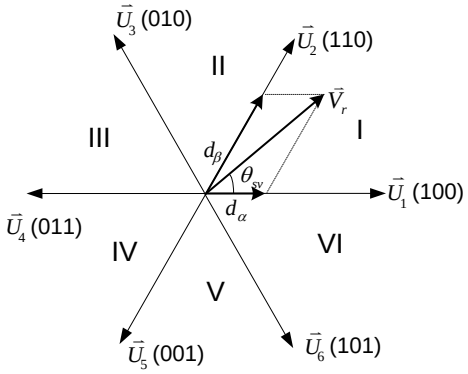

Fig.4.7 Space vector representation of the back-end inverter

The back-end inverter is a conventional voltage source inverter (VSI). Among all the switches combinations, there are six non-zero-vectors and two zero-vectors shown in Fig.4.7. The rotating output-voltage vector can be modulated by the six non-zero-vectors and two zero-vectors. Hence, the resulting output voltage vector can be described as:

$$\vec{V} = d_{\alpha}\vec{V}_{\alpha} + d_{\beta}\vec{V}_{\beta} + d_{ov}\vec{V}_{0} \tag{4.2}$$

Where, $d_{\alpha} = T_{\alpha}/T_s = m_v \sin(60 - \theta_{sv})$, $d_{\beta} = T_{\beta}/T_s = m_v \sin(\theta_{sv})$, and $d_{ov} = 1 - d_{\alpha} - d_{\beta}$. θ_{sv} is the output-voltage vector angle, m_v is the modulation index of the VSI.

4.3.2 Control of indirect matrix converter

To obtain a correct balance of the input currents and output voltages in the same switching periods, the modulation pattern should produce all combinations of the rectification ($\mu-\nu-0$) and inversion ($\alpha-\beta-0$) switching states, resulting in the following switching pattern: $\mu\alpha-\mu\beta-\nu\beta-\nu\alpha-0$. Each sequence duty-cycle is a cross-product of the rectification and inversion duty-cycles, while zero-vector duration completes the switching sequence:

$$\begin{aligned} d_{\mu\alpha} &= d_\mu \cdot d_\alpha = m \cdot \sin(60-\theta_{sc}) \cdot \sin(60-\theta_{sv}) \\ d_{\mu\beta} &= d_\mu \cdot d_\beta = m \cdot \sin(60-\theta_{sc}) \cdot \sin(\theta_{sv}) \\ d_{\nu\beta} &= d_\nu \cdot d_\beta = m \cdot \sin(\theta_{sc}) \cdot \sin(\theta_{sv}) \\ d_{\nu\alpha} &= d_\nu \cdot d_\alpha = m \cdot \sin(\theta_{sc}) \cdot \sin(60-\theta_{sv}) \end{aligned} \tag{4.3}$$

Where, $m = m_i \cdot m_v$ is defined as the modulation index of IMC. For simplification, it is convenient to choose $m_i = 1$ and $m = m_v$.

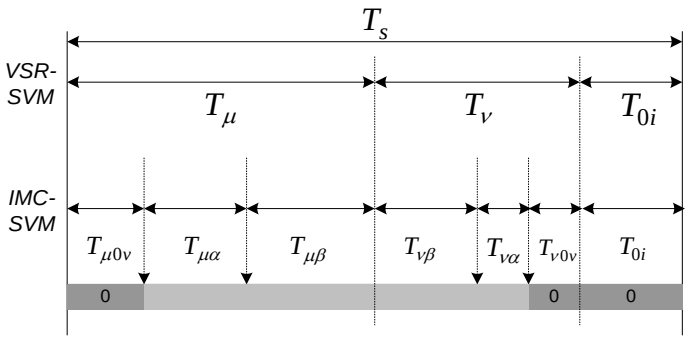

Fig.4.8 Switching modes synthesis of the IMC

During the remaining part of the switching cycle (1- $d_{\mu\alpha}$ - $d_{\mu\beta}$ - $d_{\nu\beta}$ - $d_{\nu\alpha}$), we can utilize the zero-vector, either from the rectification stage (three zero-vectors) or inversion stage (two zero-vectors). Hence, there are totally five zero-vectors available in the IMC. Note that only three zero-vectors are available in the conventional MC. This is the most notable difference in modulation between the IMC and conventional MC. To make the averaged DC-link stage voltage of the IMC constant, the switching sequence shown in Fig.4.8 is utilized. The corresponding duty-cycles can be calculated by:

$$\begin{aligned} d_{\mu 0v} &= d_{\mu} \cdot d_{0v} = m \cdot \sin(60 - \theta_{sc}) \cdot [1 - \cos(30 - \theta_{sv})] \\ d_{v0v} &= d_{v} \cdot d_{0v} = m \cdot \sin(\theta_{sc}) \cdot [1 - \cos(30 - \theta_{sv})] \\ d_{0i} &= m \cdot [1 - \cos(30 - \theta_{sc})] \end{aligned} \tag{4.4}$$

Where, $d_{\mu 0v}$, d_{v0v} are the duty-cycles while the zero voltage-vector of the inversion stage and the nonzero current-vector of the rectification stage are performed simultaneously. d_{0i} is shown in (4.1).

To evaluate the DC-link voltage of the IMC, we take the input current-vector in the interval *I* [105] as an example. Based on the duty-cycles in (4.3) and (4.4), the DC-link voltage can be expressed as:

$$\begin{aligned} V_{pn} &= V_{ab} \cdot (d_{\mu\alpha} + d_{\mu\beta} + d_{\mu 0v}) + V_{ac} \cdot (d_{v\alpha} + d_{v\beta} + d_{v0v}) \\ &= V_{ab} \cdot d_{\mu} + V_{ac} \cdot d_{v} \end{aligned} \tag{4.5}$$

Together with (4.3) and (4.4), (4.5) can be rewritten as:

$$V_{pn} = d_{\mu} v_{ab} + d_{v} v_{ac} = \begin{bmatrix} d_{\mu} + d_{v} \\ -d_{\mu} \\ -d_{v} \end{bmatrix}^{T} \begin{bmatrix} v_a \\ v_b \\ v_c \end{bmatrix} = \frac{3}{2} V_{im} \cos\varphi_i \tag{4.6}$$

Where, v_a, v_b, v_c are three-phase input voltages, V_{im} is the amplitude of the input phase-voltage and φ_i is input power factor angle. Assuming that the input power factor is unity, maximum DC-link voltage can be obtained. Similarly, the voltage waveform in the other five segments can be deduced.

4.3.3 Modulation of the developed converter

With the principle of simplification in Fig.4.4, the control principle is easily expanded to the developed Z-Source inverters. Figure 4.9 shows the switching sequence of the proposed Z-Source inverters within a switching period T_s. During the duration of $m \cdot T_s$, the SVM approach is applied to modulate the converter. Then the shoot-through state of the converter is arranged in the zero-vector interval ($(1-m) \cdot T_s$). The detailed switching modes will be analyzed in Section 4.4. The subsections in d_{0i} is also required similar in d_u

and d_v in order to obtain a good performance of input current. The related duty-cycles can be expressed as,

$$\begin{aligned} d_{0i\alpha} &= d_{0i} \cdot d_{\alpha} = m \cdot [1-\cos(30-\theta_{sc})] \cdot \sin(60-\theta_{sv}) \\ d_{0i\beta} &= d_{0i} \cdot d_{\beta} = m \cdot [1-\cos(30-\theta_{sc})] \cdot \sin(\theta_{sv}) \\ d_{0i0v} &= m \cdot [1-\cos(30-\theta_{sc})] \cdot [1-\cos(30-\theta_{sv})] \end{aligned} \tag{4.7}$$

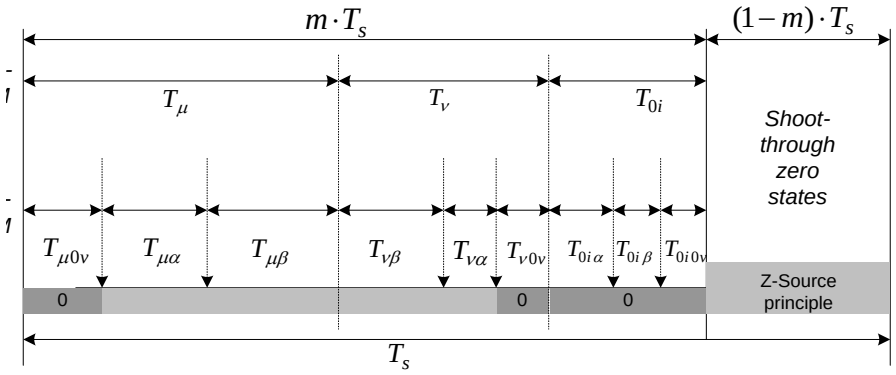

Fig.4.9 Switching sequence for the developed Z-Source topology

On the other hand, turning-on the switches in the front-end circuit of the three-switch buck-type Z-Source inverter will make it as the diode front-end Z-Source inverter of [106]. Doing this makes it impossible to modulate good line-side current. However, this provides a robust operation characteristic of the three-switch buck-type Z-Source converter since shoot-through is allowed.

4.4 Circuit analysis of the developed Z-Source inverter

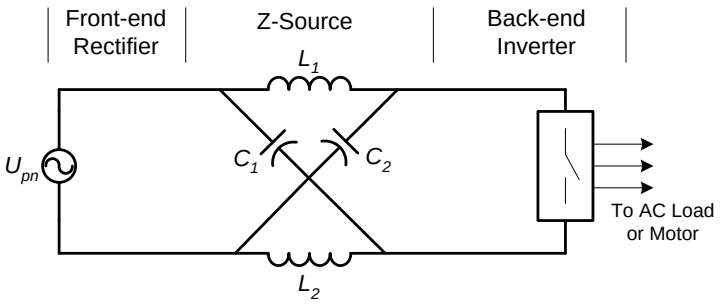

Fig.4.10 Reduced circuit of the developed Z-Source inverter

As viewed from the Z-Source network, the front-end rectifier can be modeled as an averaged DC Voltage source with high frequency harmonics. So the DC-link voltage can be expressed as (4.6). We take the current-vector in the interval *I* as an example to further explain the operating principle and operating modes. When the input current-vector is located at the Interval *I*, the switches S_{r1} and S_{r4} conduct as a pair ($\vec{I}_{\mu}$) and thereby the Z-Source input voltage is fed by V_{ab}. Then the switches S_{r1} and S_{r6} conduct as a pair ($\vec{I}_{v}$) and thereby the DC-link voltage is V_{ac}. Finally the switches S_{r1} and S_{r2} conduct as a pair (Zero-vector) and the DC-link voltage would be zero (short-circuit). As a result, the proposed Z-Source inverters are reduced to the basic Z-Source inverter, as shown in Fig.4.10.

4.4.1 Equivalent circuit analysis

From the reduced circuit, there are three operation modes in terms of the back-end inverter bridge's different switching states.

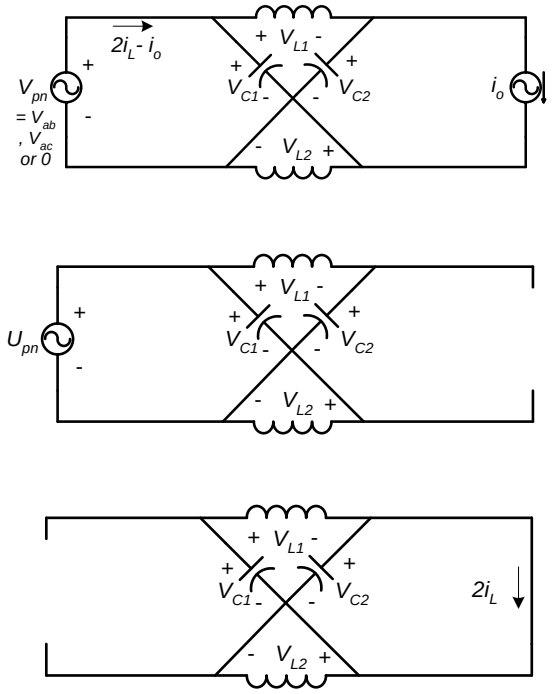

(a) Mode *I*

(b) *Mode II*

(c) *Mode III*

Fig.4.11 Equivalent circuit modes of the developed Z-Source inverter

Mode I

The inversion stage is operating in one of the six traditional non-zero-vectors, thus acting as a current source (i_0) viewed from the Z-Source circuit. The DC-voltage of the Z-Source network can be V_{ab}, V_{ac} or 0 which is depended on the input current-vector applied. Figure 4.11(a) shows the circuit of this mode. In the conventional AC-DC-AC converter, the front-end rectifier may not conduct depending on the DC capacitor voltage level. However, the Z-Source network always forces the front-end rectifier to support the difference between the inductor current (I_L) and inverter DC current i_0, namely $2I_L - i_0$. Both inductors have an identical current value because of the circuit symmetry.

Mode II

The back-end inversion bridge is operating in one of two zero voltage-vectors and shooting through either the upper and lower three switches, thus acting as an open circuit viewed from the Z-Source network. Figure 4.11(b) shows the circuit of this mode. The voltage drop on the inductor would not be a constant which is dependent on the actual value of the V_{pn}. This is the difference between the Z-Source network applied in the IMC and the conventional inverter. The current in the inductor will therefore be following in nonlinear form.

Mode III

The back-end inversion stage is operating in one of the seven shoot-through states. During this mode, all the bidirectional switches in the front-end rectifier are off, separating the DC-link from the AC line. In the three-switch buck-type Z-Source inverter, the AC line is automatically separated by the front-end diode. Figure 4.11(c) shows the circuit of this mode. Depending on how much a voltage boost is needed, the duration of the shoot-through state is determined.

Due to the switching principle presented in Fig.4.9, the corresponding switching modes of the Z-Source inverters are presented in Fig.4.12.

① When $t \in [t_0, t_1]$, the Z-Source inverter is operating at *Mode II*. One of two non-zero input current-vectors is applied. The inductor voltage $V_{L1} = -(V_C - V_{ab})$, and thereby the inductor current is dropping. The output voltage of the Z-Source network is $V_0 = 2V_C - V_{ab}$.

② When $t \in [t_1, t_2]$, the Z-Source inverter is operating at *Mode I*. One of two non-zero input current-vectors is applied. The inductor voltage is $V_{L1} = -(V_C - V_{ab})$, and the output voltage of the Z-Source network is $V_0 = 2V_C - V_{ab}$.

③ When $t \in [t_2, t_3]$, the Z-Source inverter is operating at *Mode I*. Another of the two non-zero input current-vectors is applied. The inductor voltage is $V_{L1} = -(V_C - V_{ac})$, and thereby the falling rate of the inductor current is changed. Thus the output voltage of the Z-Source network is $V_0 = 2V_C - V_{ac}$.

④ When $t \in [t_3, t_4]$, the Z-Source inverter is operating at *Mode II*. Another of the non-zero input current-vectors is applied. The inductor voltage is $V_{L1} = -(V_C - V_{ac})$, and the output voltage of the Z-Source network is $V_0 = 2V_C - V_{ac}$.

⑤ When $t \in [t_4, t_5]$, the Z-Source inverter is operating at *Mode I*. The zero input current-vector is applied. The inductor voltage is $V_{L1} = -V_C$, and the output voltage of the Z-Source network is $V_0 = 2V_C$.

⑥ When $t \in [t_5, t_6]$, the Z-Source inverter is operating at *Mode III*. This is the shoot-through state. During this period, all the switches in the rectification stage are off, separating the DC-link from the input AC supplies. The inductor voltage is $V_{L1} = V_C$, and thereby the inductor current is increasing. The output voltage of the Z-Source network is $V_0 = 0$.

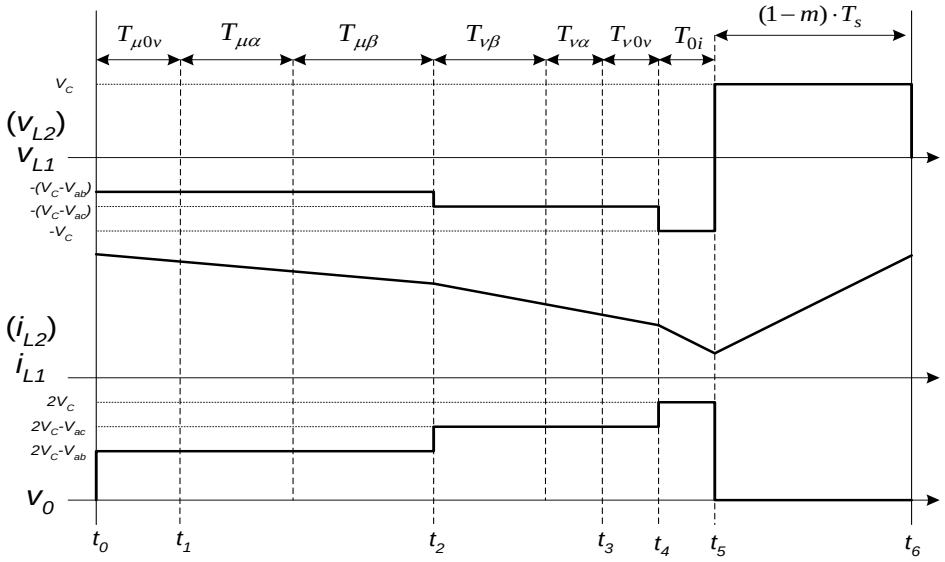

Fig.4.12 Operating waveforms of the Z-Source inverters

4.4.2 Obtainable voltage transfer ratio

From the symmetry and the equivalent circuits, we have

$$V_{C1} = V_{C2} = V_C \quad \text{and} \quad v_{L1} = v_{L2} = v_L \tag{4.8}$$

The average voltage of the inductors over one switching period (T_s) should be zero in steady state. Thus we have

$$\begin{aligned} V_L = \bar{v}_L &= \frac{-(V_C - V_{ab})\cdot T_\mu - (V_C - V_{ac})\cdot T_v - V_C \cdot T_{0i} + V_C \cdot (1-m)\cdot T_s}{T_s} \\ &= 0 \end{aligned} \tag{4.9}$$

Utilizing (4.7), then (4.9) can be rewritten as

$$\frac{V_C}{V_{pn}} = \frac{m}{2m-1} \tag{4.10}$$

Where, V_{pn} is the DC-link voltage expressed in (4.6), $m \in [0,1]$ is the modulation index of the proposed Z-Source inverters.

Consequently, the average DC-link voltage across the inversion stage can be found as:

$$V_0 = \bar{v}_0 = \frac{(2V_C - V_{ab}) \cdot T_\mu + (2V_C - V_{ac}) \cdot T_\nu + 2V_C \cdot T_{0i}}{T_s} \tag{4.11}$$

Together with (4.7) and (4.10), the (4.11) can be rewritten as

$$V_0 = \bar{v}_0 = m \cdot (2 \cdot V_C - V_{pn}) = \frac{m}{2m-1} V_{pn} \tag{4.12}$$

Furthermore, we define the peak phase-voltage of the inversion stage as V_{om}, and substituting V_{pn} from (4.6) into (3.12), the obtainable voltage transfer ratio is derived as

$$\frac{V_{om}}{V_{im}} = \frac{m}{2m-1} \cdot \frac{\sqrt{3}}{2} \cos\varphi_i \tag{4.13}$$

Where, φ_i is the input power factor angle.

4.5 Simulation and experimental verification

The integration of the three-switch buck-type rectifier and the Z-Source inverter is modeled with the developed modulation scheme. The simulation study is set up with the parameters shown in Table 4.1.

Table 4.1 Parameters of the three-switch buck-type rectifier based Z-Source inverter

Items	Value
Input AC source	120V/ 50 Hz (line-to-line RMS)
Commanded output voltage	220V/ 25Hz (line-to-line RMS)
Load resistance	30 Ω
Load inductance	25 mH
Input power factor	1
Switching frequency	5 kHz
Inductor L_1 and L_2	3 mH
Capacitor C_1 and C_2	470 uF

4.5.1 Simulation results

All the simulation has been performed by the output second-order filter with cutoff frequency of 1 kHz. By inserting the shoot-through modes, the magnitude of the output line-to-line voltage was boosted to 220V rms and was confirmed by the sinusoidal waveform (Fig.4.13 (a) and (b)). During the simulation, the modulation index *m* was set as 0.65 in order to obtain the commanded output voltage. Thus the traditional MC cannot produce 220V rms since the limit of voltage transfer ratio at 0.866. Figure 4.14 shows the Z-Source network capacitor voltage and the inductor current. The capacitor voltage has been boosted to 317.5V. The traces of V_{C1} and V_{C2} coincided with each other and so did the two inductor currents i_{L1} and i_{L2}. The equivalent DC voltage across the back-end inverter, V_0 was boosted to 311 V (which was illustrated from the output phase-voltage shown in Fig. 4.13).

Figure 4.15 shows the input waveforms of the Z-Source inverter. The desired unity input power factor is obtained. Figure 4.15 (b) and (c) present the input phase current waveforms before and after the input filter. Unlike the diode front-end Z-Source inverter [106], the developed converter still exhibits the good input current performance of IMC.

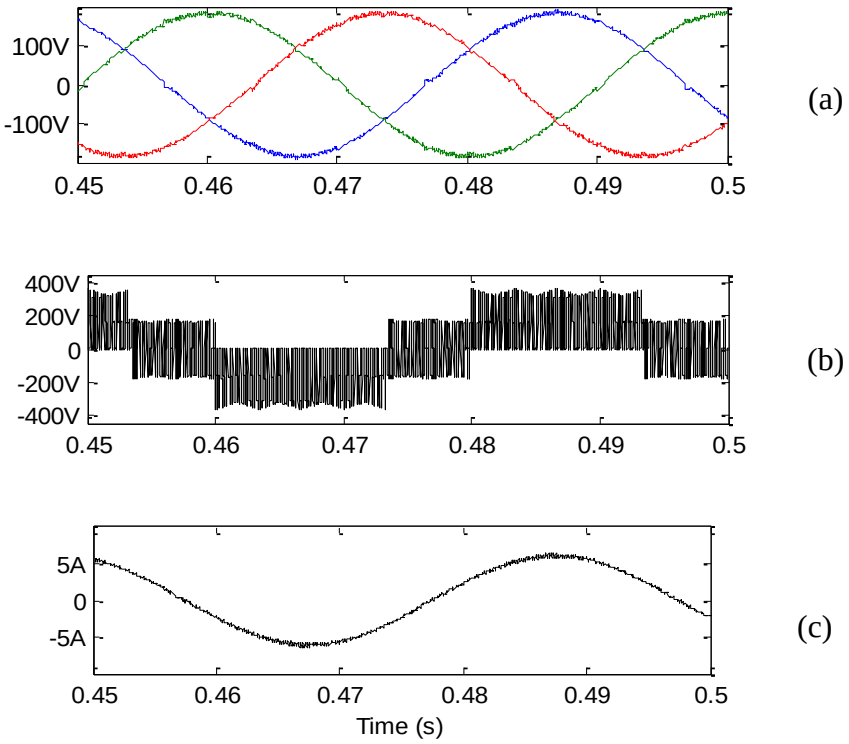

Fig.4.13 Simulation results of output voltage and current with shoot-through
(a) Phase voltages (b) Phase A PWM voltage (c) Phase A load current

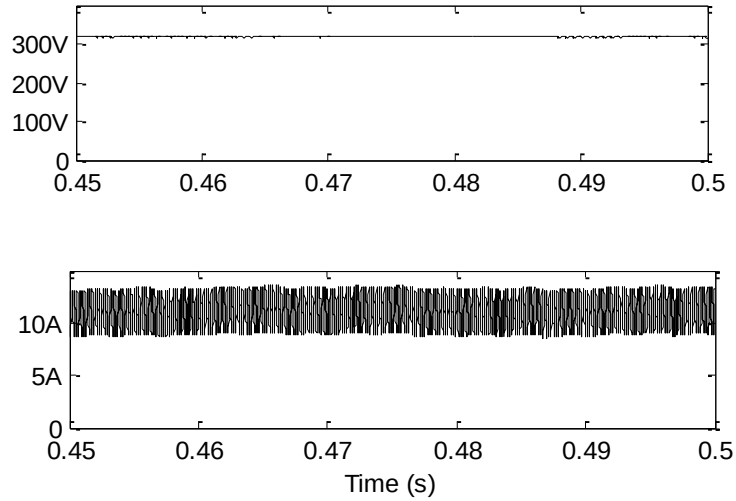

Fig.4.14 Simulation results of DC-link voltage and current waveforms with shoot-through

(a) Z-Source capacitor voltage (b) Z-Source inductor current

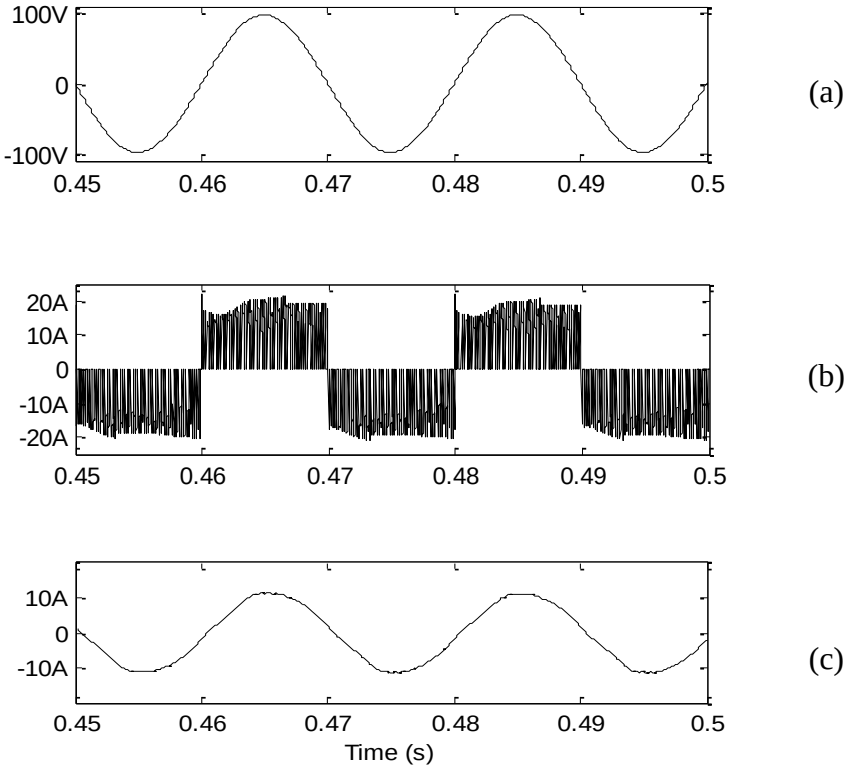

Fig.4.15 Simulation results of input voltage and current waveforms with shoot-through

(a) input Phase a voltage (b) input Phase a current before input filter (c) input Phase a current after input filter

4.5.2 Experimental results

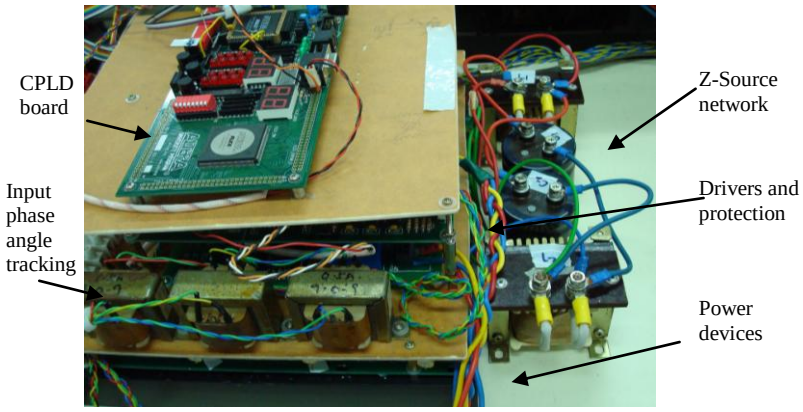

Fig.4.16 Photograph of the prototype of three-switch buck-type Z-Source inverter

A laboratory prototype of the three-switch buck-type Z-Source converter has been constructed to demonstrate the aforementioned modulation. The switching times and switch vectors are calculated by Dspace 1103 and then transferred to CPLD (Altera EPM7128) that generates each of the switch gate signals. The physical arrangement of the converter, which includes all power devices, gate drives, passive components and control boards can be seen from the photograph in Fig.4.16.

Experimental measurements of the topology have been made on the input currents and voltages, Z-Source network voltages and currents, and the output voltages. The operating conditions in Table 4.1 are also applied to conduct the corresponding experiments. Figure 4.17 and 4.18 show the experimental results of the DC-link voltage and output voltages under non-shoot through condition, respectively. It can be seen from Fig.4.17 that the instantaneous DC-link voltage is switched to v_{ab} for a duration of 60^0. This is followed with the control principle of IMC. The average DC-link voltage is equivalent to a constant, which serves as the input of the Z-Source network. Figure 4.18 shows the unfiltered output voltage, filtered voltage and current flowing in the RL load. The output current is sinusoidal and has a fundamental frequency according to the command. However, the voltage transfer ratio, which is theoretically limited to 0.866, is actually even lower as seen in Fig.4.18. All the experiments have been performed by a second-order filter with cutoff frequency of 1 kHz, which is similarly used in the simulation study.

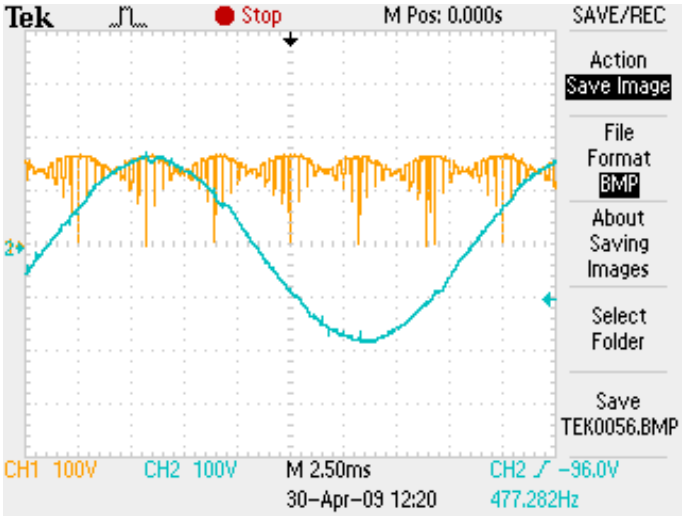

(Channel 1: DC-link voltage of the front-end circuit, Channel 2: Line-to-line voltage of v_{ab})

Fig.4.17 Experimental results of DC-link voltage and current waveforms without shoot-through

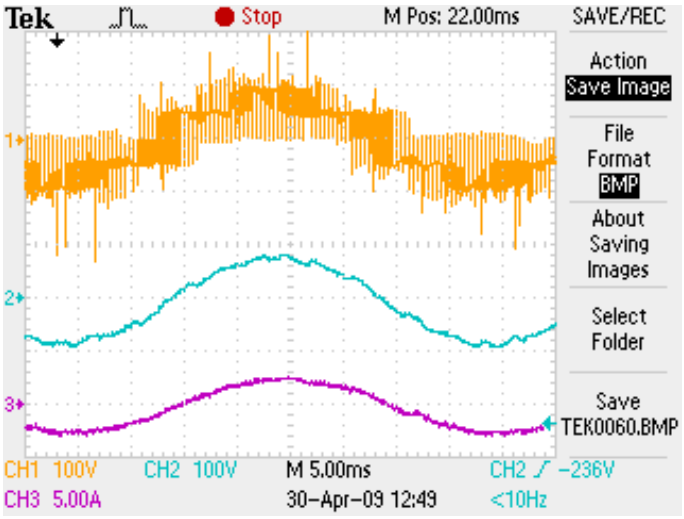

(Channel 1: PWM based Phase A voltage, Channel 2: Phase A voltage after filter, Channel 3: Load current on Phase A)

Fig.4.18 Experimental results of output voltage and current waveforms without shoot-through

Figure 4.19 and 4.20 show the experimental results of the Z-Source network voltage and current, the output voltage and current waveforms, respectively. Herein, the modulation index *m* is generally reduced from 1, which means the shoot-through duration is increased, until the output voltage meets the commands. From Fig.4.19, the Z-Source capacitor voltage has been boosted to nearly 320V, compared to the DC-link voltage of 150V from

Fig.4.17. Thereby the output voltage has been boosted to the commanded voltage. From Fig.4.20, the output current is still sinusoidal and has met the commanded frequency although the shoot-through states are inserted into the back-end inversion bridges. Therefore, the three-switch buck-type Z-Source inverter is successfully operating as a buck-boost AC-AC power converter. Figure 4.21 shows the supply-phase voltage, the modulated supply-phase current and near-sinusoidal filtered current waveforms. From Fig.4.21, sinusoidal input current is achieved and unity power factor control is possible.

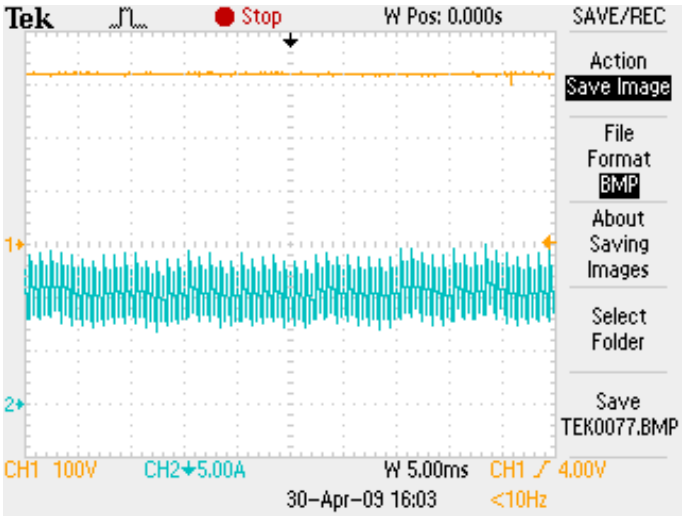

(Channel 1: Z-Source capacitor voltage, Channel 2: Z-Source inductor current)

Fig.4.19 Experimental results of DC-link voltage and current waveforms with shoot-through

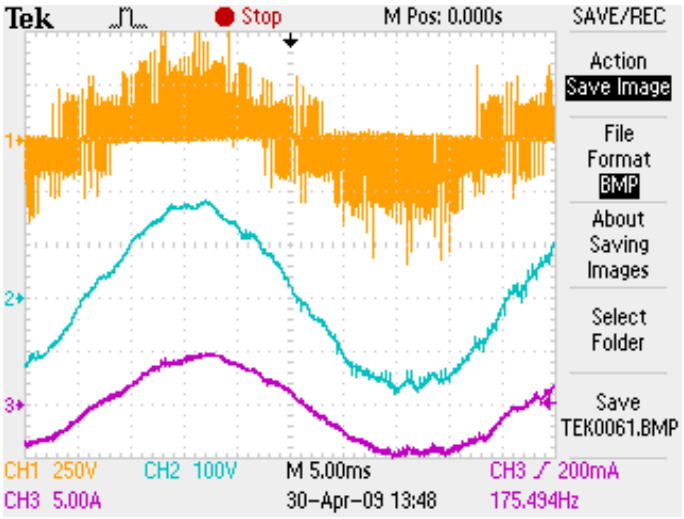

(Channel 1: PWM based Phase A voltage, Channel 2: Phase A voltage after filter, Channel 3: Load current on Phase A)

Fig.4.20 Experimental results of output voltage and current waveforms with shoot-through

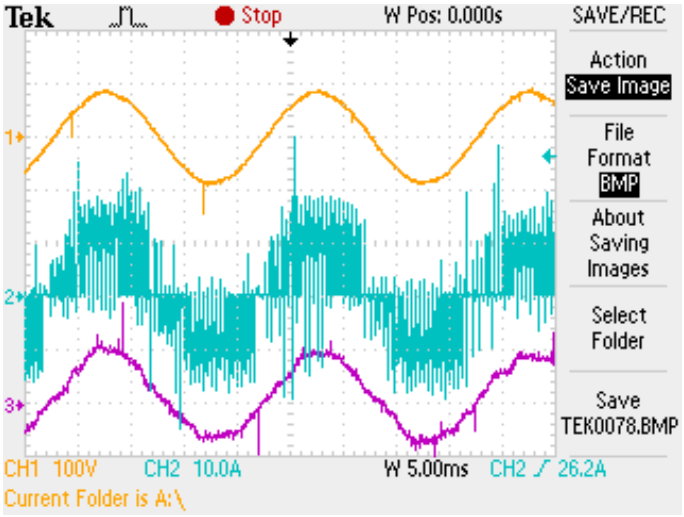

(Channel 1: input Phase a voltage, Channel 2: input Phase a current before input filter, Channel 3: input Phase a current after input filter)

Fig.4.21 Experimental results of input voltage and current waveforms with shoot-through

4.6 Comparison of simulation and experimental results

In order to completely evaluate the system performance, it is necessary to compare the simulation and experimental results in terms of several performance parameters, such as power factor, THD, ripple on the DC link.

Numerical simulation normally consists of ideal operating conditions, i.e., the ideal components/switches, fast-enough control processor, real-time sampling without delay, and no measurement and calculation error and so on. However, in the lab-based prototype, the power semiconductor switch, i.e., IGBT, is definitely not like the ideal switch used in the simulation. The real switch has switching loss, reverse current, internal resistance and so on, and all of these non-ideal factors will impact on the system performance. In addition, digital signal processor (DSP) is widely used in experimental verification, and the sampling time is limited by the processing speed of the used DSP.

Bearing all these in mind, the performance of simulation is better than that of experimental studies in terms of power factor control, THD of input current, and DC-link voltage ripple. The input current distortion in the experimental results is larger than that in the simulation, and thereby the input power factor control in experiment is better than that

in simulation as well. In addition, the parasite parameters in the prototype also impact on the DC-link voltage, which can be found from the simulation and experimental studies.

4.7 Conclusions

This chapter discussed the development of the three-switch buck-type rectifier based Z-Source inverter and the proposed modulation scheme has been presented in detail. All these are the prerequisite conditions to apply the developed converter for any WTG configuration which requires full power converter. The simulation studies and experimental results have verified the concept of integrating the three-switch rectifier with a Z-Source inverter. From the aforesaid results, the developed converter exhibits good reliability due to shoot-through allowance and less power semiconductor switches compared with the conventional back-to-back topology. The detailed design methodology and verification of the proposed architecture for PMSG application will be discussed in the next chapter.

CHAPTER 5

DESIGN OF A ROBUST PMSG TURBINE SYSTEM BASED ON THE DEVELOPED TOPOLOGY

5.1 Introduction

The modulation, analysis and demonstration of the three-switch buck-type rectifier based Z-Source inverter have been introduced in Chapter 4. This chapter presents the design of a robust PMSG wind turbine based on the aforementioned topology. Figure 5.1 shows the proposed PMSG based wind generation system, which provides high reliability, low capital cost, and harmonic-free characteristics in both generator and grid sides.

From Fig.5.1, the wind power captured by the turbine is converted by the PMSG and transferred to the grid via a three-phase three-switch PWM buck-type rectifier in series with a Z-Source inverter. The detailed power circuit is illustrated in Fig.5.2, which has been analyzed in Chapter 4. The main function of the generator-side PWM rectifier is to regulate the power factor of PMSG and to ensure sinusoidal generator currents. A small LC input filter can be designed to absorb the high frequency harmonics injected into the generator by the rectifier switching action. The grid-side inverter serves as a grid power interface to connect PMSG with network utility. The detailed generator-side and grid-side control scheme will be discussed in this chapter.

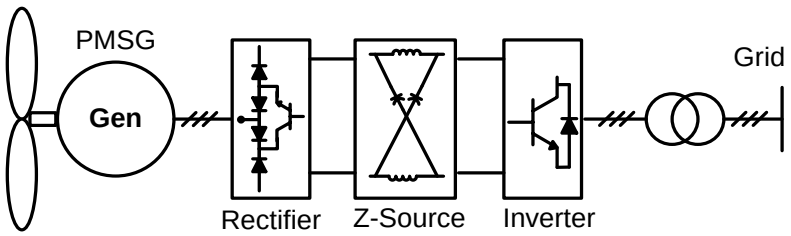

Fig.5.1 Proposed PMSG based wind generation system

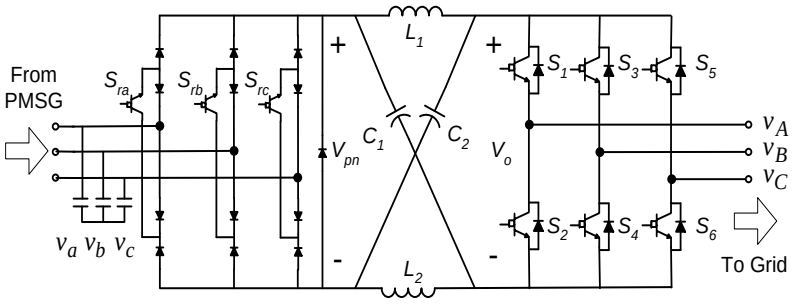

Fig.5.2 Three-switch buck-type rectifier based Z-Source inverter for PMSG

5.2 Generator-side (PMSG) control principle

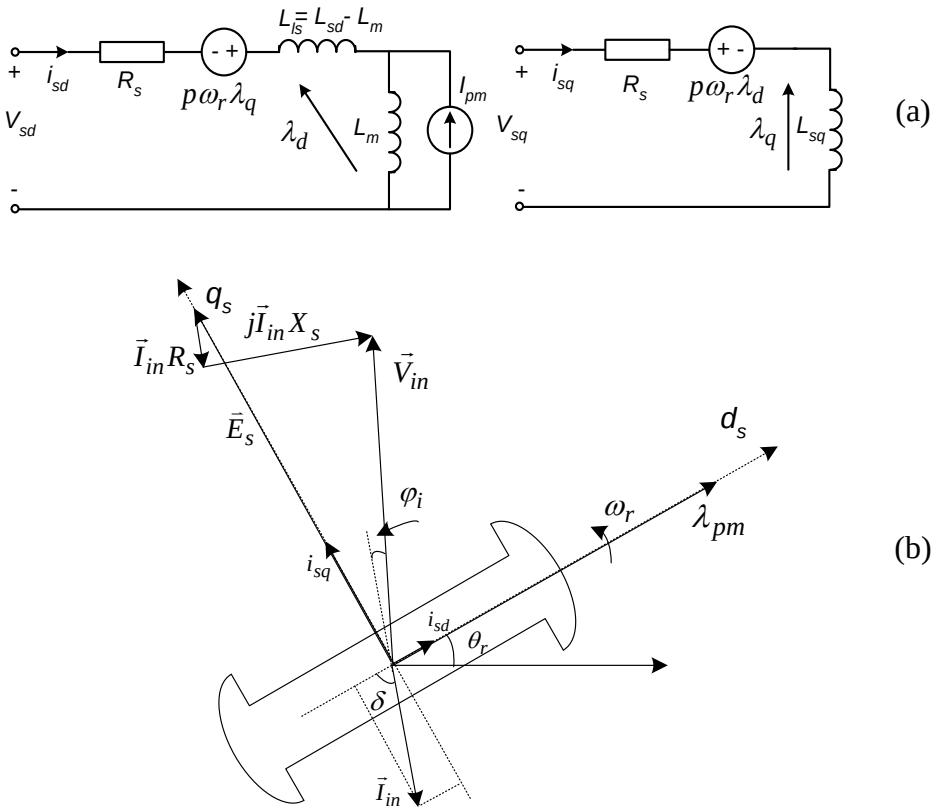

Fig.5.3 Equivalent circuit and phasor diagram of the PMSG
(a) equivalent circuit (b) phasor diagram

The control strategy for the generator-side converter (the three-switch buck-type rectifier) is discussed based on the equivalent circuit and phasor diagram of PMSG illustrated in Fig.5.3. The generator terminal voltage serves as the input voltage to the rectifier, termed

as $\vec{V}_{in}$, which is equal to the machine back-EMF $\vec{E}_s$ minus the voltage drop in the machine impedance (R_s+jX_s). From the equivalent circuit, the steady-state equation of PMSG can be expressed as

$$\begin{bmatrix} V_{sd} \\ V_{sq} \end{bmatrix} = \begin{bmatrix} R_s & -p\omega_r L_{sq} \\ p\omega_r L_{sd} & R_s \end{bmatrix} \cdot \begin{bmatrix} I_{sd} \\ I_{sq} \end{bmatrix} + \begin{bmatrix} 0 \\ p\omega_r \lambda_{pm} \end{bmatrix} \tag{5.1}$$

Where, R_s, L_{sd} and L_{sq} are the PMSG stator resistance, direct-axis and quadrature-axis inductances, respectively. ω_r is the generator speed, p is the PMSG pole pairs and $\lambda_{pm}=L_m I_{pm}$ is the permanent magnetic flux. Herein, two control schemes: unity power factor control and $I_d=0$ control, are discussed in this section.

5.2.1 Unity power factor control of PMSG

From Fig.5.3, the angle φ_i between the PMSG terminal voltage and the generator stator current is equal to the input power factor angle of the three-switch buck rectifier, assuming small capacitance of the filter. Unity power factor control of the rectifier can be implemented by making the stator current vector follow the measured terminal voltage vector. That means the angle φ_i is kept at zero, which means the rectifier can be treated as an equivalent ‘resistance’ load of the PMSG. Thereby the generator current harmonics can be reduced and the generator efficiency can be improved compared to the conventional diode-rectifier topology, where the sinusoidal generator current cannot be achieved.

With unity power factor control, the overall volt-ampere of the front-end rectifier would contribute to the active power transfer and thereby reduce the power rating of the proposed configuration. This would lead to a smaller size and hence reduce the cost of power circuit, which is one of the significant considerations for MW-level wind turbine design.

5.2.2 Id=0 control of PMSG

The $I_d=0$ control is applied to improve the efficiency of machine. With this control, the machine torque is coordinated with the magnitude of the q-axis current, while the d-axis current is always kept as zero (I_d =0).

According to the rotor flux oriented strategy, the stator current vector should always be kept aligned with the back EMF of PMSG. In other words, the torque angle δ should be controlled as,

$$\delta = 90^0 \tag{5.2}$$

Equation (5.2) denotes the fundamental principle of $I_d=0$ control. The input power factor of the front-end rectifier can be flexibly adjusted by changing current space vector angle. Specifically, the reference of the current-vector is easily obtained by utilizing rotor position signal of the PMSG with a constant angle bias (90^0).

5.2.3 Optimized control strategy of PMSG

The $I_d=0$ control can provide the maximum torque per ampere. However, for the $I_d=0$ control, the maximum available speed is limited to a base value, which depends on the DC-link voltage and machine back EMF. Alternatively, this limitation can be explained using the power factor angle φ_i of the $I_d=0$ control, which can be derived from (5.1) as,

$$\varphi_i = \cos^{-1}\frac{V_{sq}}{\sqrt{V_{sq}^2+V_{sd}^2}} = \cos^{-1}\frac{1}{\sqrt{1+\dfrac{(L_{sq}I_{sq}/\lambda_{pm})^2}{(1+R_sI_{sq}/\omega_r\lambda_{pm})^2}}} \tag{5.3}$$

From (5.3), the power factor deteriorates with increasing rotor speed as well as with increasing stator current. This control results in a relatively low power factor of PMSG, especially at the rated power and overload operation [69]. Therefore, the lower the power factor, the higher the DC-link voltage is required in order to keep the same torque. Once the DC-link voltage is selected, the low power factor results in the reduction of the speed operating range.

The unity power factor control means that it is still able to increase the voltage for wider range of speed operation before reaching the base value, while the machine torque is kept constant. Consequently, the base operating speed range can be extended significantly compared to the $I_d=0$ control. This principle is similar to the field weakening control of motor drive. However, this control strategy is not optimal in terms of efficiency as compared to the $I_d=0$ control. The fundamental machine loss is also evaluated by the generator torque angle δ, which can be derived from (5.1) as,

$$\delta = \cos^{-1}\frac{I_{sd}}{\sqrt{I_{sq}^2 + I_{sd}^2}} = \cos^{-1}\left[\sqrt{\frac{L_{sq}I_{sd}}{\lambda_{pm} + (L_{sd} - L_{sq})I_{sd}}}\right] \tag{5.4}$$

From (5.4), the δ can be more than or less than 90^0 with increasing stator current. A torque angle larger than 90^0 will result in an increase of flux linkage contributing to machine saturation. Hence, the torque per ampere is less than one, indicating that the unity power factor control is not optimal in terms of torque generation. The efficiency will be reduced by the increased copper losses for generating the same torque.

In order to obtain both maximum efficiency and maximum torque per ampere, it is preferable to incorporate the $I_d=0$ control with the unity power factor control, specifically: the $I_d=0$ control is used before reaching the base speed, while the unity power factor control is selected after this base speed.

In order to determine the speed boundary, the system real power P is expressed as

$$P = S \cdot \cos\varphi_i = V \cdot I \cdot \cos\varphi_i \tag{5.5}$$

Where, V and I are the system rating voltage and current, respectively. S is the system apparent power. The curve of the power factor angle φ_i versus the real power can be calculated by (5.3) with the PMSG parameters. From (5.5), we can obtain the relation between the real power and apparent power. Herein, if the S is set as 1 p.u, the boundary real power can be determined. Therefore, the speed boundary can be derived from the speed-power relationship, which will be introduced in the following section.

5.3 System control scheme considering turbine characteristics

5.3.1 Maximum power point tracking

Due to the horizontal wind turbine, the mechanical power captured by the turbine can be expressed as [107]

$$P_m = 0.5\rho A C_p v_w^3 \tag{5.6}$$

Where, ρ is the air density, A is the swept area of wind turbine, v_w is the wind speed, and C_p is the power coefficient defined as a function of the tip speed ratio $\lambda = \omega_r R / v_w$, ω_r and R are the rotor speed and radius of wind turbine respectively. Figure 5.4 shows the relation between generator speed and output power according to wind speed change. Herein the rated wind speed is 16 m/s. It is observed that the maximum power tracking point (MPPT) occurs at different generator speeds for different wind speeds.

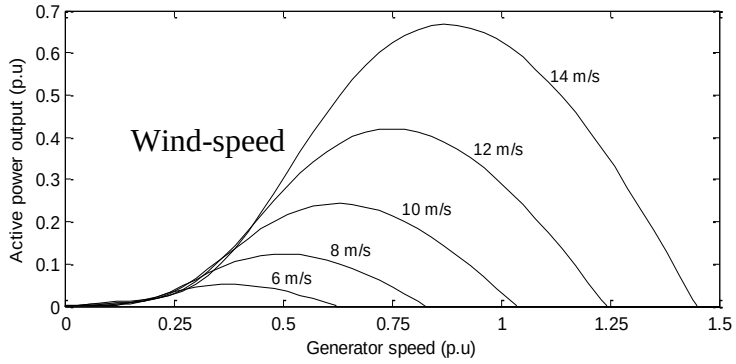

Fig.5.4 The turbine power output versus the generator speed under different wind speeds

According to (4.10), the capacitor voltage of the Z-Source network can be rewritten as

$$V_C = V_{C1} = V_{C2} = \frac{1-D}{1-2D} V_{pn} \tag{5.7}$$

Where, $D = T_{st}/T_s$ is the shoot-through duty-cycle. The shoot-through of the Z-Source inverter is desired to be controlled in order to achieve variable speed operation of the system. The terminal voltage of PMSG is decided by the generator speed. So the input voltage of the Z-Source network V_{pn} also relies on the speed of PMSG. In other words, the control of generator speed can be implemented by regulating the V_{pn}. From (5.7), V_{pn}

can be adjusted by changing duty-cycle of shoot-through state while the capacitor voltage V_C is kept constant. The capacitor voltage can be controlled as a constant by regulating the active power delivered to the grid.

With the capacitor voltage regulated, the relation between shoot-through duty-cycle and generator speed can be derived from (4.6) and (5.7) as

$$m = \frac{1-D}{1-2D} = \frac{V_c}{1.5k\omega_r \cos\varphi_i} \tag{5.8}$$

Where, k is the back EMF constant of PMSG. From (5.8), the generator speed ω_r can be regulated by the control of D. The corresponding system control scheme for MPPT is depicted in Fig.5.4. Herein the MPPT is based on wind-speed measurement. Using the measured wind speed, the required rotor speed (optimized speed) for maximum power generation is computed. Then the actual rotor speed is also measured and compared to the calculated optimal rotor speed, while the resulting error is used to control the grid interface system. In this study it is designed to regulate the shoot-through duty-cycle in order to control the speed.

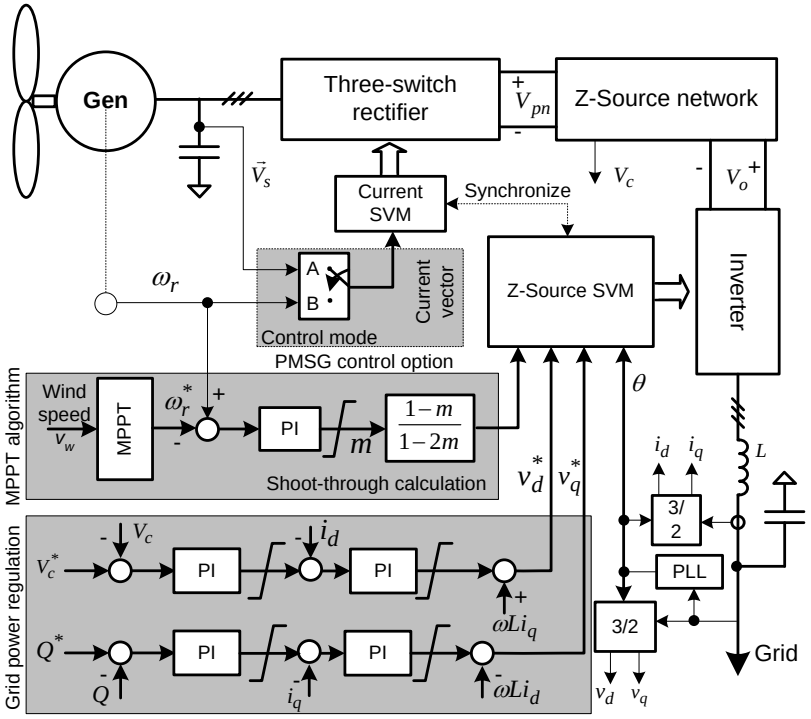

Fig.5.5 System control diagram of the developed PMSG wind generation system

The PMSG control scheme is presented in Fig.5.5. Any of the two different control schemes mentioned are utilized to control the PMSG, which is decided by the wind power obtained from (5.5). The Z-Source inverter serves as a power interface to feed captured wind power into the grid. The detailed vector-control of the grid-side inverter is given in the next section.

5.3.2 Control of power delivered into grid

The dynamic model of the grid connection when selecting a reference frame rotating synchronously with the grid voltage space vector is

$$\begin{aligned} u_d &= u_{id} - Ri_d - L\frac{d}{dt}i_d + \omega L i_q \\ u_q &= u_{iq} - Ri_q - L\frac{d}{dt}i_q - \omega L i_d \end{aligned} \tag{5.9}$$

Where, L and R are the grid inductance and resistance, respectively, and u_{id} and u_{iq} are the inverter voltage components. If the reference frame is oriented along the supply voltage, the grid voltage vector is

$$u=u_d+j0 \tag{5.10}$$

Then the active and reactive power feeding into the grid can be expressed as

$$\begin{aligned} P &= 1.5u_d i_d \\ Q &= 1.5u_d i_q \end{aligned} \tag{5.11}$$

Active and reactive power control can be implemented by controlling direct- and quadrature-current, respectively. The control of the grid-side converter is presented in Fig.5.5. An outer DC voltage control loop is used to set the d-axis current reference for active power control. This makes sure all the power coming from the rectifier is instantaneously fed into the grid by the Z-Source inverter. On the other hand, the second current control loop is designed to control the reactive power by setting q-axis current reference to a current loop. The current controller will provide a voltage reference for the inverter that is compensated by adding the direct-axis and quadrature-axis intersection terms.

5.4 Design consideration of the passive components

In this section, the passive components of the proposed topology are calculated analytically based on the system operating condition. This provides the basis for the design method for the various circuit components.

5.4.1 Parameters design of the Z-Source network

Based on the analysis in Section 4.4, the average current through the rectifier circuit is equal to the sum of the average current through the inductor L_1 and capacitor C_1. In steady state, the average current through the inductor equals to that of the rectifier. If the output power is P_o, therefore, the average current through the rectifier switches as well as the inductor is

$$I_L = P_o / V_{pn} = P_o / (1.5 V_{im} \cos\varphi_i) \tag{5.12}$$

The Z-Source capacitor value is selected according to the voltage ripple and the capacitor current. Then from the mode *III* in Fig.4.11, when the capacitor current equals the Z-Source inductor current, then we get

$$C = \frac{I_L}{\Delta V_C} \cdot DT_s \tag{5.13}$$

If ΔV_C is selected as $\Delta V_C \le k_1\% V_C$, we have

$$\begin{aligned} C &\ge \frac{DT_s}{k_1\% V_C} I_L = \frac{(1-2D)DT_s}{(1-D)k_1\% V_{pn}^2} P_o \\ &= \frac{(1-2D)DT_s}{2.25\times(1-D)k_1\% V_{im}^2 \cos^2\varphi_i} P_o \end{aligned} \tag{5.14}$$

The Z-Source inductor value is selected according to the current ripple; from the mode *III* again, the inductor voltage equals the Z-Source capacitor voltage, then we get

$$L = \frac{V_C}{\Delta I_L} \cdot DT_s \tag{5.15}$$

If ΔI_L is selected as $\Delta I_L \le k_2\%\ I_L$, we have

$$\begin{aligned} L &\ge \frac{DT_s}{k_2\%I_L}V_C = \frac{(1-D)DT_s}{(1-2D)k_2\%P_o}V_{pn}^2 \\ &= 2.25\frac{(1-D)DT_s}{(1-2D)k_2\%P_o}V_{im}^2\cos^2\varphi_i \end{aligned} \tag{5.16}$$

5.4.2 Parameters design of the generator-side filter

Filters must be used at the input of the three-switch buck-type rectifier to reduce the switching frequency harmonics presented in the input current. The filter requirements are as follows:

1) To have a cutoff frequency lower than the switching frequency of the converter;

2) to minimize its reactive power at the rated condition;

3) to minimize the filter inductance voltage drop at rated current in order to avoid a reduction in the voltage transfer ratio.

According to these guidelines, the reactive power of the filter usually has to be limited to 5~10% of the rated power in order to ensure high power factor, so the capacitance C_{in} of the generator-side filter can be calculated by

$$C_{in} \le \frac{(5\sim 10\%)\cdot P_{in}}{2\pi f_{in}V_{in,l-l,rms}^2} \tag{5.17}$$

The generator-side filter inductance is designed by the cut-off frequency f_c, which should be lower than one-twentieth to one-tenth of the switching frequency f_s. For a given filter capacitor C_{in} then the filter inductance can be calculated by

$$L_{in} = \frac{1}{(2\pi f_c)^2 C_{in}} \approx \frac{1}{(2\pi\times 0.1 f_s)^2 C_{in}} \tag{5.18}$$

It should be noted that this generator-side filter inductance consists of the PMSG winding inductance and the external filter inductor.

5.5 Simulation and experimental verification

To verify the performance of the proposed wind generation system, simulation tests have been carried out. Major system parameters are listed in Table 5.1 according to the design consideration in the previous section.

Table 5.1 System Parameters of the Proposed Systems

System ratings	
Grid line-line voltage	127V / 50Hz
DC capacitor voltage	240 V
Cut-in wind speed	4 m/s
Rated wind speed	16 m/s
Generator parameter	
Rated power	1.5 KW
Rated frequency	50 Hz
Winding resistance	1.2 Ω
Winding inductance	6 mH
Number of poles	4
Rotor inertia	5.66 x 10-3 kgm2
Back EMF constant	0.832 V/ rad/s
Converter parameter	
Z-Source inductance	5 mH
Z-Source capacitance	1000 uF
Switching frequency	5 kHz
Grid-side inductance	5 mH
Generator-side inductance	1 mH
Generator-side capacitance	15 uF

5.5.1 Simulation results

In this simulation, the system is driven by a wind turbine model provided by Matlab/Simulink. The turbine model receives the wind speed and provides an optimized reference speed to the control system. The simulation results are shown in Fig. 5.6~5.12.

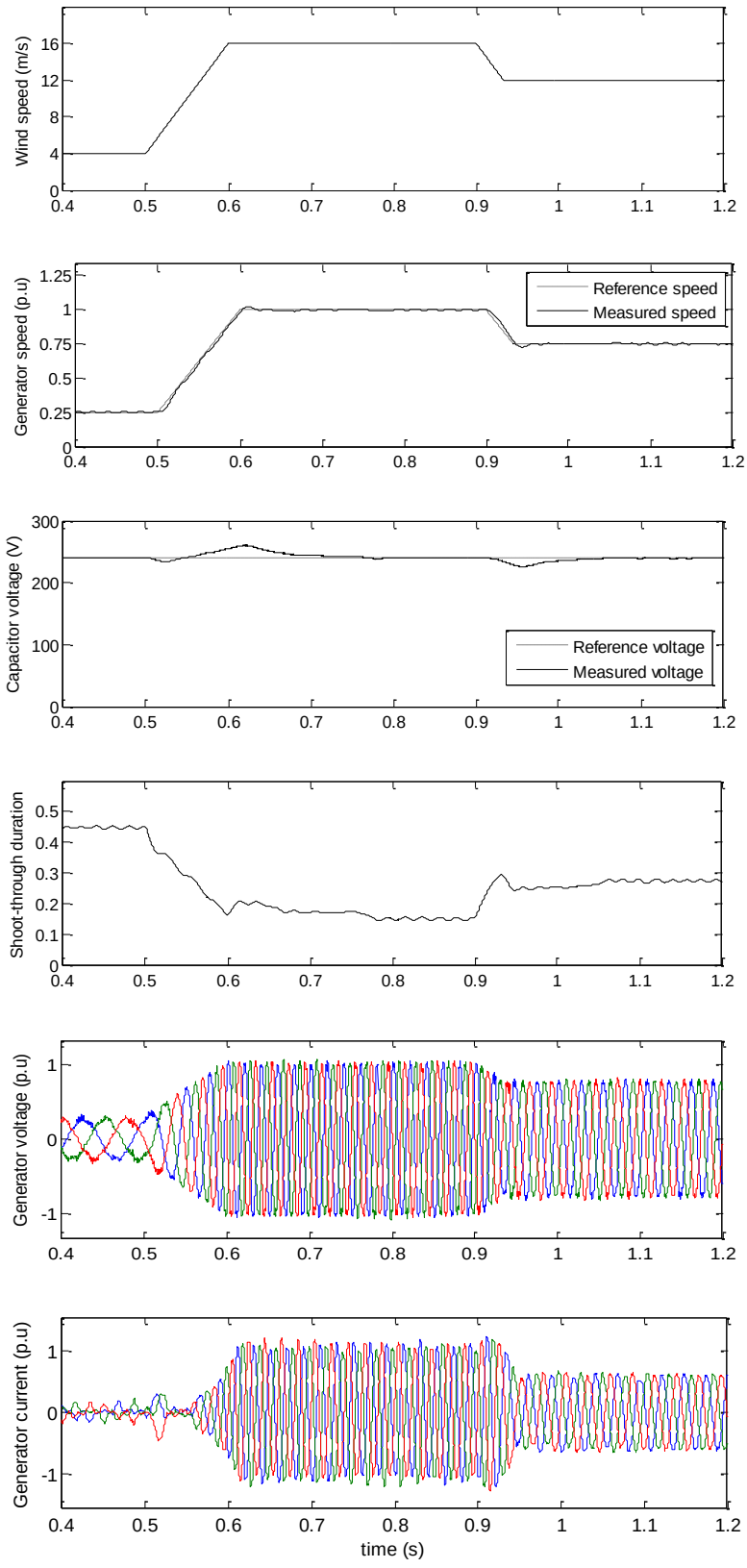

Fig.5.6 Simulation results of the PMSG-side operating profiles

(a) wind speed, (b) generator rotor speed, (c) Z-Source capacitor voltage, (d) shoot-through duty-cycle D, (e) generator phase-voltages and (f) generator currents

In order to simulate the transient response of the proposed control system, wind speed is assumed to have a step-up from 4 m/s to 16 m/s at 0.5 s, and a step-down from 16 m/s to 12 m/s at 0.9 s. Herein, 4 m/s and 16 m/s are the cut-in and the rated wind speeds, respectively. Figure 5.6 illustrates the operating waveforms of the generator-side converter. The reference speed for MPPT is shown in Fig.5.6(b). Figure 5.6 (c) shows the Z-Source capacitor voltage, which is controlled to 240V by the grid-side d-axis controller. At the instant when the wind speed steps up, the speed regulator reduces the shoot-through duty-cycle, thus helping to speed up the generator speed. The dynamic response of the shoot-through duty-cycle is shown in Fig.5.6 (d). The increase of the generator speed leads to higher generator voltages and currents, and hence higher generator output power. The transient PMSG phase-voltages and currents are shown in Fig.5.6 (e) and (f), respectively. The above analysis approach is also viable to study the generator operating condition when wind speed is step-down.

Figure 5.7 illustrates the grid-side characteristics of the proposed wind generation system. Herein, the negative value in Fig.5.7 (b) and (c) means the power is flowing into grid. The performance of MPPT can be evaluated from the power curves shown in Fig.5.7 (a) and (b). With the grid power regulation, the capacitor voltage is controlled to a constant 240V as shown in Fig.5.6 (c) and thereby the captured wind power can be fully fed into grid. This function is similar to that of grid-side inverter in the conventional power generation system [26].

The reactive power output is presented in Fig.5.7 (c). The reference of the reactive power is assumed to have a step-up from 0 to -0.22 pu at 1.1 s. It can be seen from Fig.5.6 and 5.7 that the active and reactive power can be regulated independently. This helps to overcome the ride-through problem, which is an important issue in the grid-connected wind generation system. The grid-side d-axis and q-axis currents are also presented in Fig.5.7 (d) and (e), respectively.

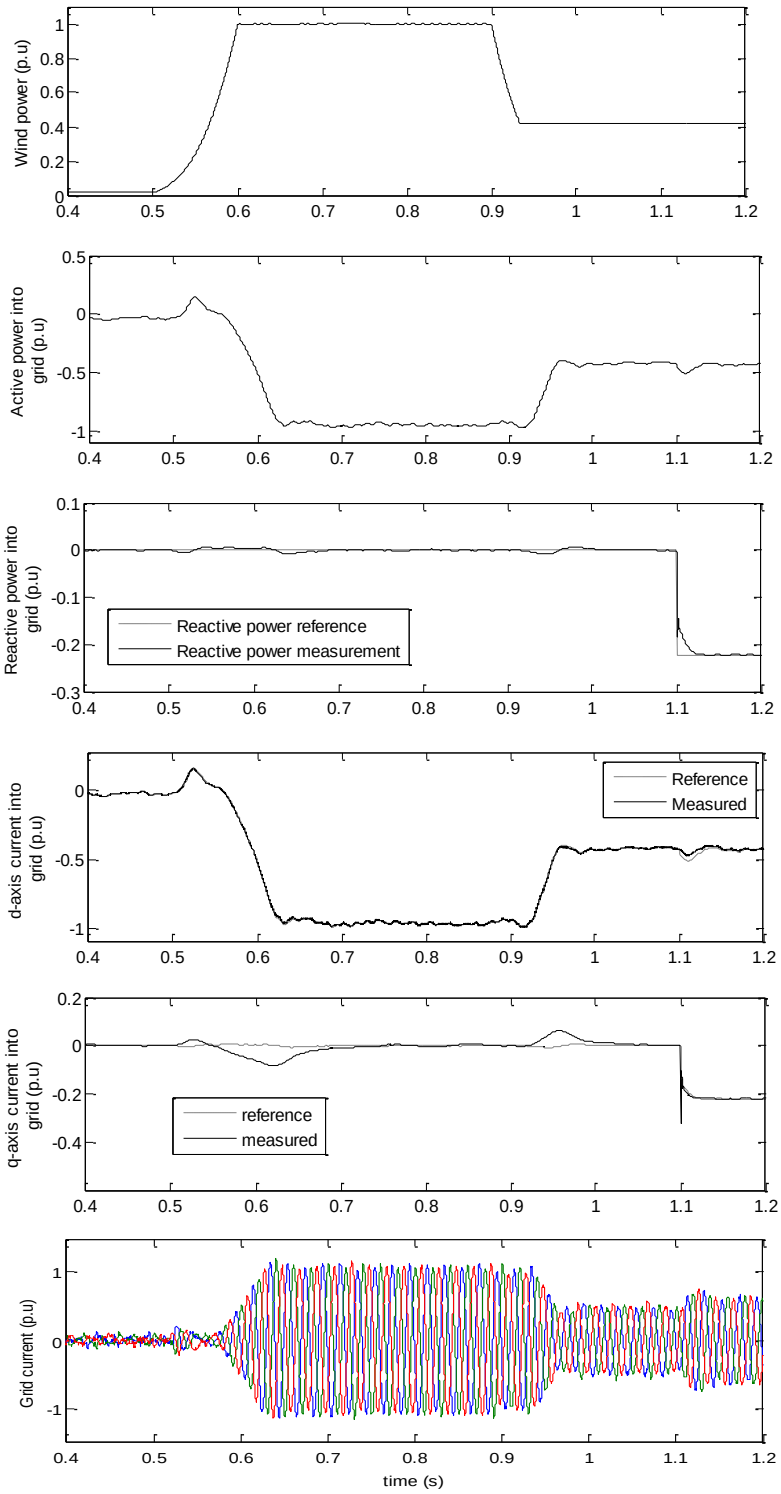

Fig.5.7 Simulation results of the grid-side operating profiles

(a) captured wind power by turbine, (b) real power flowing into grid, (c) reactive power output, (d) the d-axis current of the grid-side converter and (e) the q-axis current, and (f) the grid-side phase-currents

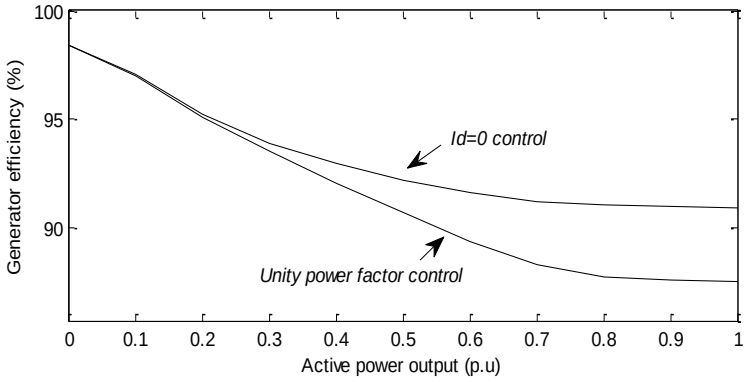

Fig.5.8 Comparison of efficiency of PMSG under different control principles

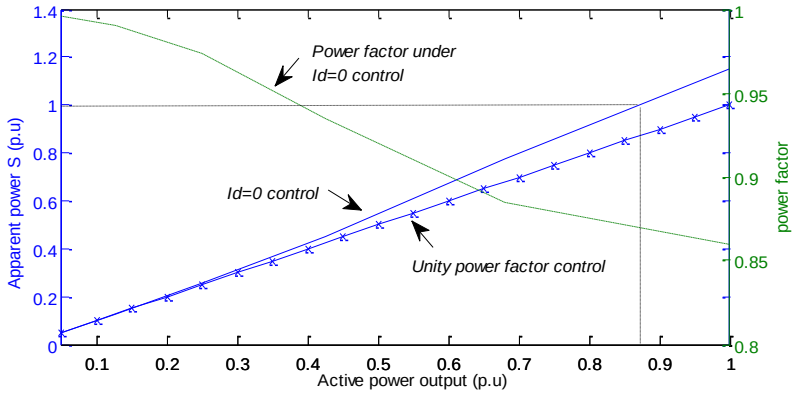

Fig.5.9 Comparison of the converter power ratings under different control principles

As illustrated in Fig.5.5, two PMSG control algorithms, the unity power factor control and the $I_d=0$ control, have been utilized to control the generator. In order to fully evaluate these two PMSG operating strategies, the detailed comparisons are presented in Fig.5.8 and 5.9 in terms of PMSG efficiency and system power rating. When wind power output increases, the efficiency of PMSG is reduced rapidly with the unity power factor method, as shown in Fig.5.8. On the contrary, the PMSG efficiency with the $I_d=0$ control is relatively higher than that with the unity power factor method. Under the unity power factor method, the direct-axis current is not regulated. However, the efficiency with the unity power factor method tends to be constant when power output is larger than 0.8 p.u.

On the other hand, from Fig.5.9, the PMSG power factor under the $I_d=0$ control is decreased when the wind power increases and thereby the system power rating under the $I_d=0$ control is increasing rapidly when wind power output is increasing. Thus the apparent power S under the unity power factor control is equal to the active power output

P. Hence, with the converter power rating constraint, it is superior to use the unity power factor control considering its full real power transfer capability.

The proposed PMSG control strategy is the integration of the unity power factor control and the $I_d=0$ control. Based on the discussion in Section 5.2.3, we assume the converter power rating to be 1 p.u. Consequently, the wind power boundary is chosen as 0.87 p.u, as illustrated in Fig.5.9. From (5.5), the speed boundary can be obtained as 0.95 p.u. That means the $I_d=0$ control is adopted when wind power output is smaller than 0.87 pu and the unity power factor method is utilized when wind power output is larger than 0.87 pu. The main objective of the proposed control strategy is to optimize the performance in terms of the system cost and efficiency.

Another important motivation to develop the proposed wind generation system is its low-harmonic characteristic. The proposed converter is compared with the conventional diode-front system and back-to-back converter, as shown in Fig.2.9 and 2.10, respectively. Figure 5.10, 5.11 and 5.12 shows the simulation results of PMSG terminal phase-voltage / current and the FFT spectrum/ total harmonic distortion (THD) of the current waveform. The generator speed along with wind speed is set as 0.4 p.u in both Fig.5.10, 5.11 and 5.12. The terminal phase-voltage is filtered by a second-order filter with 1000 Hz cut-off frequency and the same switching frequency is utilized in these three systems. It can be seen from Fig.5.10 that there are no low-order harmonics in the generator. This low-harmonic characteristic result from the utilization of the generator-side three-switch buck-type converter, and the THD of the generator current is only 2.76%. Figure 5.11 presents the simulation results of phase-voltage/current obtained by the diode front-end conventional system shown in Fig. 2.9. From Fig.5.11, there are significant 5th-order and 7th-order harmonics in the stator current. The current THD is up to 6.65%, which is much larger than that in the proposed system. High harmonic distortion currents also appeared in the generator that further reduce efficiency and produce torque oscillations. These are the drawbacks of the conventional diode front-end system. Figure 5.12 presents the simulation results of the back-to-back system. The current THD is only 2.2% and low-order harmonics are absent. However, the back-to-back converter would be much more expensive than other two topologies, especially for high power application.

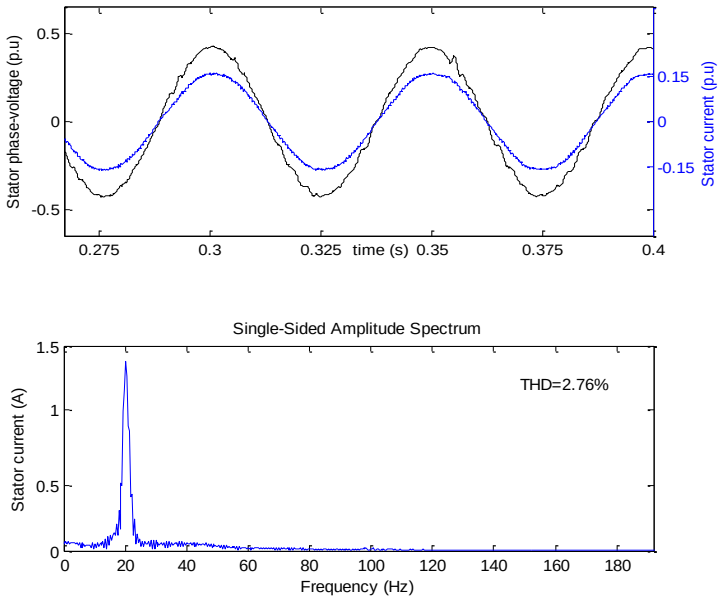

Fig.5.10 Simulation results of PMSG voltage and current waveforms in the proposed system

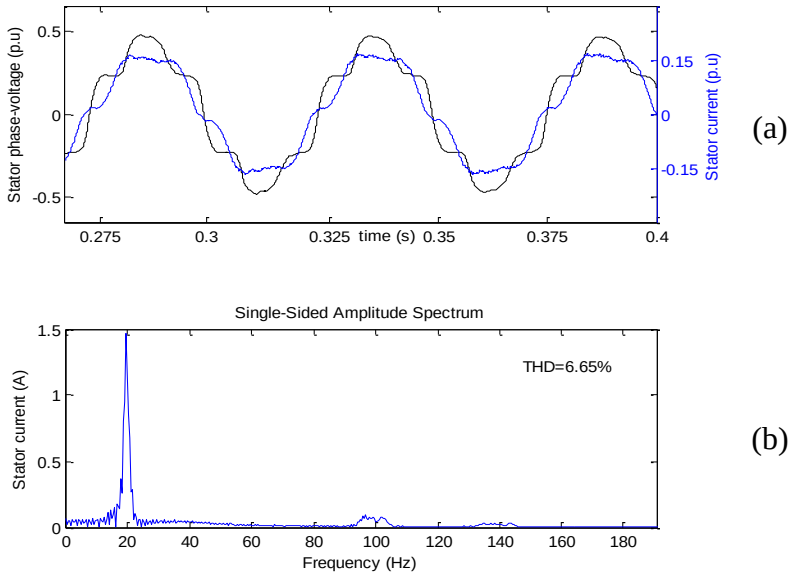

Fig.5.11 Simulation results of PMSG voltage and current waveforms in the conventional diode-fronted system

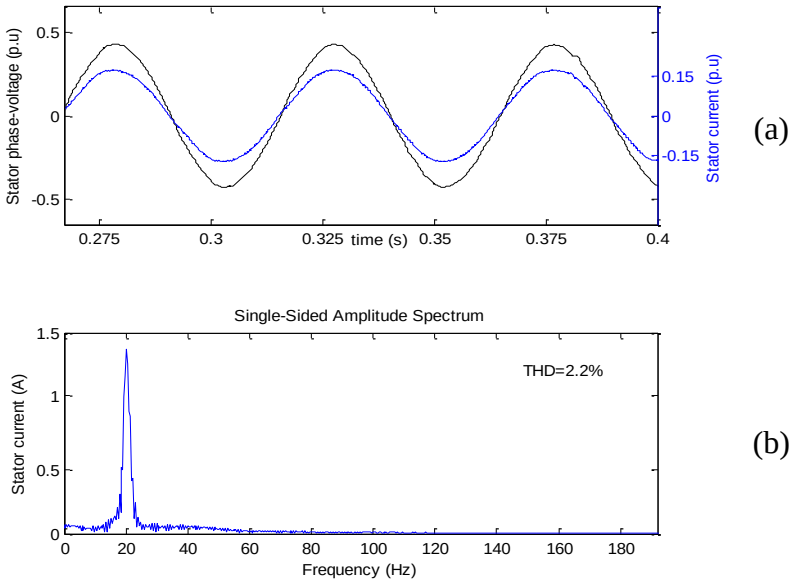

Fig.5.12 Simulation results of PMSG voltage and current waveforms in the back-to-back converter system

5.5.2 Experimental results

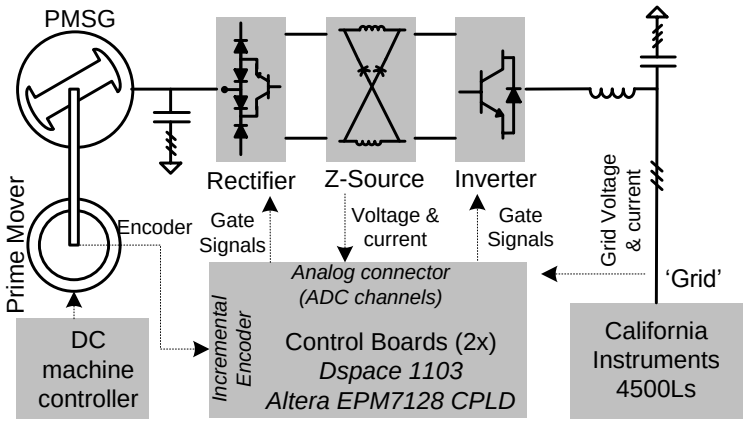

Fig.5.13 Experimental setup of the proposed system

A prototype system with detailed system parameters listed in Table 5.1 is constructed for experimental verification. The prime mover is a DC-machine controlled in torque producing mode, where the torque reference is desired to change along with rotor speed. Herein, a pre-set table between torque reference and speed is established based on the power characteristic of wind turbine, of which the mechanical torque is varied by the wind speed and generator speed. When the generator speeds up, the system starts

operation and the terminal voltage of PMSG is adjusted by the DC-link voltage controller, which maintains the generator speed to the desired value. Figure 5.13 shows the block diagram of the experimental system. The grid is simulated by an AC source (California Instruments 4500Ls). The control system is implemented on a platform consisting of Dspace 1103 and a complex programmable logic device (CPLD). The experimental results from the laboratory-prototype are shown in Fig.5.14~5.18.

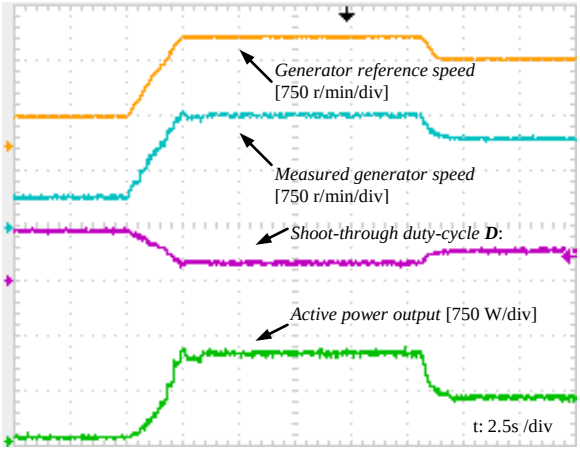

Fig.5.14 Experimental results of generator reference and actual speeds, the shoot-through duty-cycle D and active power output

Based on the aforesaid control algorithm, the generator speed can be regulated by the shoot-through duty-cycle *D*. Figure 5.14 shows the experimental results of the generator reference speed, actual speed and the related shoot-through duty-cycle. In Fig.5.14, the generator speed is assumed to have a step-up from 0.25 p.u to 1 p.u, and then a step-down from 1 p.u to 0.75 p.u. It is noted that the torque of the DC machine is following the turbine torque curve along with different rotor speed, in order to emulate the characteristics of typical wind energy source. It can be seen from Fig.5.14 that the shoot-through duty-cycle is reduced according to the increasing rotor reference speed. The active power captured is presented in Fig.5.14 as well. This is consistent with the simulation results.

In Fig.5.15 and 5.16, the generator speed reference is assigned to 600 r/min. The steady-state generator terminal line-to-line voltage and stator current with unity power factor control and the $I_d=0$ control are shown in Fig.5.15 and 5.16, respectively. It can be observed from Fig.5.15 (a) that the generator current i_a is lagging the line voltage V_{ab} at

the generator terminal by around 30^0. This angle difference is fixed with the unity power factor control. Thus, from Fig.5.16 (a), the generator current i_a is just lagging the line voltage V_{ab} by around 10^0. This angle difference is changed along with the different power output, which can be explained by the theoretical analysis and simulation, depicted in the previous sections. From the spectrum and THD of stator current shown in Fig.5.15(b) and 5.16 (b), harmonic-elimination is achieved at the generator-side with both control methods and thereby the operating performance of generator can be improved, which is consistent with the simulation results.

The switches in the front-end rectifier are then always turned on and thereby the proposed topology is reconfigured to a diode front-end Z-Source inverter based generation system. The corresponding generator terminal voltage and current are shown in Fig.5.17. Low-order harmonics appeared in the stator current as shown in Fig.5.17 (a), and hence results in distorted generator voltage. Most importantly, the torque oscillations are significant compared with the proposed system with SVM method. The harmonic spectrum of the current is presented in Fig.5.17 (b) together with its THD.

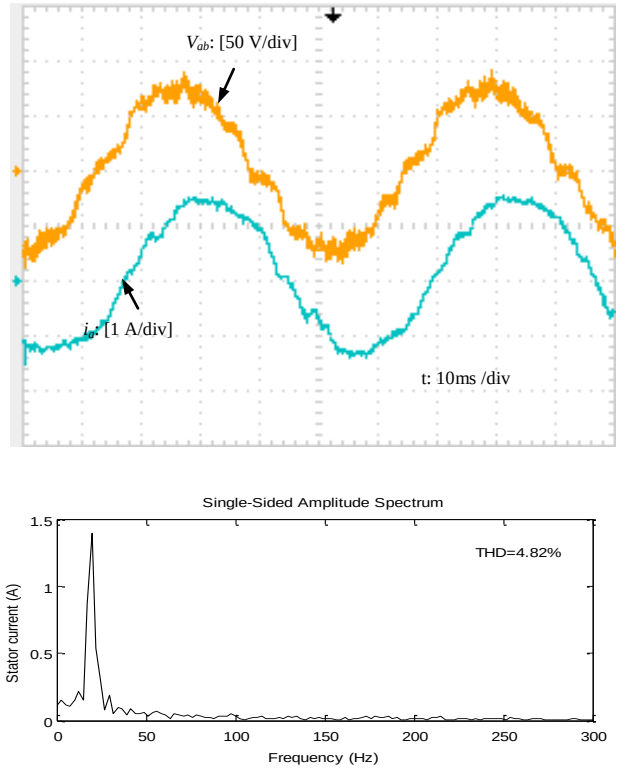

(a)

(b)

Fig.5.15 Steady-state experimental waveforms of voltage and current of PMSG with unity power factor method

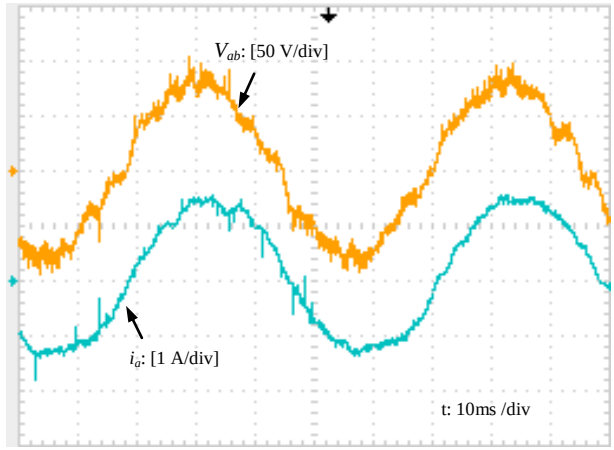

(a)

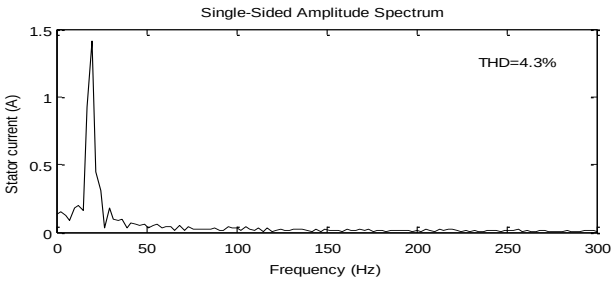

(b)

Fig.5.16 Steady-state experimental waveforms of voltage and current of PMSG with the Id=0 control

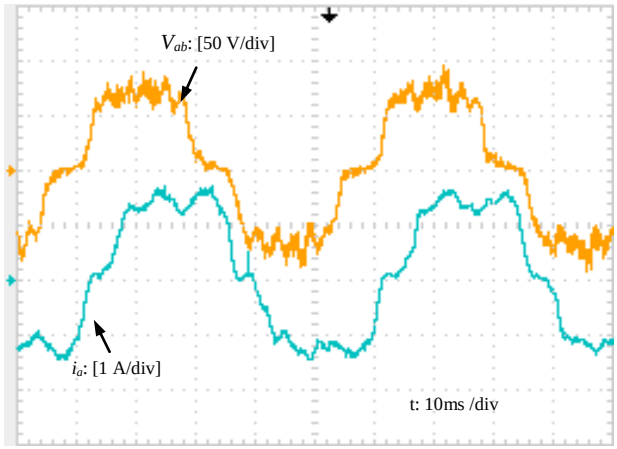

(a)

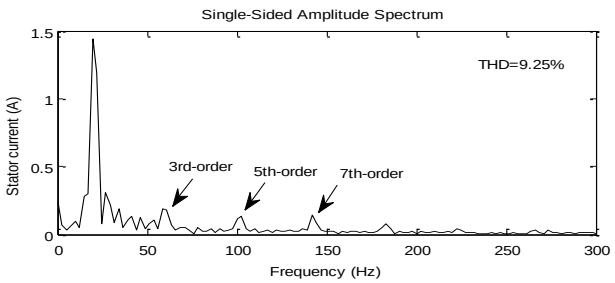

(b)

Fig.5.17 Experimental waveforms of voltage and current in the conventional diode front-end system.

In order to verify the reliable operation of the proposed system, a fault-ride-through experiment is illustrated in Fig.5.18. Initially, the proposed system is operating at the normal situation with the proposed control scheme. At a particular instant, the system senses a fault event, where any of the switches in the front-end rectifier is shorted and shoot-through occurred. With the control principle discussed in Chapter 4, the proposed system is immediately reconfigured into the diode-rectifier based system. It helps the system to sustain a certain tolerance time. The detailed voltage and current are shown in Fig.5.18, which illustrate the feasibility of the proposed configuration.

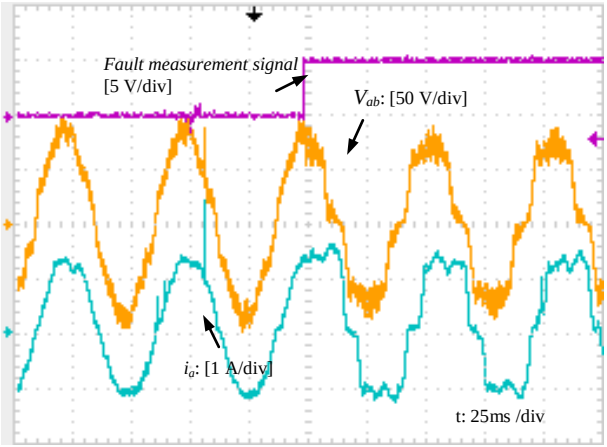

Fig.5.18 Experimental results of reliable operation of the proposed system.

5.5.3 Comparison of simulation and experimental results

It is valuable to compare the simulation and experimental results in terms of several performance parameters, such as power factor, THD, ripple on the DC link.

Section 5.2 has explained the optimal power factor control strategy, which consists of unity power factor control and $I_d=0$ control. From the comparison of simulation and experimental results, the performance of power factor control in the simulation is much better than that in the experiments. The phenomenon in THD comparison is also same. For instance, the input current THD of the proposed topology is 2.76% as illustrated in Fig.5.10, and thus the input current THD in the experiment is up to 4.8% as illustrated in Fig.5.15. This difference is because the numerical simulation consists of ideal operating conditions, such as the ideal components/devices, fast-enough control processor, real-time sampling without delay, and no measurement and calculation error and so on. However,

in the lab-based prototype, the power semiconductor switch, i.e., IGBT, is definitely not like the ideal switch used in the simulation. Normally the real switch has switching loss, reverse current, internal resistance and so on, and all of these non-ideal factors will affect the system performance.

5.5.4 Comparison with other topology

The comparison of Z-Source inverter and traditional inverters was investigated in [108] using cost, efficiency and passive components requirement as benchmarks. The Z-Source inverter exhibits a better performance than other topologies from the comparison results. Herein, the corresponding performance indices will be extended to evaluate the proposed converter and the back-to-back converter. First, the converter cost can be judged by the total average switching device power (SDP) and peak SDP [108], which are defined as follow,

$$(SDP)_{av} = \sum_{j=1}^{N} V_j I_{j,av} \text{ , and } (SDP)_{pk} = \sum_{j=1}^{N} V_j I_{j,pk} \tag{5.19}$$

Where, N is the number of switching devices, V_j is the peak voltage induced on the devices, and $I_{j,av}$ and $I_{j,pk}$ are the average and peak current through the devices, respectively. The total SDPs of both topologies are calculated, as shown in Table 5.2, based on the operating condition in Table 5.1. It can be seen from Table 5.2 that the total SDP of the back-to-back converter is much greater than that of the proposed converter in average and peak value, respectively.

On the other hand, the shoot-through problem, which is usually the main weak-link of the system reliability, does not exist in the proposed converter. Therefore, the developed topology is able to improve system reliability.

Table 5.2 Comparison between the back-to-back converter and the developed converter

Relationship	Items	Back-to-back converter	Developed converter
Total SDP	Number of switching device	12	9
	(SDP)av (kVA)	10.85	9.66
	(SDP)pk (kVA)	34.06	21.05

5.6 Conclusion

In this chapter, the design methodology, the simulation studies, and the experimental verification of an integrated generator-side buck-type rectifier and grid-side Z-Source inverter based PMSG wind generation system have been presented. The proposed generator-side control strategy was optimized from the fundamentals of the $I_d=0$ control and unity power factor method. The voltage-oriented control was adapted for the Z-Source inverter to decouple active and reactive power control while extracting the maximum wind power by adjusting the shoot-through duration of the Z-Source network. Compared with the traditional back-to-back converter, the shoot-through operation is allowed in the grid-side Z-source inverter and the reconfiguration of the generator-side converter is enabling the wind turbine to maintain the safety operation during faults of the power semiconductors in the generator-side converter. All the aforementioned characteristics are helpful to improve the reliability of the PMSG based wind turbine.

CHAPTER 6

STATISTICAL VOLTAGE QUALITY ASSESSMENT METHOD FOR GRIDS WITH WIND POWER GENERATION

6.1 Introduction

Regardless of DFIG or PMSG, wind power capacity will be meeting a significant percentage of the worldwide electricity demand in the next decade, especially in western European countries. Consequently, wind power will affect the operation of utility in terms of voltage regulation, frequency control and so on. Thus there is a need to devise reliable methods to accurately quantify the impacts so as to obtain the most appropriate and economical solution to mitigate the negative impacts. Hence, this chapter intends to develop a feasible voltage quality analysis for large wind power penetrated networks.

The method proposed in this chapter calculates the impact of wind power penetration on network voltage in a statistical manner: the wind power injection and the state of the connected grid are described in terms of probabilistic distributions. An index, termed the significant level of voltage deviation, is developed to quantify the level of the voltage variations. The index helps in identifying the most effective remedial actions in restoring voltage quality to an acceptable level. A case study is included to illustrate the relatively simple calculation involved.

6.2 Preliminary considerations

6.2.1 Network description

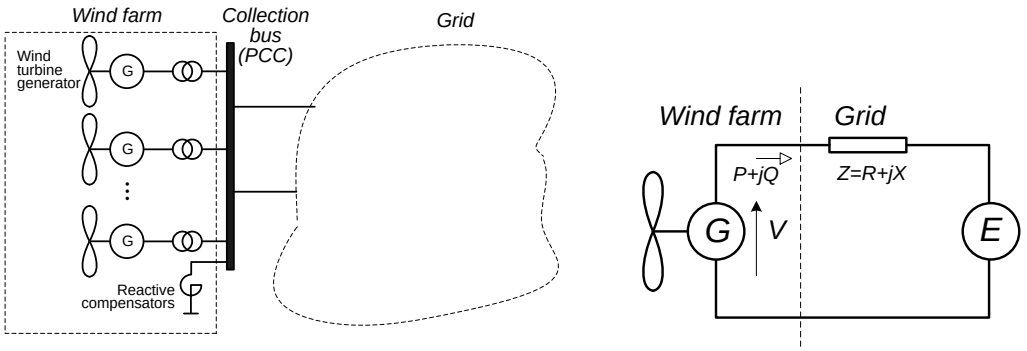

(a) (b)

Fig.6.1 Diagram of wind generation system

(a) Schematic of a grid-connected wind farm, (b) Equivalent circuit of the wind-farm-grid system

Figure 6.1(a) shows the schematic of a wind farm interconnected to a grid. All the wind turbine generators (WTG) are connected to a common node called the collection bus via distribution links. This bus is often treated as the point of common coupling (PCC) between the wind farm and the grid. When integrating a wind farm into the grid, the PCC would be the network node where specified technical conditions have to comply with the respective grid-code [109]. One such requirement governs the power factor at the PCC where for example, constant or variable power factor operational mode can be selected to operate wind farms, depending on the types of wind turbines used. For fixed-speed turbines, power factor control can be achieved by regulating the reactive power compensators which are connected to the PCC, and modern variable speed WTG can be speed-controlled to regulate the active and reactive power production [110]. Indeed, variable-speed wind turbine manufacturer can now offer different options for Var generation in steady state. Reference [111] presents two options of wind turbine reactive power output characteristic, which are constant power factor and variable power factor, respectively. Whether a wind farm operates under constant power factor mode or variable power factor mode, its active output power *P* and reactive power *Q* can be expressed as:

$$Q = k_p \cdot P \tag{6.1}$$

Where, $k_p = \sqrt{(1-\cos^2\phi)} \big/ \cos\phi$. $\cos\phi$ is the power factor of the wind farm output, *P* is the total real power output from the farm, and *Q* is the net reactive power output from

both the WTG and the wind farm reactive power compensator. It is worthy to mention that k_p has a fixed value under constant power factor operational mode of the wind farm, and would be variable under variable power factor mode.

From Fig. 6.1(a), the grid can be represented by its Thevenin equivalent circuit viewed from the PCC. In this representation, the voltage at the bus is denoted as *V*. The voltage source *E* equals to the no-load voltage at the bus. It can be readily shown that the equivalent Thevenin impedance $Z = R + jX$ (in p.u.) is governed by the short circuit ratio (ζ) and the *R/X* ratio (γ) at the PCC, as follows:

$$\begin{cases} R = \dfrac{E^2}{S_0 \times \xi} \times \dfrac{\gamma}{\sqrt{1+\gamma^2}} \\ X = \dfrac{E^2}{S_0 \times \xi} \times \dfrac{1}{\sqrt{1+\gamma^2}} \end{cases} \tag{6.2}$$

where S_0 is the rated power. Equation (6.2) is useful as very often, the terminal condition for the wind farm connection is expressed in terms of ζ and γ, instead of *Z*.

6.2.2 Impact on the PCC voltage

As soon as the wind farm begins to inject power *P* + j*Q* (at a particular power factor $\cos\phi$) into the grid, the voltage at the PCC will deviate from *E*. With respect to Fig.6.1(b), the voltage deviation can be expressed approximately as:

$$\Delta V = V - E = \frac{P \cdot R + Q \cdot X}{|V|} \tag{6.3}$$

Together with (6.1), (6.3) can then be rewritten as:

$$\Delta V = \frac{R + k_p \cdot X}{|V|} \cdot P \tag{6.4}$$

It can be seen from (6.4) that the voltage deviation ΔV is directly proportional to the wind farm output power P and the grid Thevenin equivalent R, X values. It should be emphasized that (6.4) only yields the steady-state value of the voltage variation, assuming over the interval of interest, no network control action has been initiated within the grid to vary Z or E.

The impact of the wind farm output power on the PCC voltage quality can be readily assessed via (6.4). Unfortunately, as will be described in greater detail in the next section, the WTG power output depends on the prevailing wind condition. As wind speed varies and when the wind farm operates under power factor control mode, the PCC voltage will vary in response to the fluctuating wind farm power production. Excessive voltage variations should not be allowed as it would lead to equipment damage. Allowable voltage variation applicable for wind farm operation has been prescribed in standards such as [87]. ΔV has to comply with the steady-state or long-term voltage deviation limit allowable in the respective standards.

For the problem in hand, an additional complication arises because the grid Thevenin impedance would also vary over the long-term. Clearly as network topology changes due to the switching in and out of network elements, upgrading and/or retiring of equipment, normal generation/load variations, these changes will inevitably lead to variations in ζ and γ and hence Z.

With the statistical and time-varying nature of P and Z taken into consideration, one needs to examine not only the degree of severity of the resulting voltage deviations but also the likelihood of their occurrence. An operating condition which leads to an unacceptable voltage variation at the PCC and which has a high probability of occurrence warrants closer design consideration than one which is seen to occur less often. With these points in mind and unlike the approaches described in [85, 86], a new statistical approach will be proposed in the next Section to analyze the voltage quality at the PCC.

6.3 Probabilistic analysis of PCC voltage deviation

As stated earlier, P relies on the availability of the wind and Z depends on the operating state of the network. Probabilistic analysis has been used to estimate wind farm output P

while statistical concept has been applied in [112] to analyze operating state of power system elements. The approach described in this section is an attempt to apply these techniques to obtain the probabilistic evaluation of ΔV at the PCC.

6.3.1 Probabilistic model of wind power generation

In the literature, Weibull distribution function has been widely used to statistically describe wind speed distribution [113]. The probability density function (pdf) of wind speed is given by:

$$f(v) = (\frac{k}{c})(\frac{v}{c})^{k-1} \exp[-(\frac{v}{c})^{k}] \tag{6.5}$$

where v is the wind speed, k is the shape coefficient and c is the scale coefficient. In handling wind speed data, it is convenient to sub-divide the continuous speed range into sub-sections or states and characterize the probability distribution of v in terms of these states. Hence from (6.5), one can express the probability distribution of v as a set of discrete data

$$F_v = \{v(l), F_v(l) : l = 0,1,\cdots, N\} \tag{6.6}$$

where N is the total number of the discrete wind speed states, and $v(l)$ is the discrete wind speed value over the speed range $\{v(l) - \varepsilon/2, v(l) + \varepsilon/2\}$, ε being the width of the speed range. Typically, $\varepsilon = 1\ m/s$. According to (6.5), the probability $F_v(l)$ of the discrete wind speed is then given by

$$F_v(l) = \int_{v(l)-\varepsilon/2}^{v(l)+\varepsilon/2} f(v)dv = \exp\{-[\frac{v(l) - \varepsilon/2}{c}]^k\} - \exp\{-[\frac{v(l) + \varepsilon/2}{c}]^k\} \tag{6.7}$$

An example of the discrete probability distribution of v is shown on Fig.6.2, with $\varepsilon = 1\ m/s$.

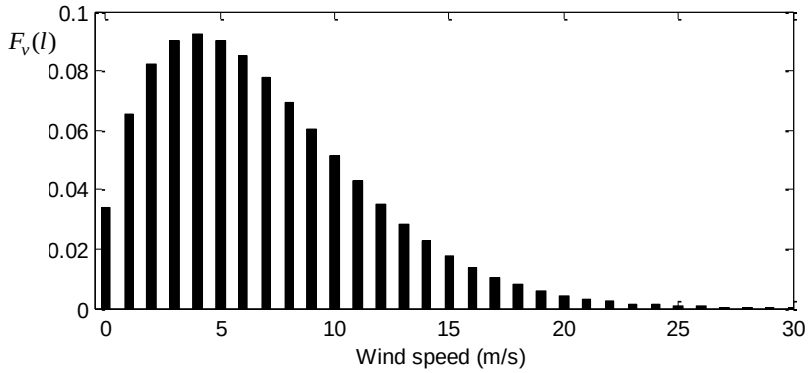

Fig.6.2 A typical discrete probability distribution of wind speed

From the discrete distribution data of wind speed, the next task is to relate it to the wind power produced, *P*. One could adopt the generic WTG model described in [4] where *P* is expressed in terms of wind speed *v* as

$$P=\begin{cases}0 & v\in[0,v_{in})\cup(v_{out},+\infty)\\ a+bv^3 & v\in[v_{in},v_r)\\ P_r & v\in[v_r,v_{out}]\end{cases} \tag{6.8}$$

where v_{in} is the cut-in wind speed, v_r the rated wind speed, v_{out} the cut-out wind speed and P_r is the rated real power capacity of the wind farm. The constant coefficients *a*, *b* are given by

$$a=\frac{P_r\cdot v_{in}^3}{v_{in}^3-v_r^3} \quad , \quad b=\frac{P_r}{v_r^3-v_{in}^3}$$

Equation (6.8) describes the 3 operating ranges of the WTG. When wind speed is below v_{in} or above v_{out}, no output power can be expected from the WTG. When the wind speed is between v_{in} and v_r, *P* varies to the cube of wind speed. Beyond v_r and at less than v_{out}, only rated power will be produced.

Since the wind speed distribution function has been discretized into the form of (6.6), and bearing in mind the three operating ranges of the WTG described by (6.8), one can obtain the discrete probability distribution of *P* as follows:

$$F_P(i)=\begin{cases}\{1-\exp[-(\frac{v_{in}}{c})^k]+\exp[-(\frac{v_{out}}{c})^k]\}\delta(P) & v(i)\in[0,v_{in})\cup(v_{out},+\infty)\\ \exp\{-[\frac{v(i)-\varepsilon/2}{c}]^k\}-\exp\{-[\frac{v(i)+\varepsilon/2}{c}]^k\} & v(i)\in[v_{in},v_r)\\ \{\exp[-(\frac{v_r}{c})^k]-\exp[-(\frac{v_{out}}{c})^k]\}\delta(P-P_r) & v(i)\in[v_r,v_{out}]\end{cases} \tag{6.9}$$

where $P(i)$ is the discrete state of the active power production at the discrete wind speed $v(i)$. $\delta(P)$ denotes the impulse function at *P*. Derivation of (6.9) is given in Appendix B.

In Fig. 6.3(a), the discrete wind speed distribution $F_v(l)$ is shown. The corresponding WTG output power *P* vs speed *v* curve is shown in Fig.6.3(b). The discrete probabilistic distribution of the wind power $F_P(i)$, as described by (6.9), is shown in Fig.6.3(c) where it is plotted against $P(i)$. Figure 6.3(c) can be described by the power discrete probability set

$$T_P=\{P(i),F_P(i):i=0,1\cdots,M\} \tag{6.10}$$

where *M* is the number of selected wind power states at which $P(i)$ is calculated using (6.8) and $F_P(i)$ is obtained from (6.9).

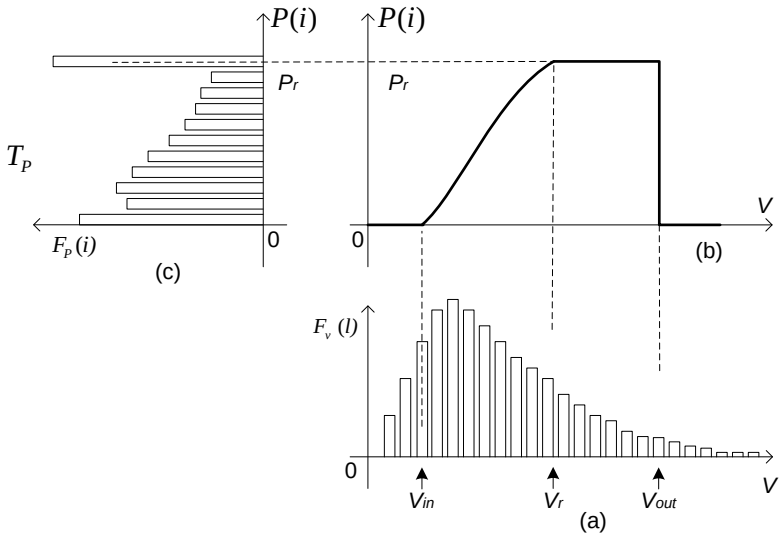

Fig.6.3 Probabilistic derivation

(a) Discrete probabilistic distribution of wind speed, (b) Wind-farm power vs wind speed characteristic, (c) Discrete probability distribution of wind power production

6.3.2 Grid Thevenin equivalent impedance probabilistic model

The grid is made up of numerous elements, including transmission lines, cables, transformers and generators. While it can be expected in most instances these equipment would be in service, it cannot be assumed that this will be so at all times. Consequently, when an element of the grid is taken out or put in service, it will result in changes in the fault level ζ, R/X ratio γ and hence impedance Z, when viewed from the PCC. Such impedance changes can be statistically related to the status of the grid. This is because utilities have excellent knowledge pertaining to the statistical likelihood of the service availability of individual major equipment in the grid, based on the operational statistical data collected over long time and experience. Hence, it is on this basis that the following approach is proposed to yield a probabilistic grid model.

Suppose there are n elements in the grid, the status of each of which is to be considered in the analysis. In practice, n would be much less than the actual number of elements in the grid. This is because as an element is electrically further from the PCC, its operational status will have lesser impact on the variation in Z. Hence remote elements need not be considered in the analysis.

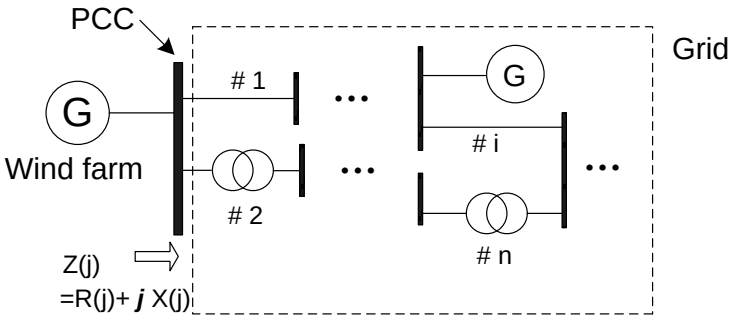

Fig.6.4 Network elements in grid

Next, define x_k, k = 1,2, …n as the operational state of each of the n elements shown in Fig.6.4. Each x_k can assume the value of 1 or 0: if the k^{th} element is in service, x_k has a value 1 and if the element is out of service, x_k has a 0 value.

Thus a system state vector x can be defined as $x = (x_1, x_2, \ldots, x_n)$. From the utility statistical data, suppose the corresponding availability and unavailability of each of the elements at

any given time are A_k and U_k respectively. One can then derive the discrete probability of the grid system state via the expression

$$F_Z(j) = \prod_{k=1}^{n} [x_k A_k + (1 - x_k) U_k] \tag{6.11}$$

where $j = 1, 2, \ldots, 2^n$ denotes the grid system state number associated with x. Each state corresponds to one of the 2^n grid configurations. For example, if one is interested in seeing how two elements in a grid is affecting Z, one only need to consider 2^2 or 4 states or network configurations. From (6.11), the probability $F_z(j)$ will consist of 4 elements: A_1A_2, A_1U_2, U_1A_2 and U_1U_2.

For each of the grid state ***j***, there is a corresponding Thevenin equivalent impedance, denoted as $Z(j)$. The determination of $Z(j)$ is straight-forward: one only has to use a conventional short-circuit analysis program to calculate ζ and γ at the PCC bus for the particular grid state, and then apply (6.2) to evaluate $Z(j)$.

The equivalent impedance $Z(j)$ and its associated probability $F_Z(j)$ can then be grouped to form the discrete probability set of impedance Z

$$T_Z = \left\{ Z(j), F_Z(j) : j = 1,2\cdots,2^n \right\} \tag{6.12}$$

6.3.3 Probabilistic voltage deviation

From (6.4), it is seen that the voltage deviation ΔV at the PCC can be calculated based on the wind power production P and the grid Thevenin impedance Z. Since P and Z have now been expressed in terms of probability sets (6.10) and (6.12), the statistical distribution of ΔV can be computed by recognizing the distribution of ΔV as a joint distribution between P and Z. The P and Z distributions are deemed to be independent.

Hence if wind power state ***i*** occurs, the corresponding probability distribution $F_P(i)$ can be obtained from (6.9), and if the grid configuration ***j*** also occurs, its probability distribution $F_z(j)$ can be inferred from (6.11). Hence from (6.4), ΔV resulting from the combined state ***i-j*** is given by:

$$\Delta V(i,j) = \frac{[R(j) + k_p \cdot X(j)]}{|V|} \cdot P(i) \equiv \psi(j) \cdot P(i) \tag{6.13}$$

The corresponding probability of occurrence of the state ***i-j*** is given by

$$F_V(\Delta V(i,j)) = F_P(i) \cdot F_Z(j) \tag{6.14}$$

Thus ΔV and its probability of occurrence can be evaluated using (6.13) and (6.14).

6.4 Significant level of voltage deviation

As explained in Section 6.2, various standards governing voltage quality are in place. The analysis of previous section shows that such voltage excursions are statistical in nature. It is now proposed an index called significant level of voltage deviation be used to quantify the extent of severity of voltage deviations, taking into consideration their likelihood of occurrence. Significant level concept has been used in various statistical studies [114]. In the context of the present study, the significance level of ΔV is denoted as α where

$$\alpha = prob(|\Delta V| > \delta) \tag{6.15}$$

As shown, the significant level α is defined as the probability when $|\Delta V|$ exceeds a pre-set limit δ: i.e. α is the cumulative probability of all the discrete voltage deviations occurring beyond the $|\Delta V|$ limit δ. The value of δ is selected from the relevant standards governing voltage deviation. Typically δ = 0.1 p.u. from [87]. Since (6.14) yields the probability of each of the discrete voltage deviations and the value of each ΔV can be readily evaluated using (6.13), thus all the discrete states of $|\Delta V|$ which exceeds δ can be extracted and their corresponding probabilities summated to provide the significant level measure α. Mathematically, the calculation of α can be expressed as:

$$\alpha = \sum_{|\Delta V(i,j)|>\delta} F_V(\Delta V(i,j)) = \sum_{|\Delta V(i,j)|>\delta} [F_P(i) \cdot F_Z(j)] \tag{6.16}$$

Stated in this context, the ideal grid-wind farm system design would be one with α = 0. In practice, however, a more realistic design objective would be to reduce α to an acceptable level. From (6.16), α is seen to be dependent on the distributions of wind power $F_P(i)$ and network Thevenin impedance $F_Z(j)$. Manipulation of network impedance $Z(j)$ can be

carried out by the grid operator. Hence in this paper, the objective is to examine the impact of adjusting Z on α.

To achieve this objective, the first step is to determine the extent of the contribution of each of the grid state ***j*** to α. The significance level α can be decomposed as

$$\alpha = \sum_{j=1}^{2^n} prob(|\Delta V| > \delta \,|\, Z(j)) \cdot prob(Z(j)) \tag{6.17}$$

Consider the grid state ***j*** which has the Thevenin equivalent impedance of $Z(j)$. At $Z(j)$ and from (6.11), the probability of its occurrence is $F_z(j)$ or prob($Z(j)$). The conditional probability term prob($|\Delta V| > \delta \,|\, Z(j)$) shown in (6.17) denotes the probability of $|\Delta V|$ exceeding the limit δ when the impedance is $Z(j)$. For this given $Z(j)$ and from (6.13), $\Delta V = \Psi(j)\, P(i)$. Hence the computation of prob($|\Delta V| > \delta \,|\, Z(j)$) can be transformed to

$$\begin{aligned} prob(|\Delta V| > \delta \,|\, Z(j)) &= prob(|\psi(j) P(i)| > \delta) \\ &= prob(P(i) > \delta / |\psi(j)|) \end{aligned} \tag{6.18}$$

Since $Z(j)$ is given, $\Psi(j)$ is also known. With a pre-set value for δ, one can obtain $\delta/|\Psi(j)|$. From (6.9), the cumulative probability for $P(i) > \delta/|\Psi(j)|$ can be evaluated. Hence, prob($|\Delta V| > \delta \,|\, Z(j)$) is obtained. By repeating the calculation for all $Z(j)$, one can therefore determine the probability of $|\Delta V|$ exceeding the voltage limit δ for all the grid states ***j***.

A very useful result can now be derived by applying Bayes' theorem, i.e.

$$prob(Z(j) \,|\, |\Delta V| > \delta) = \frac{prob(|\Delta V| > \delta \,|\, Z(j)) \cdot prob(Z(j))}{\Pr ob(|\Delta V| > \delta)} \tag{6.19}$$

Substituting (7.15) into (7.19), (7.19) can be rewritten as:

$$prob(Z(j) \,|\, |\Delta V| > \delta) = \frac{prob(|\Delta V| > \delta \,|\, Z(j)) \cdot prob(Z(j))}{\alpha} \tag{6.20}$$

Equation (6.20) quantifies the individual contribution of grid state ***j*** toward the significance level α. Therefore it is now possible to calculate the contribution of state ***j*** to α since all the terms on the right hand side of (6.20) are known. From all the states ***j*** which contribute toward voltage deviation exceeding the level δ, one can screen out those

network scenarios or states which have higher probability of occurrence. Remedial actions to be taken on these states will be effective ways to enhance the voltage quality at the PCC. Numerical examples in the next section will illustrate this design strategy.

6.5 Case study

An example of a grid with wind power generation is used in this case study to illustrate the proposed statistical method. Its single-line diagram is shown in Fig.6.5 and its details can be found in [115]. In the studied network, Bus 112 is the collection bus of a wind farm. The farm is assumed to be inter-connected to Bus 111 via an under-sea transmission cable. Thus Bus 111 is considered as the PCC. Hence, the focus of the study will be the voltage quality at the PCC.

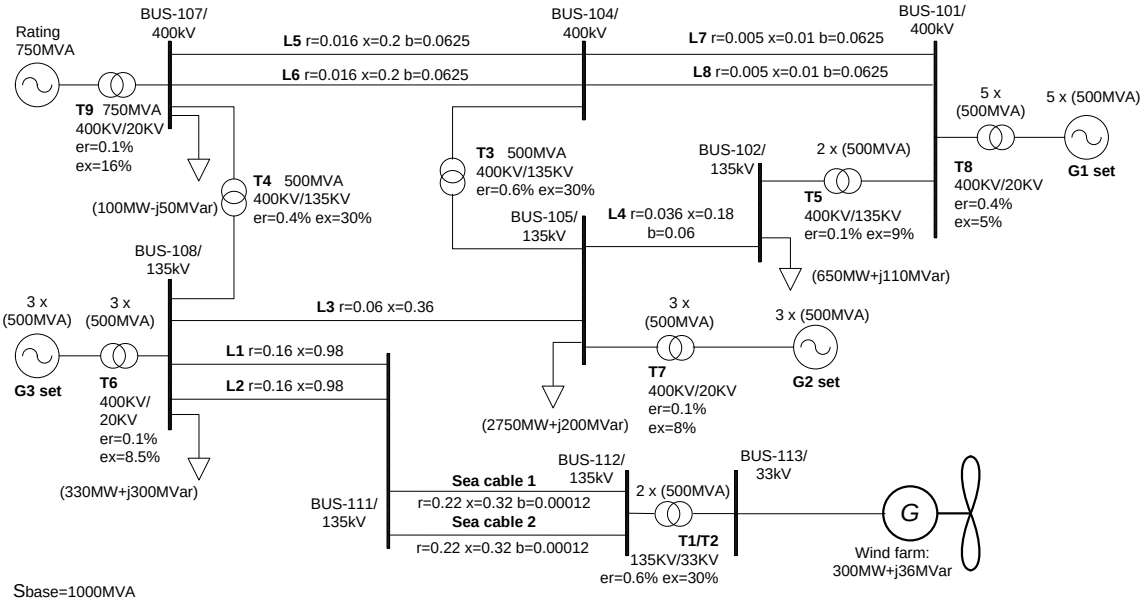

Fig.6.5 The base-case network model used in the study

The data from [115] is used for this case study, whereby the total load in the network is 3730 MW, of which the wind farm contributes 300 MW. The base case shows that 36 MVAr (k_p = 0.12) of capacitive reactive power is also needed at the PCC in order to achieve satisfactory voltage profile in the vicinity of the wind farm. Also included in the

diagram are the p.u. impedance values of the various plant elements and the power levels of the various generators and loads. The parameters of sea cable are from [116].

6.5.1 Wind power distribution

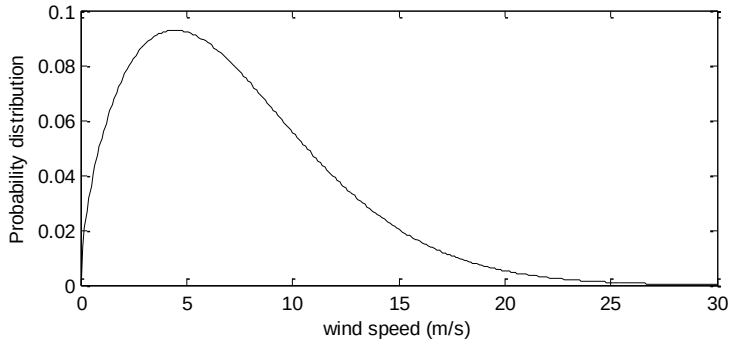

(a)

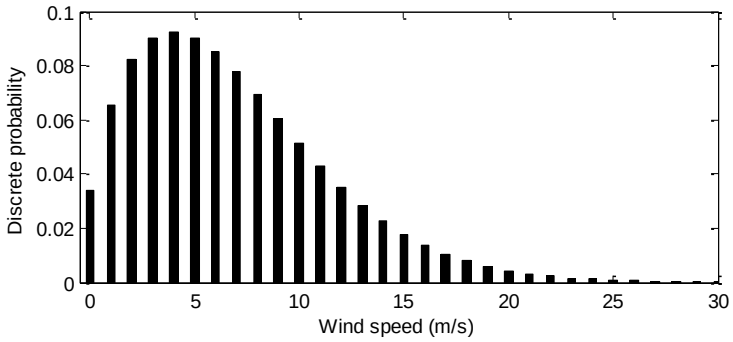

(b)

Fig.6.6 Wind speed probability distribution

(a) Weibull function with k = 1.6 and c = 8.2, (b) Discrete wind speed distribution F_v

Based on two years' wind data obtained from [117], the Weibull distribution curve with k = 1.6 and c = 8.2 is included to describe the wind speed probability distribution function shown in Fig.7.6(a). The WTG data was taken from [118]. Each WTG is rated 3 MW. Therefore the wind farm is expected to contain at least 100 WTG. Also for this type of WTG, the cut-in speed of 4 m/s also means that the WTG will only be operational when the wind speed exceeds 4 m/s, a range the Weibull curve shown in Fig.6.6(a) has represented well. The cut-out speed and nominal speed for this WTG is 25 m/s and 15 m/s respectively. Based on the WTG data and the wind speed distribution shown in Fig.6.6(b), wind power production in the wind farm can be calculated using (6.8) for the rated power

(P_r) of 300 MW. The corresponding probabilistic distribution of P is depicted in Fig.6.7, which is the graphical description of (6.9).

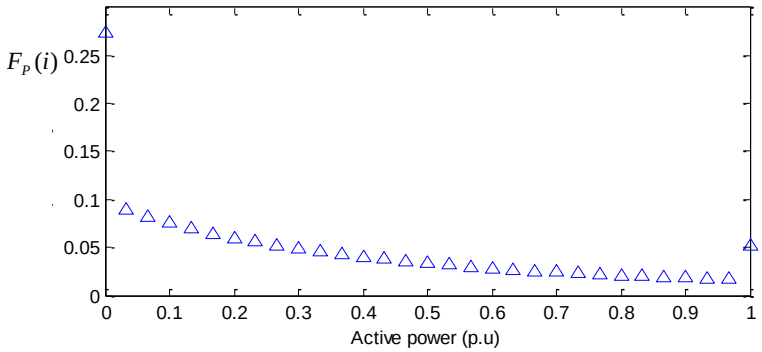

Fig.6.7 Discrete probability distribution of wind power: rated power 300MW

6.5.2 Grid Thevenin impedance

Component reliability data of the various elements of the grid system is required in order to derive the plant availability/unavailability information. It is assumed the data shown in Table 6.1 taken from [112] is applicable in the present study. Unavailability of element(s) results in altered network configurations/topologies from that shown in the example study. The probability of the particular grid configuration or state can then be calculated based on the data given in Table 6.1. For each grid state, the individual impedance at the PCC has been determined using a short-circuit study program. With this information and applying (6.2), the Thevenin impedance Z at the PCC is obtained. The results are summarized in Table 6.2. Grid states with probability of less than $7x10^{-5}$ have been ignored as it is considered that these states have too small a probability of occurrence to be of concern.

Table 6.1 Component Reliability Data

Component	**λ (failures/yr)**	**Repair Time(hr)**
Generator unit	2	198
Overhead line	0.02/km	10
Transformer	0.01	200

Table 6.2 Thevenin Impedance of Grid at Various States and the Associated Probability (Base MVA = 1000)

State *j*	**Element of grid outage**	$Z(j)$ (ohm)	$F_Z(j)$
1	None	2.739+j17.134	0.611445
2	One of G1	2.804+j17.506	0.138202
3	One of G2	3.805+j23.329	0.083401
4	One of G3	3.843+j23.260	0.083401
5	Two of G1	3.449+j21.416	0.012495
6	Two of G2	4.108+j24.472	0.003748
7	Two of G3	4.395+j27.880	0.003748
8	T8	2.804+j17.506	0.000697
9	Three of G1	3.800+j23.394	0.000565
10	T7	3.804+j23.329	0.000419
11	T6	3.843+j23.260	0.000419
12	L4	3.75+j23.332	0.000419
13	T5	3.583+j22.339	0.000279
14	L1 or L2	5.628+j34.904	0.000209
15	L5 or L6	3.415+j21.402	0.000139
16	T1 or T2	2.739+j17.134	0.000139
17	L7 or L8	3.414+j21.381	0.000070
18	L3	3.526+j23.833	0.000070
19	Simultaneous multiple elements outage (L5 and L6)	Probability less than 0.000070 - case ignored	

6.5.3 Voltage deviations probability

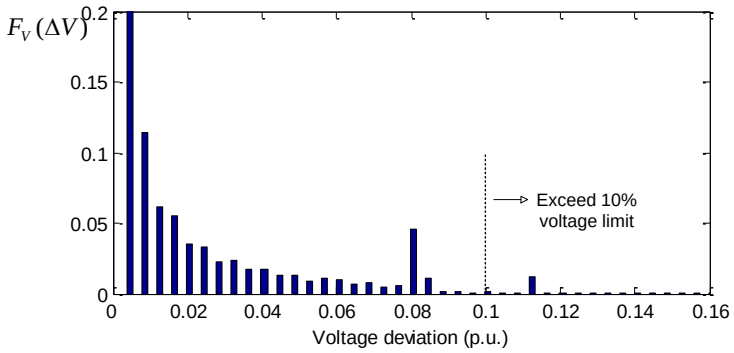

Fig.6.8 Probabilistic distribution of ΔV

Once the probability distributions of wind power P and the grid impedance Z have been determined, the probabilistic distribution of ΔV can be evaluated using the procedure described in Sections 6.3.3 and 6.4. **Figure** 6.8 shows the probabilistic distribution of ΔV at the PCC. Following the guidelines given in [119], the steady-state voltage at the bus must be controlled to within 10% of its nominal value. Therefore, the voltage limit δ is set as 0.1. From the discrete distributions F_p given in Fig.6.7 and F_z in Table 6.2, the significant level α for $|\Delta V| > 0.1$ can be calculated. In this instance, $\alpha = 0.01396$ which indicates that for 1.396% of the time, $|\Delta V|$ at the PCC can be expected to exceed the 10% threshold.

Next, it is interesting to explore, of the expected 1.396%, the contribution of each grid state toward α. One makes use of (6.20). In this case, to calculate prob ($Z(j) \mid |\Delta V| > 0.1$)), one needs to evaluate the term prob ($|\Delta V| > 0.1 \mid Z(j)$). Take grid state $\boldsymbol{j} = 2$ in Table 6.2 as an example. The corresponding impedance is $Z(2) = 2.804 + j\ 17.506$ ohm. Then, from (6.13),

$$\Delta V(i,2) = \frac{2.804 + k_p \cdot 17.506}{|V|} \cdot P(i) \tag{6.21}$$

For this grid state, (6.21) shows that the probability distribution of ΔV depends on the probability of wind power distribution $P(i)$ which is shown in Fig.6.7. Accordingly and from (6.21), calculate $\Delta V(i,2)$ for each $P(i)$, extract only those cases with $|\Delta V(i,2)| > 0.1$ and the corresponding probability of $P(i)$ from Fig.6.7. The sum of all the probabilities of such $P(i)$ cases is the contribution of grid state 2 toward α.

The contribution of other grid states ***j*** to α can be calculated in the same manner described earlier. The results are presented in Table 6.3. The table only includes those states which can result in $|\Delta V| > 0.1$. From Table 6.3, it is obvious states ***j*** = 3 and 4 are the two main contributing states to α. Other grid states ***j*** either have much lower probability or there is no incident of $|\Delta V| > 0.1$ for these grid states.

To verify the accuracy of the ΔV calculation used in the proposed method, a series of conventional load-flow study have also been carried out to calculate ΔV at the PCC for each of the grid states shown in Table 6.2, at the maximum wind farm output of 300MW. Table 6.4 compares the voltage deviation ΔV calculated by the proposed method and the conventional low flow study. Only those grid state(s) which contribute to $\Delta V > 10\%$ have been shown in Table 6.4.

Table 6.3 Grid States and Probability when $|\Delta V| > 0.1$

Grid State *j*	**Element(s) of Plant Outage**	$prob(Z(j) \mid\mid \Delta V \mid > 10\%)$
3	One of G2 set	0.439108
4	One of G3 set	0.499100
6	Two of G2 set	0.022422
7	Two of G3 set	0.025452
9	Three of G1 set	0.003178
10	T7	0.002356
11	T6	0.002357
12	L4	0.002286
13	T5	0.001433
14	L1 or L2	0.001927
18	L3	0.000371

Table 6.4 Comparison of voltage deviation ΔV obtained from the conventional load flow study and from the proposed probabilistic method

Grid State *j*	**Element(s) of Plant Outage**	**Voltage deviation** ΔV *(%)*	
		Conventional load flow study	**Proposed statistical method**
3	One of G2 set	11.160	10.87
4	One of G3 set	10.106	10.923
6	Two of G2 set	12.471	11.595
7	Two of G3 set	12.992	12.742
9	Three of G1 set	10.060	10.871
10	T7	11.160	10.87
11	T6	10.106	10.922
12	L4	10.871	10.782
13	T5	10.543	10.311
14	L1 or L2	16.761	17.775
18	L3	10.332	10.512

From Table 6.4, it can be seen that the differences between ΔV obtained from the much simpler Thevenin equivalent model used in this analysis and that obtained from the conventional load flow study are less than 8% which are considered acceptable. More importantly, it is pleasing to note that the load flow studies confirm all the grid states identified by the present approach and shown in Table 6.3 do indeed result in $|\Delta V|$ exceeding the 10% limit. Furthermore, the computational time of the proposed method is much shorter than that of the conventional load flow study. For instance, the computational times required for calculating grid state 3 in Table 6.4 are 9.6s and 0.5s for the conventional load flow and the proposed statistical method respectively. These simulations were carried out using a P4 2.13-GHz/1-GB RAM PC. Therefore, the proposed statistical approach using the simplified network model is able to provide a quick way to identify those grid states which would result in voltage quality violations.

6.5.4 Screening network states

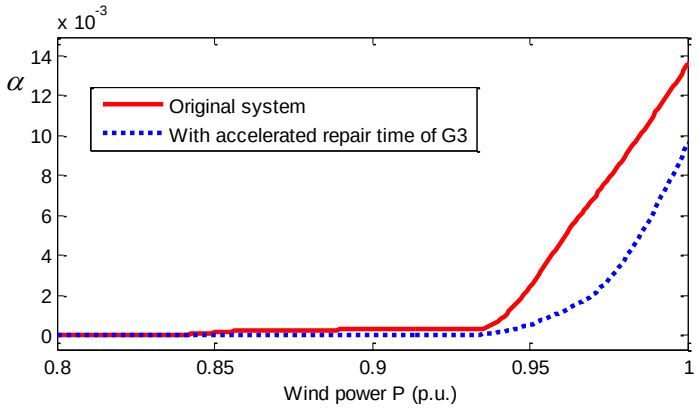

Fig.6.9 Significant level α vs P: with and without accelerated G3 repair

The results shown in Table 6.3 are very useful because they can help identify effective grid upgrade/re-enforcement strategies to enhance grid voltage quality. For example, Table 6.3 shows that since grid state 4 has contributed most significantly toward the cumulative probability α, state 4 is an obvious candidate worthy for closer examination. State 4 pertains to the outage of one unit of G3. Suppose one were to examine the impact of reducing the G3 unit repair or down-time from the assumed value of 198 hours given in Table 6.1 to 50 hours. One can re-calculate the significant level and the results are included in Fig.6.9. The outcome of such a study is promising: it indicates that by reducing the G3 unit repair time, α or the cumulative probability of $|\Delta V| > 0.1$ p.u. is 0.96% for the wind power output up to its rated value of 300 MW. This is a much reduced probability, compared to the 1.396% level obtained without the reduction in G3 repair time.

The reduction in G3 repair time is suggested here as one possible way to increase wind power contribution while taking into consideration its impact on voltage quality. Clearly there are other grid reinforcement possibilities and these have to be evaluated with respect to its technical as well as economic viability. What is significant from the present approach is that it allows one to screen out those grid states which would result in higher probability of the voltage limit being exceeded. The method identifies these grid states so that effective network remedial actions can be used to allow increased wind power penetration while acceptable voltage quality performance at the PCC can be realized.

6.5.5 Additional comparison with other Methods

Although voltage quality can be investigated using the conventional load flow study, the likelihood of the network voltage quantities assuming particular states is not predicted since the load flow study is a deterministic method. A more appropriate comparison would be based on the probabilistic load flow (PLF) method [92, 93], in which one can evaluate probability issues and statistical moments of all state variables and output network quantities to indicate the possible ranges of load flow, instead of obtaining a point estimate result from the conventional load flow.

Alternatively, Monte Carlo simulation (MCS) can be used to solve the PLF problem by repeated simulations. MSC [120] has been widely used in power system computations, especially in reliability assessment. It can provide considerably accurate results, but the computation is time-consuming. In the present investigation, the technique that combine MCS with multi-linearized power flow equations described in [121] has been adapted in order to reduce the computational burden. Specifically, MCS is utilized to generate random wind speed in order to obtain realistic wind power distribution. The wind power then forms the input to the load flow study of the studied network. This approach provides a simplified and yet effective technique to investigate voltage quality violations. Results obtained by MCS are set as benchmarks for comparing against the proposed statistical method.

Table 6.5 Computational Time Comparison

Methods	**Computational Time (s)**
Monte Carlo Simulation (10000 trials)	*77.06*
Monte Carlo Simulation (20000 trials)	*156.89*
Proposed method	*1.63*

The proposed statistical method and the MCS method are implemented by using MATLAB M-language. The methods are tested using the same 2.13-GHz PC mentioned earlier. The average computation times based on the combined MCS-multi-linearized power flow equations with different trials have been tracked. The computational times are compared with that using the proposed statistical method, as shown in Table 6.5. From

Table 6.5, it is seen that the MCS requires some 77 s on the PC in order to generate 10000 trials and provides the estimated probability density distribution of wind speed and power. And the computational burden would be even larger if more trials are required. The computational time is at least some 50 times less using the proposed statistical method, as is clearly shown in the table.

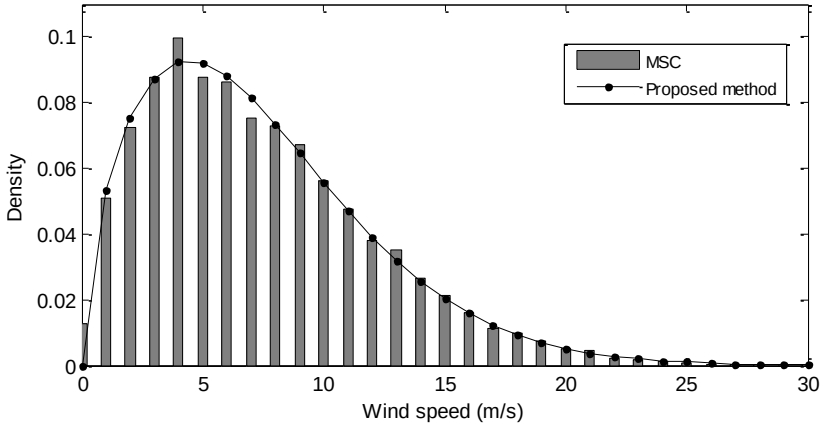

Fig.6.10 Comparison between the probability density distribution of wind speed obtained from MCS and proposed method

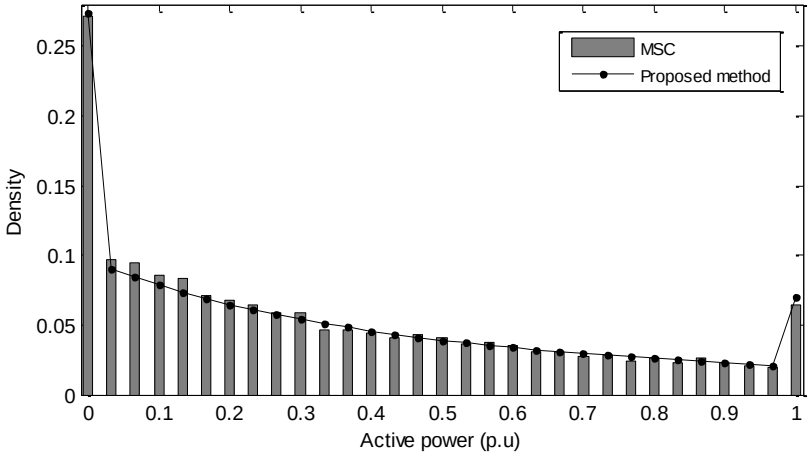

Fig.6.11 Comparison between the probability density distribution of wind power obtained from MCS and proposed method

Next, Figure 6.10 and 6.11 compare the probability density curves obtained by the MCS (based on 10000 trials) and the proposed statistical method. From Fig. 6.10, it is seen that the wind speed distributions obtained from the two methods agree well. Differences in some local part of the distributions occur and these deviations are mainly caused by linear approximations. Again, it can also be seen from Fig. 6.11 that the probability density

distributions of wind power obtained by the proposed method are in reasonable agreement with those obtained by the MCS. This is most encouraging as the proposed probabilistic method is an efficient computational technique to assess voltage quality in wind farm-grid connected system, in terms of its simple arithmetic operation, while it can still provide good estimates of voltage deviations and their likelihood of occurrence.

6.6 Conclusion

In this chapter, a statistics-based analysis method has been proposed for the purpose of assessing the impact on voltage quality caused by wind power generation. Voltage deviation has been computed using the probabilistic models of wind power production and grid Thevenin impedance. An index called significance level of the voltage deviation α has been developed to provide a probabilistic measure of the voltage quality performance. By considering the contributing factor from each of the grid states that constitute α, possible solution methods to improve on voltage quality can be obtained. This will lead to a corresponding increase in the wind power penetration level that can be accommodated in the grid, with acceptable voltage quality at the PCC. A case study example is included in this chapter to illustrate the effectiveness of the proposed method.

CHAPTER 7

CONCLUSIONS AND RECOMMENDATIONS

7.1 Conclusions

This thesis has documented the investigation of the grid integration issues for wind based renewable energy conversion system in terms of architecture, control and analysis. The research includes a review of current wind market development, the advance of wind turbine technology and grid regulations for wind power penetration; Modeling of DFIG wind generation system and the potential ride-through enhancement solution; Modulation of an integration of three-switch buck-type rectifier and Z-Source inverter and its application for PMSG based wind turbine; and statistics-based voltage assessment method for large wind power penetration.

A strong increase of worldwide wind capacity is expected in the next decade. The turbine configurations have been reviewed in terms of different generators and the main grid connection demands has been reviewed in terms of safety operation of transmission systems. All these investigations are intended to clarify the potential challenges of modern wind turbines and thus provided a guide to define research objectives in this thesis. In fact, with the increase of wind power penetration into utility, it is desired to design a grid compatible wind turbine, which is able to improve turbine operating performance and eliminate negative impacts on the network, such as fault ride-through capability, flexible voltage regulation and power quality issue.

DFIG based wind turbine has been adopted by many turbine manufacturers due to the low cost of its partial-scale power converter. However, enhancing ride-through capability under grid fault events has been worldwide recognized as a challenging problem of the DFIG wind generation systems. Hence, a potential ride-through solution, which is inspired by power quality improvement devices, i.e., series compensation, has been proposed in this thesis. The compensator is in series with the stator windings of DFIG in order to eliminate the effect of grid voltage faults. The essential behavior of DFIG during

faults has been analyzed via phasor diagram. Then an improved ride-through control scheme based on the ramp-function injection voltage has been developed to significantly reduce the energy capacity of the series compensator, which in turn reduce the capital cost. The performance of the designed architecture has been verified in simulation.

Compared with DFIG, the PMSG based wind turbine has better grid integration performance since full-scale power electronics converter is utilized. The power electronics are enabling wind turbines to have better dynamic response, faster fault monition, and quicker reaction operation. Thus it is recognized that power electronics play an important role in modern wind turbine. Hence, in this thesis, the integration of a three-switch buck-type rectifier and a Z-Source inverter has been developed to design a reliable power architecture for PMSG based turbine. The detailed modulation and operating principle of this topology were discussed and thereby the modulation scheme has been verified by both simulation studies and experimental results.

Subsequently, the design methodology, the simulation studies, and the experimental verification of the aforementioned architecture for PMSG application have been presented. The proposed generator-side control strategy is optimized from the fundamentals of the $I_d=0$ control and the unity power factor method. The voltage-oriented control is adapted for the Z-Source inverter to decouple active and reactive power control while extracting the maximum wind power by adjusting the shoot-through duration of the Z-Source network. The detailed numerical simulation and experimental results have verified the proposed control schemes.

With the increasing wind power penetration into grid utility, voltage quality analysis is becoming one of the important issues. In this thesis, a statistics-based analysis method has been proposed for the purpose of assessing the impact on voltage quality caused by wind power generation. Voltage deviation has been computed using the probabilistic models of wind power production and grid Thevenin impedance. An index called significance level of the voltage deviation α has been developed to provide a probabilistic measure of the voltage quality performance. By considering the contributing factor from each of the grid states that constitute α, possible solution methods to improve on voltage quality can be obtained. This would lead to a corresponding increase in the wind power penetration level

that can be accommodated in the grid, with acceptable voltage quality at the PCC. A case study example has been included to illustrate the effectiveness of the proposed method.

7.2 Recommendations

Based on the contributions of the completed project, further researches are recommended in following areas.

1. Energy storage control scheme for smoothing wind power

When renewable energy penetration reaches sufficiently high levels (around 20%–30% of total capacity), the intermittent nature of renewable source such as wind power, can begin to have noticeable negative effects on the entire grid. To meet this potential challenge, the utility has the right to curtail wind energy in order to avoid any violation of the system constraints.

The integration of energy storage systems (ESSs) with renewable energy resources has become one of the most viable solutions for facilitating increased penetration of renewable energy. Further studies for allocating an ESS in a distribution system with a high penetration of wind energy are suggested. The ultimate objective is to maximize the benefits for both the wind power plant and the utility by sizing the ESSs to accommodate all amounts of excess wind energy and by then allocating it within the system in order to minimize the annual cost of the electricity.

2. Scaled-up implementation of ride-through enhancement for DFIG system

The proposed control algorithm for ride-through enhancement for DFIG system can be scaled up to be implemented for a MW power level DFIG wind turbine in order to demonstrate the effectiveness and practicality for industry application. One design issue that needs to be considered is that the selection of power rating of rotor-side converter should be large enough so as to guarantee the safety operation of the converter during the demonstration of fault conditions. Then real-time monitoring of grid voltage fault would be one of the challenges in the experiment, which affects the start and end of the series compensation duration.

3. Ride-through enhancement of PMSG based wind turbine

PMSG based wind turbine is expected to have a large market share in the next decade. The ride-through problem of PMSG is easier to solve than that of DFIG since it has a full scale power converter. However, the rated power of PMSG is up to 5MW, which presents a high requirement for crowbar circuits in terms of cooling facilities and maintenance. One potential way is to merge energy storage system into the turbine. The flywheel energy storage system is a good alternative since it has fast charging and discharging characteristics for absorbing and supplying energy during fault transients.

4. Statistics-based analysis method for the purpose of assessing frequency control

With the large wind power penetration into grid utility, active power and frequency control is also one of the important issues. In this thesis, a statistics-based analysis method has been proposed for the purpose of assessing the impact on voltage quality. Further studies of frequency control are suggested to carry out via statistical methods. Frequency regulation can be computed using the probabilistic models of wind power production and system loads. An index called significance level can be also developed to provide a probabilistic measure of the frequency control performance. The corresponding case study is recommended using a practical micro grid simulator for simplification.

AUTHOR'S PUBLICATIONS

1. **S. Zhang**, K. J. Tseng, Vilathgamuwa D.M., and Nguyen T.D., "Design of a Robust Grid Interface System for PMSG-based Wind Turbine Generators," IEEE Transactions on Industrial Electronics, vol. 58, no. 1, pp. 316-328, 2011.

2. **S. Zhang**, K. J. Tseng, and S. S. Choi, "Statistical voltage quality assessment method for grids with wind power generation," Renewable Power Generation, IET, vol. 4, no. 1, pp. 43-54, 2010.

3. **S. Zhang**, K. J. Tseng, and et al, "Advanced Control of Series Voltage Compensation to Enhance Wind Turbine Ride-through," IEEE Transactions on Power Electronics, **to** be appeared (Early access), 2011.

4. T. D. Nguyen, K. J. Tseng, **S. Zhang**, and H. T. Nguyen, "A Novel Axial Flux Permanent Magnet Machine for Flywheel Energy Storage System: Design and Analysis," IEEE Transactions on Industrial Electronics, vol. 58, no. 9, pp. 3784-3794, 2011.

5. **S. Zhang**, K. J. Tseng, and T. D. Nguyen, "Novel three-phase AC-AC Z-Source converters using matrix converter theory," in Energy Conversion Congress and Exposition, 2009. ECCE 2009. IEEE, 2009, pp. 3063-3070.

6. **S. Zhang**, K. J. Tseng, and T. D. Nguyen, "Modeling of AC-AC matrix converter for wind energy conversion system," in Industrial Electronics and Applications, 2009. ICIEA 2009. 4th IEEE Conference on, 2009, pp. 184-191.

7. **S. Zhan**g, K. J. Tseng, and T. D. Nguyen, "WRIG based wind conversion system excited by matrix converter with current control strategy," in Sustainable Energy Technologies, 2008. ICSET 2008. IEEE International Conference on, 2008, pp. 203-208.

8. **S. Zhang** and K. J. Tseng, "Modeling, Simulation and Analysis of Conducted Common-Mode EMI in Matrix Converters for Wind Turbine Generators," in 2008

13th International Power Electronics and Motion Control Conference, Vols 1-5, 2008, pp. 2516-2523.

9. T.D. Nguyen, K.J. Tseng, **S. Zhang**, H.T.Nguyen. (2010). "On The Modeling and Control of a Novel Flywheel Energy Storage System". IEEE International Symposium on Industrial Electronics (ISIE) (pp. 214-219)Bari, Italy.

10. T. D. Nguyen, K. J. Tseng, and **S. Zhang**, "Position Sensorless Control of a Novel Flywheel Energy Storage System, " IPEC 2010, Singapore, pp. 1192 - 1198.

11. T. D. Nguyen, K. J. Tseng, and **S. Zhang**, "Model Predictive Control of a Novel Axial Flux Permanent Magnet Machine for Flywheel Energy Storage System," IPEC 2010, Singapore, pp. 519 - 524.

12. T. D. Nguyen, K. J. Tseng, **S. Zhang**, and C. Zhang, "A flywheel cell for energy storage system," in Sustainable Energy Technologies, 2008. ICSET 2008. IEEE International Conference on, 2008, pp. 214-219.

BIBLIOGRAPHY

[1] A. D. Hansen and L. H. Hansen, "Wind turbine concept market penetration over 10 years (1995-2004)," *Wind Energy*, vol. 10, no. 1, pp. 81-87, 2007.

[2] "http://www.awea.org/," *American wind energy association*.

[3] J. A. P. Lopes, N. Hatziargyriou, J. Mutale, P. Djapic, and N. Jenkins, "Integrating distributed generation into electric power systems: A review of drivers, challenges and opportunities," *Electric Power Systems Research*, vol. 77, no. 9, pp. 1189-1203, Jul 2007.

[4] T. Ackermann, *Wind power in power systems*: Hoboken, NJ: John Wiley & Sons, 2005.

[5] R. Doherty, E. Denny, and M. O'Malley, "System operation with a significant wind power penetration," in *Power Engineering Society General Meeting, 2004. IEEE*, 2004, pp. 1002-1007 Vol.1.

[6] M. Altin, O. Goksu, R. Teodorescu, P. Rodriguez, B.-B. Jensen, and L. Helle, "Overview of recent grid codes for wind power integration," in *Optimization of Electrical and Electronic Equipment (OPTIM), 2010 12th International Conference on*, pp. 1152-1160.

[7] J. M. Carrasco, L. G. Franquelo, J. T. Bialasiewicz, E. Galvan, R. C. PortilloGuisado, M. A. M. Prats, J. I. Leon, and N. Moreno-Alfonso, "Power-Electronic Systems for the Grid Integration of Renewable Energy Sources: A Survey," *Industrial Electronics, IEEE Transactions on*, vol. 53, no. 4, pp. 1002-1016, 2006.

[8] F. Blaabjerg and Z. Chen, *Power electronics for modern wind turbines*: Morgan & Claypool Publishers, 2006.

[9] J. M. Carrasco, L. G. Franquelo, J. T. Bialasiewicz, E. Galvan, R. C. P. Guisado, M. A. M. Prats, J. I. Leon, and N. Moreno-Alfonso, "Power-Electronic Systems for the Grid Integration of Renewable Energy Sources: A Survey," *IEEE Transactions on Industrial Electronics*, vol. 53, no. 4, pp. 1002-1016, 2006.

[10] H. Li and Z. Chen, "Overview of different wind generator systems and their comparisons," *Renewable Power Generation, IET*, vol. 2, no. 2, pp. 123-138, 2008.

[11] I. Erlich, W. Winter, and A. Dittrich, "Advanced Grid Requirements for the Integration of Wind Turbines into the German Transmission System," *Power Engineering Society General Meeting*, pp. 18-22, 2006.

[12] T. Burton, N. Jenkins, D. Sharpe, and E. Bossanyi, *Wind Energy Handbook*: John Wiley & Sons, 2011.

[13] *World wind energy association*. Available: http://www.wwindea.org/home/images/stories/worldwindenergyreport2009_s.pdf

[14] J. A. Baroudi, V. Dinavahi, and A. M. Knight, "A review of power converter topologies for wind generators," *Renewable Energy*, vol. 32, no. 14, pp. 2369-2385, Nov 2007.

[15] L. H. Hansen, P. H. Madsen, F. Blaabjerg, H. C. A. C. H. C. Christensen, U. A. L. U. Lindhard, and K. A. E. K. Eskildsen, "Generators and power electronics technology for wind turbines," in *Industrial Electronics Society, 2001. IECON '01. The 27th Annual Conference of the IEEE*, 2001, pp. 2000-2005 vol.3.

[16] S. Grabic, N. Celanovic, and V. A. Katic, "Permanent magnet synchronous generator cascade for wind turbine application," *IEEE Transactions on Power Electronics*, vol. 23, no. 3, pp. 1136-1142, May 2008.

[17] S. A. Papathanassiou and M. P. Papadopoulos, "Mechanical stresses in fixed-speed wind turbines due to network disturbances," *IEEE Transactions on Energy Conversion*, vol. 16, no. 4, pp. 361-367, Dec 2001.

[18] C. Hao, M. Chao, and Z. Xucheng, "Research on the switched reluctance wind generator system," in *Systems, Man, and Cybernetics, 2001 IEEE International Conference on*, 2001, pp. 1936-1941 vol.3.

[19] H. Chen, T. Su, F. Xiao, and A. Z. Y. Zhu Yifeng, "A switched reluctance wind power generator with the excitation of low voltage," in *Systems, Man and Cybernetics, 2002 IEEE International Conference on*, 2002, p. 5 pp. vol.6.

[20] R. Pena, J. C. Clare, and G. M. Asher, "A doubly fed induction generator using back-to-back PWM converters supplying an isolated load from a variable speed wind turbine," *IEE Proceedings-Electric Power Applications*, vol. 143, no. 5, pp. 380-387, 1996.

[21] M. Y. a. O. Motoyoshi, "Active and reactive power control for doubly-fed wound rotor induction generator," *IEEE Trans. Power Electron.*, vol. vol. 6, no. no. 4, pp. 624–629, 1991.

[22] S. Peresada, A. Tilli, and A. Tonielli, "Indirect stator flux-oriented output feedback control of a doubly fed induction machine," *IEEE Transactions on Control Systems Technology*, vol. 11, no. 6, pp. 875-888, Nov 2003.

[23] K. Amei, Y. Takayasu, T. Ohji, and M. A. S. M. Sakui, "A maximum power control of wind generator system using a permanent magnet synchronous generator and a boost chopper circuit," in *Power Conversion Conference, 2002. PCC Osaka 2002. Proceedings of the*, 2002, pp. 1447-1452 vol.3.

[24] K. Ohyama, S. Arinaga, and Y. Yamashita, "Modeling and simulation of variable speed wind generator system using boost converter of permanent magnet synchronous generator," in *Power Electronics and Applications, 2007 European Conference on*, 2007, pp. 1-9.

[25] L. Wei, C. Abbey, and G. Joos, "Control and Performance of Wind Turbine Generators based on Permanent Magnet Synchronous Machines Feeding a Diode Rectifier," in *Power Electronics Specialists Conference, 2006. PESC '06. 37th IEEE*, 2006, pp. 1-6.

[26] M. Chinchilla, S. Arnaltes, and J. C. Burgos, "Control of permanent-magnet generators applied to variable-speed wind-energy systems connected to the grid," *IEEE Transaction on Energy Conversion*, vol. 21, no. 1, pp. 130-135, March 2006.

[27] J. A. Sanchez, C. Veganzones, S. Martinez, F. Blazquez, N. Herrero, and J. R. Wilhelmi, "Dynamic model of wind energy conversion systems with variable speed synchronous generator and full-size power converter for large-scale power system stability studies," *Renewable Energy*, vol. 33, no. 6, pp. 1186-1198, Jun 2008.

[28] R. Johan and B. Lina Margareta, "Survey of Failures in Wind Power Systems With Focus on Swedish Wind Power Plants During 1997–2005," *IEEE transactions on Energy conversion*, vol. 22, no. 1, pp. 167-173, 2007.

[29] M. G. Simoes, B. K. Bose, and R. J. Spiegel, "Fuzzy logic based intelligent control of a variable speed cage machine wind generation system," *Power Electronics, IEEE Transactions on*, vol. 12, no. 1, pp. 87-95, 1997.

[30] T. Ahmed, O. Noro, K. Matzuo, Y. A. S. Y. Shindo, and M. A. N. M. Nakaoka, "Minimum excitation capacitance requirements for wind turbine coupled stand-alone self-excited induction generator with voltage regulation based on SVC," in *Telecommunications Energy Conference, 2003. INTELEC '03. The 25th International*, 2003, pp. 396-403.

[31] T. Ahmed, O. Noro, K. Matsuo, Y. A. S. Y. Shindo, and M. A. N. M. Nakaoka, "Wind turbine coupled three-phase self-excited induction generator voltage regulation scheme with static VAR compensator controlled by PI controller," in *Electrical Machines and Systems, 2003. ICEMS 2003. Sixth International Conference on*, 2003, pp. 293-296 vol.1.

[32] T. Ahmed, E. Hiraki, M. Nakaoka, and O. A. N. O. Noro, "Three-phase self-excited induction generator driven by variable-speed prime mover for clean renewable energy utilizations and its terminal voltage regulation characteristics by static VAr compensator," in *Industry Applications Conference, 2003. 38th IAS Annual Meeting. Conference Record of the*, 2003, pp. 693-700 vol.2.

[33] R. Cardenas, W. F. Ray, and G. M. Asher, "Switched reluctance generators for wind energy applications," in *Power Electronics Specialists Conference, 1995. PESC '95 Record., 26th Annual IEEE*, 1995, pp. 559-564 vol.1.

[34] D. McSwiggan, L. Xu, and T. Littler, "Modelling and control of a variable-speed switched reluctance generator based wind turbine," in *Universities Power Engineering Conference, 2007. UPEC 2007. 42nd International*, 2007, pp. 459-463.

[35] R. Cardenas, R. Pena, M. Perez, J. A. C. J. Clare, G. A. A. G. Asher, and P. A. W. P. Wheeler, "Control of a switched reluctance generator for variable-speed wind energy applications," *Energy Conversion, IEEE Transaction on*, vol. 20, no. 4, pp. 781-791, 2005.

[36] K. Ogawa, N. Yamamura, and M. Ishda, "Study for Small Size Wind Power Generating System Using Switched Reluctance Generator," in *Industrial Technology, 2006. ICIT 2006. IEEE International Conference on*, 2006, pp. 1510-1515.

[37] H. Polinder, F. F. A. van der Pijl, G. J. de Vilder, and P. J. A. T. P. J. Tavner, "Comparison of direct-drive and geared generator concepts for wind turbines," *IEEE Transaction on Energy Conversion*, vol. 21, no. 3, pp. 725-733, Sep 2006.

[38] Z. Yi and S. Ula, "Comparison and evaluation of three main types of wind turbines," in *Transmission and Distribution Conference and Exposition, 2008. T&D. IEEE/PES*, 2008, pp. 1-6.

[39] E. Fagan, S. Grimes, J. McArdle, P. Smith, and M. Stronge, "Grid code provisions for wind generators in Ireland," *Power Engineering Society General Meeting, 2005. IEEE*, pp. 3073-3079, 2005.

[40] I. M. de Alegria, J. Andreu, J. L. Martin, P. Ibanez, J. L. Villate, and H. Camblong, "Connection requirements for wind farms: A survey on technical requierements and regulation," *Renewable & Sustainable Energy Reviews*, vol. 11, no. 8, pp. 1858-1872, 2007.

[41] E. 50160, "Voltage characteristics of electricity supplied by public distribution systems," 1999.

[42] I. Erlich and U. Bachmann, "Grid code requirements concerning connection and operation of wind turbines in Germany," *Power Engineering Society General Meeting, 2005. IEEE*, pp. 2230-2234, 2005.

[43] C. Jauch, J. Matevosyan, T. Ackennann, and S. Bolik, "International comparison of requirements for connection of wind turbines to power systems," *Wind Energy*, vol. 8, no. 3, pp. 295-306, 2005.

[44] C. Jauch, P. Sørensen, and B. Bak-Jensen, "International review of grid connection requirements for wind turbines," *Nordic Wind Power Conference*, pp. 1–2, 2004.

[45] O. Anaya-Lara, X. Wu, P. Cartwright, J. B. Ekanayake, and N. Jenkins, "Performance of doubly fed induction generator (DFIG) during network faults," *Wind Engineering*, vol. 29, no. 1, pp. 49-66, 2005.

[46] D. Kastha and B. K. Bose, "Investigation of fault modes of voltage-fed inverter system for induction motor drive," *IEEE Transactions on Industry Applications*, vol. 30, no. 4, pp. 1028-1038, 1994.

[47] A. Causebrook, D. J. Atkinson, and A. G. Jack, "Fault ride-through of large wind farms using series dynamic braking resistors (March 2007)," *IEEE Transactions on Power Systems,* vol. 22, no. 3, pp. 966-75, 2007.

[48] J. Morren and S. W. H. de Haan, "Ridethrough of wind turbines with doubly-fed induction generator during a voltage dip," *IEEE Transactions on Energy Conversion,* vol. 20, no. 2, pp. 435-441, Jun 2005.

[49] L. Peng, B. Francois, and Y. Li, "Improved Crowbar Control Strategy of DFIG Based Wind Turbines for Grid Fault Ride-Through," in *Applied Power Electronics Conference and Exposition, 2009. APEC 2009. Twenty-Fourth Annual IEEE*, 2009, pp. 1932-1938.

[50] O. Gomis-Bellmunt, A. Junyent-Ferre, A. Sumper, and J. Bergas-Jan, "Ride-Through Control of a Doubly Fed Induction Generator Under Unbalanced Voltage Sags," *IEEE Transactions on Energy conversion,* vol. 23, no. 4, pp. 1036-1045, 2008.

[51] P. Zhou and Y. He, "Control strategy of an active crowbar for DFIG based wind turbine under grid voltage dips," in *Electrical Machines and Systems, 2007. ICEMS. International Conference on*, 2007, pp. 259-264.

[52] Y. Jin, J. E. Fletcher, and J. O'Reilly, "A Series-Dynamic-Resistor-Based Converter Protection Scheme for Doubly-Fed Induction Generator During Various Fault Conditions," *Energy Conversion, IEEE Transactions on,* vol. 25, no. 2, pp. 422-432, 2010.

[53] D. Xiang, R. Li, P. J. Tavner, and S. A. Y. S. Yang, "Control of a doubly fed induction generator in a wind turbine during grid fault ride-through," *IEEE Transaction on Energy Conversion,* vol. 21, no. 3, pp. 652-662, 2006.

[54] D. Santos-Martin, J. L. Rodriguez-Amenedo, and S. Arnaltes, "Providing Ride-Through Capability to a Doubly Fed Induction Generator Under Unbalanced Voltage Dips," *IEEE Transactions on Power Electronics,* vol. 24, no. 7, pp. 1747-1757, 2009.

[55] C. Abbey and G. Joos, "Supercapacitor Energy Storage for Wind Energy Applications," *IEEE Transactions on Industry Applications,* vol. 43, no. 3, pp. 769-776, 2007.

[56] O. Abdel-Baqi and A. Nasiri, "A Dynamic LVRT Solution for Doubly Fed Induction Generators," *IEEE Transactions on Power Electronics,* vol. 25, no. 1, pp. 193-196, 2010.

[57] M. S. El-Moursi, B. Bak-Jensen, and M. H. Abdel-Rahman, "Novel STATCOM Controller for Mitigating SSR and Damping Power System Oscillations in a Series Compensated Wind Park," *Power Electronics, IEEE Transactions on,* vol. 25, no. 2, pp. 429-441, 2010.

[58] A. H. Kasem, E. F. El-Saadany, H. H. El-Tamaly, and M. A. A. Wahab, "An improved fault ride-through strategy for doubly fed induction generator-based

wind turbines," *Renewable Power Generation, IET,* vol. 2, no. 4, pp. 201-214, 2008.

[59] J. Lopez, E. Gubia, E. Olea, J. Ruiz, and L. Marroyo, "Ride Through of Wind Turbines With Doubly Fed Induction Generator Under Symmetrical Voltage Dips," *IEEE Transactions on Industrial Electronics,* vol. 56, no. 10, pp. 4246-4254, Oct 2009.

[60] M. A. Abido, "Analysis and assessment of STATCOM-based damping stabilizers for power system stability enhancement," *Electric Power Systems Research,* vol. 73, no. 2, pp. 177-185, Feb 2005.

[61] A. H. Norouzi and A. M. Sharaf, "Two control schemes to enhance the dynamic performance of the STATCOM and SSSC," *IEEE Transactions on Power Delivery,* vol. 20, no. 1, pp. 435-442, Jan 2005.

[62] M. Molinas, J. A. Suul, and T. Undeland, "Low Voltage Ride Through of Wind Farms With Cage Generators: STATCOM Versus SVC," *IEEE Transactions on Power Electronics,* vol. 23, no. 3, pp. 1104-1117, 2008.

[63] J. C. Wu, "Novel circuit configuration for compensating for the reactive power of induction generator," *IEEE Transactions on Energy Conversion,* vol. 23, no. 1, pp. 156-162, Mar 2008.

[64] W. Qiao, G. K. Venayagamoorthy, and R. G. Harley, "Real-Time Implementation of a STATCOM on a Wind Farm Equipped With Doubly Fed Induction Generators," *IEEE Transactions on Industry Applications,* vol. 45, no. 1, pp. 98-107, Jan-Feb 2009.

[65] M. H. Haque, "Compensation of distribution system voltage sag by DVR and D-STATCOM," in *Power Tech Proceedings, 2001 IEEE Porto,* 2001, p. 5 pp. vol.1.

[66] J. F. Conroy and R. Watson, "Low-voltage ride-through of a full converter wind turbine with permanent magnet generator," *Renewable Power Generation, IET,* vol. 1, no. 3, pp. 182-189, 2007.

[67] M. A. Khan, P. Pillay, and M. Malengret, "Impact of direct-drive WEC Systems on the design of a small PM wind generator," in *Power Tech Conference Proceedings, 2003 IEEE Bologna,* 2003, p. 7 pp. Vol.2.

[68] M. Chinchilla, S. Arnaltes, and J. C. Burgos, "Control of permanent-magnet generators applied to variable-speed wind-energy systems connected to the grid," *IEEE transactions on Energy conversion,* vol. 21, no. 1, pp. 130-135, 2006.

[69] J. Y. Dai, D. D. Xu, and B. Wu, "A Novel Control Scheme for Current-Source-Converter-Based PMSG Wind Energy Conversion Systems," *IEEE Transactions on Power Electronics,* vol. 24, no. 4, pp. 963-972, Apr 2009.

[70] P. Tenca, A. A. Rockhill, and T. A. Lipo, "Wind turbine current-source converter providing reactive power control and reduced harmonics," *IEEE Transactions on Industry Applications,* vol. 43, no. 4, pp. 1050-1060, Jul-Aug 2007.

[71] T. Nussbaumer and J. W. Kolar, "Improving mains current quality for three-phase three-switch buck-type PWM rectifiers," *IEEE Transactions on Power Electronics,* vol. 21, no. 4, pp. 967-973, Jul 2006.

[72] V. Nedic and T. A. Lipo, "Low-cost current-fed PMSM drive system with sinusoidal input currents," *IEEE Transactions on Industry Applications,* vol. 42, no. 3, pp. 753-762, May-Jun 2006.

[73] T. Nussbaumer, M. Baumann, and J. W. Kolar, "Comprehensive design of a three-phase three-switch buck-type PWM rectifier," *IEEE Transactions on Power Electronics,* vol. 22, no. 2, pp. 551-562, Mar 2007.

[74] M. Baumann and J. W. Kolar, "Parallel connection of two three-phase three-switch buck-type unity-power-factor rectifier systems with dc-link current balancing," *IEEE Transactions on Industrial Electronics,* vol. 54, no. 6, pp. 3042-3053, Dec 2007.

[75] M. Shen and F. Z. Peng, "Operation modes and characteristics of the Z-source inverter with small inductance or low power factor," *IEEE Transactions on Industrial Electronics,* vol. 55, no. 1, pp. 89-96, Jan 2008.

[76] C. J. Gajanayake, D. M. Vilathgamuwa, and P. C. Loh, "Development of a comprehensive model and a multiloop controller for Z-source inverter DO systems," *IEEE Transactions on Industrial Electronics,* vol. 54, no. 4, pp. 2352-2359, Aug 2007.

[77] P. C. Loh, F. Gao, and F. Blaabjerg, "Topological and Modulation Design of Three-Level Z-Source Inverters," *IEEE Transactions on Power Electronics,* vol. 23, no. 5, pp. 2268-2277, Sep 2008.

[78] F. Gao, P. C. Loh, F. Blaabjerg, R. Teodorescu, and D. M. Vilathgamuwa, "Five-level Z-source diode-clamped inverter," *Power Electronics, IET,* vol. 3, no. 4, pp. 500-510, 2010.

[79] K. P. You and M. F. Rahman, "A Matrix-Z-Source Converter With AC-DC Bidirectional Power Flow for an Integrated Starter Alternator System," *IEEE Transactions on Industry Applications,* vol. 45, no. 1, pp. 239-248, Jan-Feb 2009.

[80] Z. J. Zhou, X. Zhang, P. Xu, and W. X. Shen, "Single-phase uninterruptible power supply based on Z-source inverter," *IEEE Transactions on Industrial Electronics,* vol. 55, no. 8, pp. 2997-3004, Aug 2008.

[81] Y. Tang, S. J. Xie, C. H. Zhang, and Z. G. Xu, "Improved Z-Source Inverter With Reduced Z-Source Capacitor Voltage Stress and Soft-Start Capability," *IEEE Transactions on Power Electronics,* vol. 24, no. 2, pp. 409-415, Feb 2009.

[82] M. Zhu, K. Yu, and F. L. Luo, "Switched Inductor Z-Source Inverter," *IEEE Transactions on Power Electronics,* vol. 25, no. 8, pp. 2150-2158, 2010.

[83] S. M. Dehghan, M. Mohamadian, A. Yazdian, and F. Ashrafzadeh, "A Dual-Input & Dual-Output Z-Source Inverter," *IEEE Transactions on Power Electronics,* vol. 25, no. 2, pp. 360-368, 2010.

[84] J. P. Barton and D. G. Infield, "Energy storage and its use with intermittent renewable energy," *IEEE Transactions on Energy Conversion,* vol. 19, no. 2, pp. 441-448, 2004.

[85] Z. Chen and E. Spooner, "Grid power quality with variable speed wind turbines," *IEEE Transaction on Energy Conversion,* vol. 16, no. 2, pp. 148-154, 2001.

[86] E. Muljadi and H. E. McKenna, "Power quality issues in a hybrid power system," *Ieee Transactions on Industry Applications,* vol. 38, no. 3, pp. 803-809, May-Jun 2002.

[87] E. 50160, "Voltage characteristics of electricity supplied by public distribution systems," *European Committee for Electrotechnical Standardization (CENELEC),* 1999.

[88] I. Erlich and U. Bachmann, "Grid code requirements concerning connection and operation of wind turbines in Germany," Piscataway, NJ, USA, 2005, pp. 1253-7.

[89] C. L. Masters, J. Mutale, G. Strbac, S. Curcic, and N. Jenkins, "Statistical evaluation of voltages in distribution systems with embedded wind generation," *IEE Proceedings-Generation Transmission and Distribution,* vol. 147, no. 4, pp. 207-212, Jul 2000.

[90] J. C. Pidre, C. J. Carrillo, and A. E. F. Lorenzo, "Probabilistic model for mechanical power fluctuations in asynchronous wind parks," *IEEE Transactions on Power Systems,* vol. 18, no. 2, pp. 761-768, 2003.

[91] P. Chiradeja and R. Ramakumar, "Voltage profile improvement with distributed wind turbine generation-a case study," in *IEEE Power Engineering Society General Meeting*, 2003, p. 2336 Vol. 4.

[92] R. Villafafila, S. Galceran, B. Bak-Jensen, C. Peiyuan, C. Zhe, and S. Sorensen, "Probabilistic assessment of wind power production on voltage profile in distribution networks," in *Electrical Power Quality and Utilisation, 2007. EPQU 2007. 9th International Conference on*, 2007, pp. 1-5.

[93] S. Chun-Line, "Effects of Distribution System Operations on Voltage Profiles in Distribution Grids Connected Wind Power Generation," in *Power System Technology, 2006. PowerCon 2006. International Conference on*, 2006, pp. 1-7.

[94] R. Pena, J. C. Clare, and G. M. Asher, "Doubly fed induction generator using back-to-back PWM converters and its application to variable-speed wind-energy generation," *IEE Proceedings-Electric Power Applications,* vol. 143, no. 3, pp. 231-241, May 1996.

[95] V. Kaura and V. Blasko, "Operation of a phase locked loop system under distorted utility conditions," *IEEE Transactions on Industry Applications,* vol. 33, no. 1, pp. 58-63, 1997.

[96] G. M. J. Herbert, S. Iniyan, E. Sreevalsan, and S. Rajapandian, "A review of wind energy technologies," *Renewable & Sustainable Energy Reviews,* vol. 11, no. 6, pp. 1117-1145, 2007.

[97] G. R. Slemon, "Modelling of induction machines for electric drives," *IEEE Transactions on Industry Applications,* vol. 25, no. 6, pp. 1126-1131, 1989.

[98] M. H. J. Bollen, *Understanding power quality problems: Voltage Sags And Interruptions*. New York: IEEE PRESS, 2000.

[99] J. G. Nielsen, M. Newman, H. Nielsen, and F. Blaabjerg, "Control and testing of a dynamic voltage restorer (DVR) at medium voltage level," *IEEE Transactions on Power Electronics,* vol. 19, no. 3, pp. 806-813, 2004.

[100] F. K. A. Lima, A. Luna, P. Rodriguez, E. H. Watanabe, and F. Blaabjerg, "Rotor Voltage Dynamics in the Doubly Fed Induction Generator During Grid Faults," *IEEE Transactions on Power Electronics,* vol. 25, no. 1, pp. 118-130, 2009.

[101] F. Z. Peng, "Z-source inverter," *IEEE Transactions on Industry Applications,* vol. 39, no. 2, pp. 504-510, March-April 2003.

[102] W. Lixiang, T. A. Lipo, and C. Ho, "Matrix converter topologies with reduced number of switches," in *Power Electronics Specialists Conference, 2002. pesc 02. 2002 IEEE 33rd Annual*, 2002, pp. 57-63 vol.1.

[103] C. Klumpner and C. Pitic, "Hybrid matrix converter topologies: An exploration of benefits," in *PESC Record - IEEE Annual Power Electronics Specialists Conference*, Rhodes, 2008, pp. 2-8.

[104] J. W. Kolar, F. Schafmeister, S. D. Round, and H. Ertl, "Novel Three-Phase AC-AC Sparse Matrix Converters," *IEEE Transactions on Power Electronics,* vol. 22, no. 5, pp. 1649-1661, 2007.

[105] L. Huber and D. Borojevic, "Space vector modulated three-phase to three-phase matrix converter with input power factor correction," *IEEE Transactions on Industry Applications,* vol. 31, no. 6, pp. 1234-1246, Nov-Dec 1995.

[106] F. Z. Peng, A. Joseph, J. Wang, M. S. Shen, L. H. Chen, Z. G. Pan, E. Ortiz-Rivera, and Y. Huang, "Z-source inverter for motor drives," *IEEE Transactions on Power Electronics,* vol. 20, no. 4, pp. 857-863, Jul 2005.

[107] E. Koutroulis and K. Kalaitzakis, "Design of a maximum power tracking system for wind-energy-conversion applications," *IEEE Transactions on Industrial Electronics,* vol. 53, no. 2, pp. 486-494, Apr 2006.

[108] M. Shen, A. Joseph, J. Wang, F. Z. Peng, and D. J. Adams, "Comparison of traditional inverters and Z-source inverter for fuel cell vehicles," *IEEE Transactions on Power Electronics*, vol. 22, no. 4, pp. 1453-1463, Jul 2007.

[109] Eltra, *Specifications for connecting wind farms to the transmission network*, Second ed. Denmark: Document ELT1999-411a

[110] H. S. Ko, G. G. Yoon, and W. P. Hong, "Active use of DFIG-based variable-speed wind-turbine for voltage regulation at a remote location," *IEEE Transactions on Power Systems*, vol. 22, no. 4, pp. 1916-1925, Nov 2007.

[111] I. Erlich, M. Wilch, and C. Feltes, "Reactive power generation by DFIG based wind farms with AC grid connection," in *Power Electronics and Applications, 2007 European Conference on*, 2007, pp. 1-10.

[112] R. Billinton and R. N. Allan, *Reliability Evaluation of Power Systems*: Springer, 1996.

[113] I. Y. F. Lun and J. C. Lam, "A study of Weibull parameters using long-term wind observations," *Renewable Energy*, vol. 20, no. 2, pp. 145-153, 2000.

[114] J. L. Devore, *Probability and statistics for engineering and the sciences*: Brooks/Cole Publishing Company, 1995.

[115] V. Akhmatov and A. H. Nielsen, "A small test model of the transmission grid with a large offshore wind farm for education and research at technical university of Denmark," *IEEE/PES Power Systems Conference and Exposition. Vols 1-5*, pp. 650-654, 2006.

[116] L. V. d. S. Pieter Schavemaker, *Electrical power system essentials*: John Wiley and Sons, 2008.

[117] http://mesonet.agron.iastate.edu/.

[118] E. Hau, *Wind Turbines: Fundamentals, Technologies, Application, Economics*: Springer, 2006.

[119] I. T. I. Council, *The ITI (CBEMA) curve*. (Available: www.itic.org/technical/iticurv.pdf).

[120] D. P. K. Reuven Y. Rubinstein, *Simulation and the Monte Carlo method* Wiley-Interscience, 2007.

[121] A. M. L. Dasilva and V. L. Arienti, "PROBABILISTIC LOAD FLOW BY A MULTILINEAR SIMULATION ALGORITHM," *Iee Proceedings-C Generation Transmission and Distribution*, vol. 137, no. 4, pp. 276-282, Jul 1990.

APPENDICES

Appendix A: Laplace transform

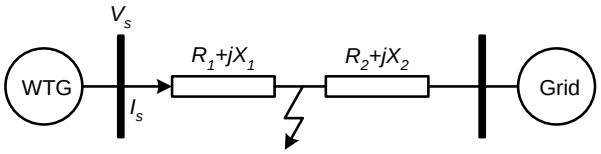

Fig.A.1 single-line equivalent circuit of grid-connected wind farm including transmission circuit

With the concern of fault situation shown in Fig.A.1, the (3.37) and (3.38) is rewritten as

$$i_{dr} = \frac{1}{L_m}\frac{\omega_s}{s^2 + 2(R_s/L_s)s + \omega_s^2} v_s - \frac{L_s}{L_m}\frac{X_1}{R_1^2 + X_1^2} v_s \tag{A.1}$$

$$i_{qr} = \frac{1}{L_m}\frac{s + R_s/L_s}{s^2 + 2(R_s/L_s)s + \omega_s^2} v_s - \frac{L_s}{L_m}\frac{R_1}{R_1^2 + X_1^2} v_s \tag{A.2}$$

The first terms in the right hand side of (A.1) and (A.2) are second-order model, which contribute on the vibrating of rotor current response. Thus the second terms are constant transfer function, which is insensitive on the vibrating. In order to reduce the vibrating, it is only needed to focus on the second-order model. On the other hand, the second terms in (A.1) and (A.2) are determined by the transmission circuits, but the first terms are depended on the DFIG, which is the scope of this study.

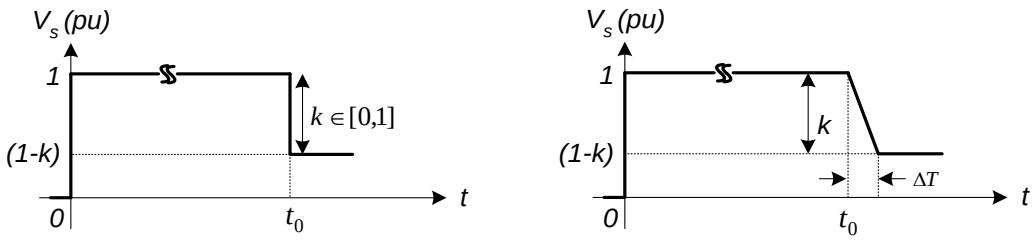

(a) (b)

Fig.A.2 The stator voltage of DFIG (a) without the series compensator (b) with linear-ramped series compensator

Figure A.2(a) shows the profile of stator voltage without the series compensator. In Fig.A.2, k is the voltage drop severity. At time t_0, there is a grid fault, which makes the stator voltage drop. Herein, t_0 is large enough to make the system into the rated condition before the grid fault. Consequently, the stator voltage in Fig.A.2(a) in frequency domain can be expressed by

$$v_s = V_s\left(\frac{1}{s} - \frac{k}{s}e^{-t_0 s}\right) \tag{A.3}$$

Where V_s is the magnitude of the nominal stator voltage.

On the other hand, with the linear ramp voltage generated by the series compensator, the stator voltage of the DFIG can be illustrated in Fig.A.2(b). And this voltage in frequency domain can be expressed by

$$v_s = V_s\left(\frac{1}{s} - \frac{k}{\Delta T}\frac{1}{s^2}e^{-t_0 s}\right) \tag{A.4}$$

Hence, due to (A.1) and (A.2), the rotor current responses according to the stator voltages shown in Fig.A.2 can be calculated as follow: Substituting (A.3) into (A.1) and (A.2), the rotor current d- and q-axis components can be calculated by inverse Laplace transformation, which is presented in (3.39) and (3.40). Similarly, substituting (A.4) into (A.1) and (A.2), the rotor current d- and q-axis components can be also calculated as shown in (3.43) and (6.44).

Appendix B: Wind power probability calculation

Derivation of the equation (6.9):

With the three operating ranges of the WTG, the calculation of the captured wind power can be divided into three sub-sections as zero output power, rated output power and power between zero and rated values.

During zero output power, the corresponding probability can be expressed with the wind speed distribution in (6.5):

$$F_P(0) = \int_0^{v_{in}} (\frac{k}{c})(\frac{v}{c})^{k-1} \exp[-(\frac{v}{c})^k]dv + \int_{v_{out}}^{\infty} (\frac{k}{c})(\frac{v}{c})^{k-1} \exp[-(\frac{v}{c})^k]dv$$

$$= 1 - \exp[-(\frac{v_{in}}{c})^k] + \exp[-(\frac{v_{out}}{c})^k]$$

During rated output power, the probability is derived as:

$$F_P(0) = \int_{v_r}^{v_{out}} (\frac{k}{c})(\frac{v}{c})^{k-1} \exp[-(\frac{v}{c})^k]dv$$

$$= \exp[-(\frac{v_r}{c})^k] - \exp[-(\frac{v_{out}}{c})^k]$$

Finally, when the output power is between zero and the rated levels, the probability value can be calculated by applying (6.6) directly. Hence, (6.9) can be determined.